Phosphorus-Based Anode Materials for Alkali-Ion Batteries



Isaac Capone

St. Catherine's College

University of Oxford

A thesis submitted for the degree of

Doctor of Philosophy

Abstract

The development of high energy density Li-ion batteries required for electric vehicle and portable device applications requires the advancement of electrode materials, specifically the increase of their specific capacity many-fold. Moreover, the high demand for these devices is likely to cause concerns, stemming from the geographical concentration and scarce availability of Li in the long term, which will likely result in an increase in cost of Li-ion batteries. Therefore research toward technologies based on similar chemistries, such as Na-ion and K-ion has shown increasing popularity. Red phosphorus (RP) is a promising anode material because it can host all three alkali ions, and is also able to deliver a very high theoretical capacity of $2596\,\mathrm{mAh\,g^{-1}}$ for Li and Na and $865\,\mathrm{mAh\,g^{-1}}$ for K, compared to graphite with Li and K ($372\,\mathrm{mAh\,g^{-1}}$ and $279\,\mathrm{mAh\,g^{-1}}$, respectively). However, it suffers from poor electronic conductivity ($10^{-14}\,\mathrm{S\,cm^{-1}}$) and, being an alloying material, also suffers from severe volume expansion/contraction upon cycling, which cause damage to the electrode material, leading to poor cycle life. In this thesis, I focus my attention on studying the properties of RP that could lead to the failure of the anode material. This study was first conducted at the particle level, where the mechanism of the alloying reaction was simulated by a computational model to understand the generation and development of stresses on the particle and the possibility that these could lead to its catastrophic failure. This was done by accurate measurement of the mechanical properties of RP, elastic and plastic, and the diffusivity of alkali ions in RP, provided here for the first time. Moreover, a study at the composite level of a RP-graphite electrode is provided. The effect of properties of the composite, such as the particle-size distri-

bution of RP and the mixing time of RP with graphite were investigated, in order to optimize the synthesis of a composite that can achieve high capacity and long cycle life. Finally, the research focused on how different electrolytes influence the performance of the material, which led to the identification of electrolyte compositions that improve the performance of the material for each alkali ion. This research provides a comprehensive study of the aspects that influence the cyclability and therefore the application of RP in electrochemical devices; ranging from the behaviour of the material at a particle level, then expanding to the composite and finally to the interaction between the electrode material and the electrolyte.

Some of the results presented in this work are shown in the following publications:

1. Isaac Capone, Kevin Hurlbutt, Andrew J. Naylor, Albert W. Xiao, and Mauro Pasta. Effect of the Particle-Size Distribution on the Electrochemical Performance of a Red Phosphorus–Carbon Composite Anode for Sodium-Ion Batteries. Energy Fuels, 33, 5, 4651–4658 (2019).

2. Isaac Capone, Jack Aspinall, Ed Darnbrough, Ying Zhao, Tae-Ung Wi, Hyun-Wook Lee and Mauro Pasta. Electrochemo-mechanical Properties of Red Phosphorus Anodes in Lithium, Sodium and Potassium-ion Batteries. Matter (2020).

3. Isaac Capone, Hyeon Jeong Lee, Albert W. Xiao, and Mauro Pasta. A High Performance Red Phosphorus-Graphite Composite as Anode Material for Potassium-Ion Batteries. In preparation.

Dedication

To my family, who have always supported me in all these years.

Declaration

I declare that the work presented in this thesis, unless otherwise stated, is the result of my original work and is written entirely by myself.

Acknowledgements

I would like to express my gratitude to everybody who helped me and offered me support along this path.

I am grateful to Prof. Mauro Pasta for granting me the opportunity to join the group and conduct my research experience in a stimulating place. I also thank him for his support, patience and all the advice that he provided me to not only improve my work, but also improve myself.

I am grateful to my lab mates and colleagues, in particular Jack Fawdon, Samuel Wheeler, Kevin Hurlbutt, Albert Xiao and Shobhan Dhir, for helping with this research and supporting me. Not to mention all the times they had to bear with my terrible jokes, ideas and theories. I also thank the postdoctoral researchers in the group, Hyeon Jeong Lee and Zack Brown, for their help and support.

I would like to thank my collaborators: Dr. Ying Zhao, for her help with the development of the "volume expansion model"; Dr. Ed Darnbrough and Jack Aspinall for their contribution to the measurement of the mechanical properties of RP; and Hyun-Wook Lee and Tae-Ung Wi for their help with acquiring the in-situ TEM data.

This research was made possible by the financial support from the John Fell Oxford University Press Research Fund and the Henry Royce Institute (through UK Engineering and Physical Science Research Council grant EP/R010145/1) for capital equipment. Special thanks to Modentech for supporting my research through a scholarship.

Many thanks to the David Cockayne Center for Electron Microscopy for allowing me to use their facilities and microscopes for my research.

Last, but not least, I would like to thank my family: my mother Pina and father Nunzio, and my brother Enrico, for their full support over all my choices. I would also like to thank Deborah, who has guided me through the most stressful times of my life over the past 10 years and hope she will keep doing it for more years to come.

Table of abbreviations

BET	Brunauer Emmet Teller surface area analysis
BP	Black phosphorus
CMC	Carboxymethyl cellulose
CTAB	Cetyl trimethyl ammonium bromide
DLS	Dynamic light scattering
EDX	Energy Dispersive X-Ray
EG	Ethylene glycol
EV	Electric vehicle
FEC	Fluoroethylene carbonate
GC	Galvanostatic cycling
GHG	Greenhouse gas
GITT	Galvanostatic intermittent titration technique
HAXPES	Hard X-ray photoelectron spectroscopy
KFSI	Potassium bis(fluorosulfonyl)imide
KIB	Potassium-ion battery
LCO	$LiCoO_2$
LIB	Lithium ion battery
LiFSI	Lithium bis(fluorosulfonyl)imide
LTO	$Li_4Ti_5O_{12}$
NaFSI	Sodium bis(fluorosulfonyl)imide
NIB	Sodium-ion battery

NMP	N-Methyl-2-Pyrrolidone
PAA	Polyacrylic acid
PEIS	Potentiostatic electrochemical impedance spectroscopy
PES	Photoelectron spectroscopy
PVDF	Polyvinylidene fluoride
PXCT	Pthycographic X-ray computer tomography
RP	Red phosphorus
SEI	Solid-electrolyte interphase
SEM	Scanning electron microscopy
SHE	Standard hydrogen electrode
SOXPES	Soft X-ray photoelectron spectroscopy
TEM	Transmission electron microscopy
USD	United States dollars
VC	Vinylene carbonate
WP	White phosphorus
XPS	X-ray photoelectron spectroscopy
XRD	X-ray diffraction

Contents

Abstract **i**

Dedication **iii**

Declaration **iv**

Acknowledgements **v**

Abbreviations **vii**

1 Introduction **1**

1.1 The need for energy storage 1

1.2 Li-ion batteries 2

1.3 Alternatives to Li-ion batteries 5

1.4 Anode materials for alkali-ion batteries 8

1.4.1 Intercalation materials 8

1.4.2 Conversion materials 11

1.4.3 Alloying materials 12

1.5 Phosphorus: an anode of choice 14

1.6 Aim of this project 22

1.7 References 23

2 Instruments and Methods **33**

2.1 Synthesis Techniques 33
2.1.1 Ball milling 33
2.1.2 Chemical synthesis 35
2.1.3 Electrode production 36
2.2 Material Characterization 38
2.2.1 DLS 38
2.2.2 Raman 40
2.2.3 X-ray diffraction 42
2.2.4 Photoelectron spectroscopy 44
2.2.5 Scanning electron microscopy 46
2.2.6 Transmission electron microscopy 48
2.2.7 Pthycographic X-ray computer tomography 49
2.2.8 Surface area analysis 50
2.2.9 Compression test 52
2.2.10 Nanoindentation 54
2.3 Electrochemical Characterization 56
2.3.1 Galvanostatic cycling 56
2.3.2 Galvanostatic intermittent titration technique 58
2.3.3 Potentiostatic Electrochemical Impedance Spectroscopy 61
2.4 References 62

3 Electrochemo-mechanical properties of RP 64

3.1 Introduction 64
3.2 Electrochemo-mechanics 65
3.3 Results and discussion 68
3.3.1 Electrochemical properties 68
3.3.2 Mechanical properties 71
3.3.3 Electrochemo-mechanical model 76

3.3.4 In-situ TEM: spherical RP particles . . . 80
3.3.5 In-situ TEM: ball milled RP particles . . . 81
3.3.6 In-situ TEM experiment modelling . . . 84
3.4 Conclusions . . . 85
3.5 References . . . 86

4 Effect of RP particle-size distribution 89
4.1 Introduction . . . 89
4.2 Results and discussion . . . 90
4.2.1 Control of the RP particle size . . . 90
4.2.2 Electrochemical performance: RP particle size . . . 94
4.2.3 Electrochemical performance: RP-graphite mixing . . . 98
4.3 Conclusions . . . 105
4.4 References . . . 106

5 RP-graphite as anode material for KIBs 108
5.1 Introduction . . . 108
5.2 Results and discussion . . . 109
5.2.1 Electrochemical performance . . . 109
5.2.2 Material Characterisation . . . 113
5.2.3 Raman operando . . . 115
5.2.4 Comparison with literature . . . 117
5.3 Conclusions . . . 118
5.4 References . . . 119

6 Electrolyte optimization 122
6.1 Introduction . . . 122
6.2 Results and discussion . . . 124
6.2.1 Electrolytes for LIBs . . . 124

6.2.2 Electrolytes for NIBs 125
6.2.3 Electrolytes for KIBs 127
6.3 Conclusions 129
6.4 References 131

Conclusions and Future work **133**

Key Findings and implications for the field 133
Future work 135

Appendices **138**

A Diffusivity values 138
B RP density 140
C Parameters used in the model 141
D RP volume expansion 142

Chapter 1

Introduction

1.1 The need for energy storage

Climate change is being driven by emissions of greenhouse gases (GHGs). Transportation accounts for ∼20% of global GHG emissions and therefore, it is a critical sector to decarbonise.[1] In the U.S., for example, a third of the total CO_2 pollution is related to transportation such as vehicles, trains or planes.[2] The leading strategy to decarbonise transportation is electrification of the transport system, such as moving from combustion engine vehicles to electric vehicles (EVs). Electrification of the majority of transport modes is dependent on energy storage. Batteries are the current leading form of energy storage for transportation due to their ability to store high amounts of energy in a small volume (high energy density). This is the reason for their widespread application in portable devices such as smartphones and laptops or electric vehicles.[3–5] Batteries are devices that convert the chemical energy of a reaction into electrical energy. They can be divided into two groups: primary and secondary batteries. Primary batteries, after the discharge reaction is complete, cannot be recharged and therefore are termed single-use. In secondary batteries, however, the reaction is reversible and provides multiple charge/discharge cycles. Lithium-ion batteries (LIBs) are the leading secondary battery technology due to their high specific energy density compared to other battery

systems. For this reason, LIBs are used over other battery chemistries in mobile phones and laptops. LIBs have also demonstrated success in EVs with impressive ranges now achieved. However, the energy density of LIBs is not high enough for practical heavy vehicles, and is far too low to enable the electrification of commercial aviation, one of the highest emitting modes of transportation. Therefore, much of the battery field's current research is focused on developing commercial batteries with increased energy density.[6, 7]

1.2 Li-ion batteries

Developed in the 1970s[8, 9], and commercialized by Sony in 1991, LIBs are widely used nowadays to power electronic devices. We can identify three main components in a battery:

- cathode (positive electrode)
- anode (negative electrode)
- electrolyte

They rely on the reversible transport of Li^+ ions from one electrode to the other while the electrons flow through an external circuit. During discharge, the anode is oxidized and Li^+ ions dissolve into the electrolyte, where they flow to the cathode, which is subsequently reduced.[10, 11] The overall charge neutrality of this process is kept by negatively-charged electrons that move from the anode to the cathode through an external circuit. During charge, an external voltage is applied to the system and the reverse reaction takes place, allowing electrical energy to be stored as chemical energy. The schematic in Figure 1.1 shows the components of the first commercialized LIB. Graphite (left) is the anode, which is reduced during charge and accommodates Li^+ ions to form LiC_6.

$$6C + Li^+ + e^- \rightarrow LiC_6 \tag{1.1}$$

On the opposite side of the cell is $LiCoO_2$ (LCO) as the cathode. During charge, the Co^{3+} ions are partially oxidised to Co^{4+} and Li^+ ions are released to the electrolyte medium (middle), according to the reaction:

$$LiCoO_2 \rightarrow Li_xCoO_2 + xLi^+ + xe^- \tag{1.2}$$

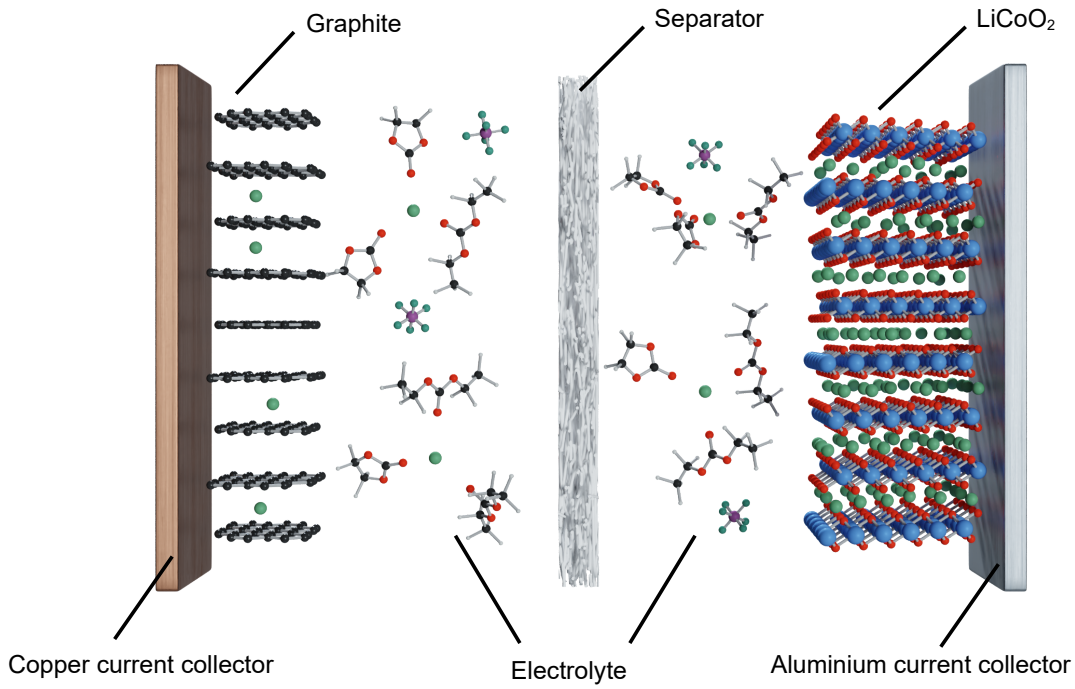


Figure 1.1: Schematic of LIB. From right to left: Cu current collector, graphite anode, electrolyte, separator, LCO cathode, Al current collector.

To ensure the electrical contact with the electrode materials, these are placed onto metal foils known as current collectors. Aluminium is mainly used for the cathode current collector. However, Li is able to alloy with Al at low potentials, therefore copper is used for the anode current collector. The development and the optimisation of the components of a battery is the primary focus of battery research, in order to improve their energy density, cycle life and decrease their cost per unit energy. Therefore, it is important to

understand how the energy stored in a battery can be calculated. The energy of a battery is calculated using the following equation:

$$\text{Energy}_{\text{cell}} = \int_0^{\text{Q}} \text{V}_{\text{Cell}} \text{dq} \tag{1.3}$$

where Q is the capacity of the electrode, defined as the amount of electric charge it is able to store during the chemical reaction per unit of mass, and V_{Cell} is the potential of the cell. The capacity is calculated with the equation:

$$\text{Q} = \frac{\text{nF}}{3600\text{M}_{\text{W}}} \tag{1.4}$$

where n is the number of the electrons involved in the reaction, F is the Faraday constant and M_{W} is the molar weight of the electrode compound that is electrochemically reacting. Therefore, the higher the capacity, the more alkali ions can be inserted and extracted into a material, resulting in an increase of the energy of the cell. Based on the reaction shown in Equation (1.1), graphite is able to deliver a theoretical capacity of $372\,\text{mAh}\,\text{g}^{-1}$ at a potential of 0.2 V vs Li^+/Li, while LCO is able to deliver a theoretical capacity of $274\,\text{mAh}\,\text{g}^{-1}$ if all the Li^+ ions are extracted. However, due to structural instability of LCO above 4.35 V vs Li^+/Li, it can only be partially delithiated, delivering a practical capacity of $165\,\text{mAh}\,\text{g}^{-1}$.[12]

The potential of the cell is defined by the chemical potential of Li^+ in the electrode materials, according to the equation:

$$\text{V}^0_{\text{Cell}} = \frac{\mu^0_{\text{c}} - \mu^0_{\text{a}}}{\text{nF}} = \text{E}^0_{\text{Cathode}} - \text{E}^0_{\text{Anode}} \tag{1.5}$$

where μ^0_{c} and μ^0_{a} are the standard chemical potentials of the Li in the cathode and anode, respectively and $\text{E}^0_{\text{Cathode}}$ and $\text{E}^0_{\text{Anode}}$ are the standard reduction potentials of the cathode and the anode, respectively. Similar to the capacity, the increase in the potential of the cell will result in an increase of the energy of the battery. From Equation (1.4) and Equation (1.5), the energy of the cell can be calculated using Equation (1.3). The

gravimetric energy density of the cell is calculated with the following equation:

$$\text{Energy density} = \frac{\text{Energy}_{\text{cell}}}{\text{mass}_{\text{cell}}} \tag{1.6}$$

Where $\text{mass}_{\text{cell}}$ is the sum of the masses of all the components (electrodes, electrolyte, separator and battery case) in the cell. Current state-of-the art LIBs employ 622 or 811 $LiNiMnCoO_2$ cathodes (where the numbers represent the ratio between transition metals) with silicon-containing graphite anodes, which are able to store up to $200\,\text{Wh}\,\text{kg}^{-1}$.[13] However, energy densities of 500-800 $\text{Wh}\,\text{kg}^{-1}$ are still required to realise practical electrified heavy goods vehicles, significantly increase the driving range of EVs, or to achieve the production of all-electric aircraft transport.[14] Therefore, in order to increase the energy of a battery, it is important to develop materials that have high capacity and/or to increase the difference of potential between the two electrodes.

1.3 Alternatives to Li-ion batteries

The application of LIBs in the market has expanded widely in recent years, with the demand set to increase tenfold by 2030, especially because of their application in electric vehicles.[5, 15] This raises significant concerns about the price and availability of Li in the near-future, because of the geographical concentration.[16] Therefore, attention has recently moved to the development of alternative battery technologies, which use elements with similar chemical and electrochemical properties, but are globally distributed, which may provide a sustainable alternative and possibly a higher energy density. Specifically, alkali metals such as sodium (Na) and potassium (K) have been deemed particularly promising. Of particular interest, Na and K are much more abundant than Li on the Earth's crust (47 billion tons in the largest deposit available, 7 billion tons and 80 million tons, for soda ash, potash and Li precursors, respectively).[17] This is reflected by the market price of the relative precursors, being 200, 1000, and 8,750 USD tons^{-1}, respectively.[17] Moreover, Na and K do not form alloys with Al, thus allowing for its

implementation as current collector for anodes, further reducing the cost and weight of the battery. For these reasons, electrochemical cells based on the mentioned two elements have been considered as a replacement of LIBs. Nevertheless, some differences need to be considered: firstly, the reduction potential of Na and K is -2.714 and -2.936 V vs SHE, respectively, higher than the reduction potential of Li (-3.040 V vs SHE), Figure 1.2.[18] Secondly, Na and K ions are bigger than Li: (1.02 Å and 1.38 Å respectively, compared to 0.76 Å, Figure 1.2b).[19] This means some materials, which have been optimized to work with Li, may work differently or not work at all with the other alkali ions. In transition metal oxide cathodes, for example, the occupancy of tetrahedral or octahedral sites with Li^+ or Na^+ ions can lead to the formation of different structures that exhibit different capacity.[20] Cathode materials such as $NaNi_{0.5}Mn_{0.5}O_2$,[21] and $Na_{2/3}[Fe_{1/2}Mn_{1/2}]O_2$ [22] have been identified as suitable cathode materials for NIBs, due to their capacity $>120\,mAh\,g^{-1}$ and $190\,mAh\,g^{-1}$, respectively and the lack of Co metal, which further reduces their cost. However, when cycled to high voltage (> 4.25 V vs Na^+/Na) they undergo a irreversible phase change that reduces the reversible capacity and leads to capacity decay. However, transition metal oxides cathodes showed poor performance with K. In fact, the larger size of K^+ ions induces numerous phase transitions and structural instability during electrochemical cycling, which lead to capacity fading and low cyclability.[23–25] Prussian blue analogues, on the other hand, have been implemented in KIBs, due to their ability to store K^+ ions with a minimal structural change and their ability to deliver a theoretical capacity of $155\,mAh\,g^{-1}$ (for $KMn[Fe(CN)_6]$). However, interstitial water that can be present in the crystal structure can cause deleterious effects on the cyclability and reduce its cycle life.[26]

The development of anode materials with improved capacity and cycling stability is also another focus of the research on energy storage, in particular for the development of alkali-ion batteries.[27, 28] For example, graphite, the most used anode material in LIBs, does not react with Na^+ ions.[29–33] However, it is able to host K^+ ions, but results in a lower capacity than Li ($279\,mAh\,g^{-1}$ compared to $372\,mAh\,g^{-1}$).[33, 34] Moreover,

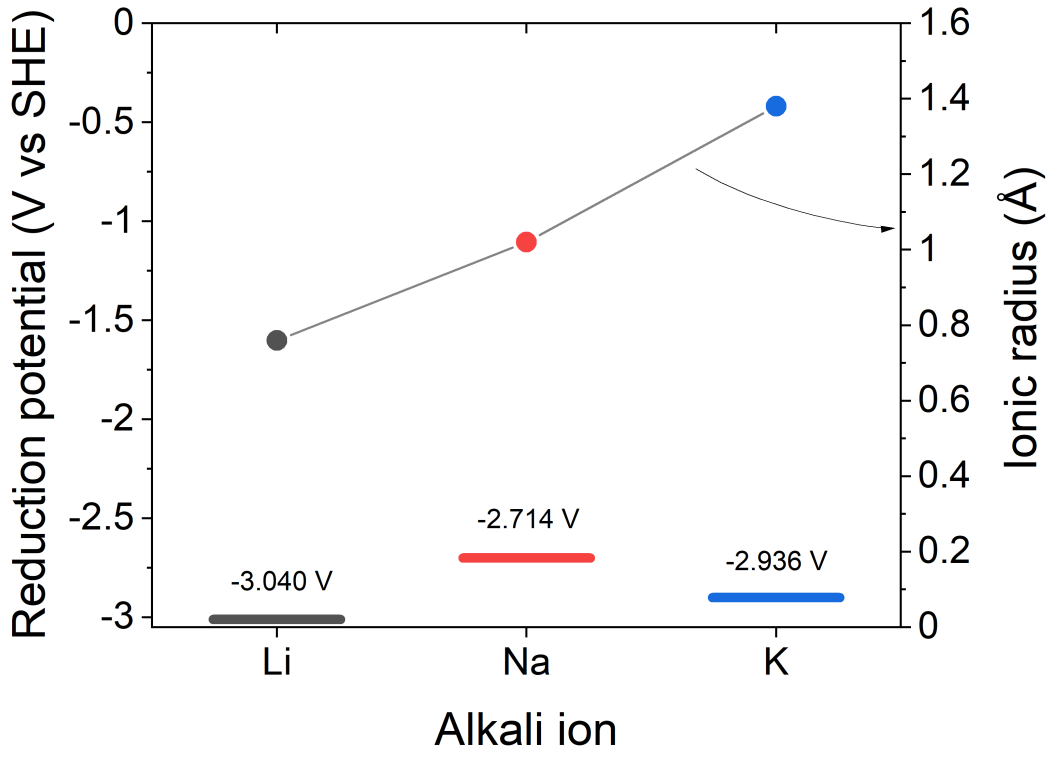


Figure 1.2: Reduction potentials and sizes of Li, Na and K.

the reaction between K^+ and graphite induces a volume expansion on the material of about 61%, six times larger than the one induced by the reaction with Li^+, resulting in higher strain on the material.[35] In sodium-ion batteries (NIBs), hard-carbon has been developed as an alternative anode material to graphite.[36, 37] However the performance reported so far (capacity of $300\,mAh\,g^{-1}$ and a working potential of 0.2 V vs Na^+/Na) are insufficient to make NIBs competitive with LIBs.[38] An anode material with high capacity is required in order to increase the energy density of NIBs. In this thesis, the focus will be the development of a suitable anode material for Li, Na and K. In the next section, a description of the main classes of anode materials and their performance with the three alkali ions are described.

1.4 Anode materials for alkali-ion batteries

An ideal anode material must satisfy the following requirements [39]:

- high reversible capacity
- low working potential
- low cost
- long cycle life
- easily scalable

We can distinguish three main classes of materials that have been developed so far, based on the type of reaction they undergo with the alkali metal: intercalation, conversion and alloying materials (Figure 1.3).

1.4.1 Intercalation materials

Graphite, a carbon based material, is widely used as anode in LIBs due to its high capacity ($372\,\mathrm{mAh\,g^{-1}}$, low working potential (0.1 V vs Li^+/Li) and ease of production. These properties allowed for the development and commercialisation of LIBs.

Graphite has a layered structure where each carbon atom is covalently bonded to three other C atoms to form sheets with hexagonal arrangements of atoms (Figure 1.4a). These layers are stacked to form the final hexagonal crystal structure. Moreover, each C atom has a delocalized electron that can move along the layers, resulting in a high electronic conductivity.[40] The reaction between Li^+ ions with graphite takes place with the introduction of the ions between the layers, in a process defined as "intercalation",[41, 42] resulting in the formation of the phase LiC_6. A similar reaction occurs in potassium-ion batteries (KIBs),[43] where the phase formed is KC_8, with a theoretical capacity of $279\,\mathrm{mAh\,g^{-1}}$, based on the reaction:

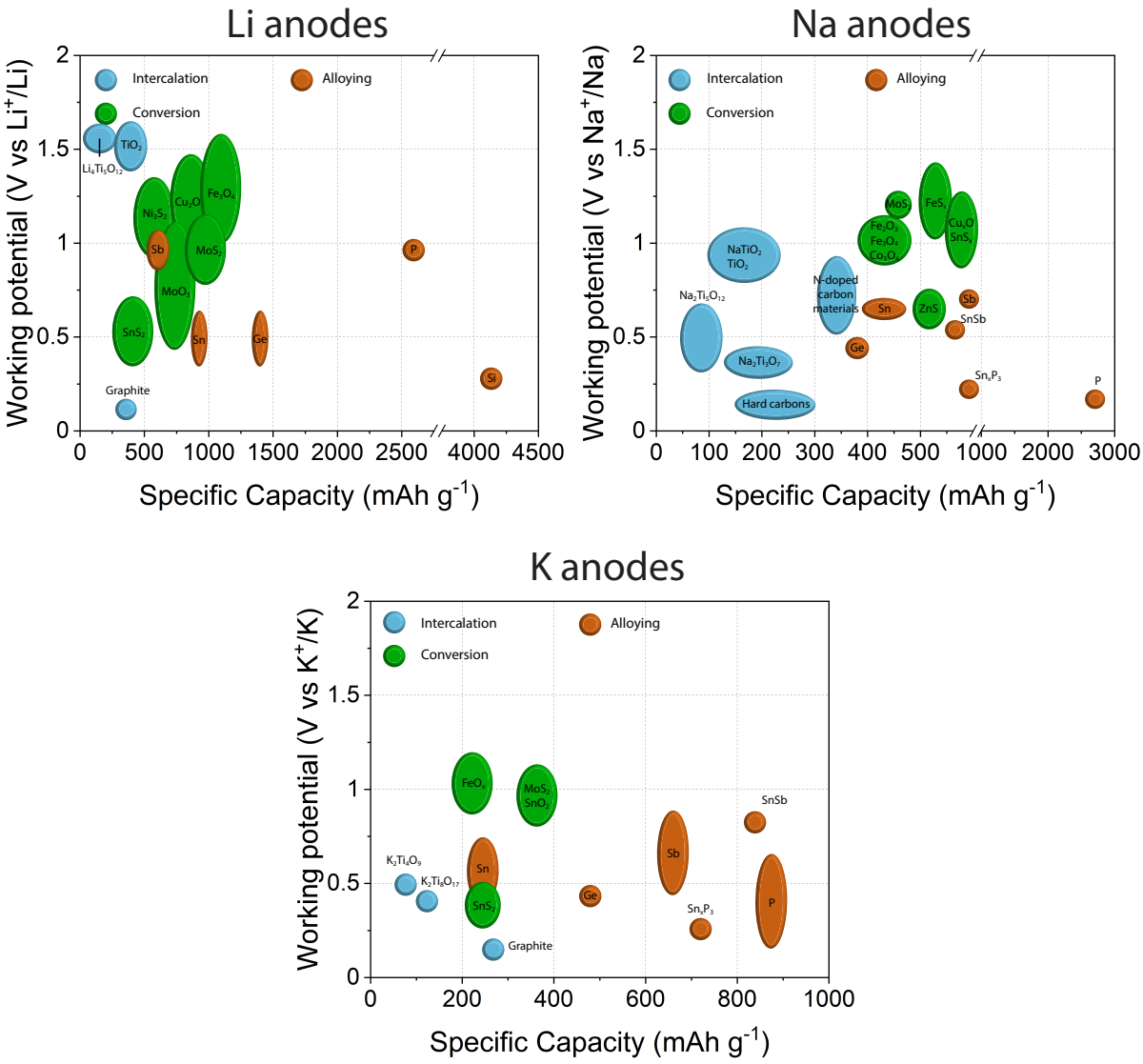


Figure 1.3: Main anode materials developed for Li, Na and K.

$$K^+ + 8C + e^- \rightarrow KC_8 \tag{1.7}$$

Interestingly, Na does not intercalate into graphite.[29–33, 44] Moriwake et al. suggested that this is due to an equilibrium between the type of bond formed between the alkali ions and the carbon atoms in graphite.[32] According to simulations, the ionic bond between K^+ ions and carbon atoms is strong enough to allow the formation of a stable phase. The bond becomes stronger as one moves down group 1 in the periodic table. In the Li case, although the ionic character of the bond fades, the covalent character

prevails, allowing for the formation of the lithiated phase. Unfortunately, with Na, both the ionic and the covalent character of the bond are weak and do not allow the formation of a stable sodiated phase. With the need for an alternative anode material to graphite for NIBs, other carbon-based materials such as hard-carbons or alloying materials such as phosphorus were developed.[36, 45–47] Hard-carbons are synthesized by heat treatment of oxygen-rich organic precursors such as carbohydrates at high temperatures ($> 900\,^{\circ}C$) in an inert atmosphere. The resulting material has a structure that is mainly amorphous with short range crystalline domains similar to graphite but with a larger layer interspace (Figure 1.4b). It has been reported that the reaction in these materials occurs in two steps: first there is the intercalation of sodium in the crystalline domains; then, sodium plates into the pores of the material.[37]

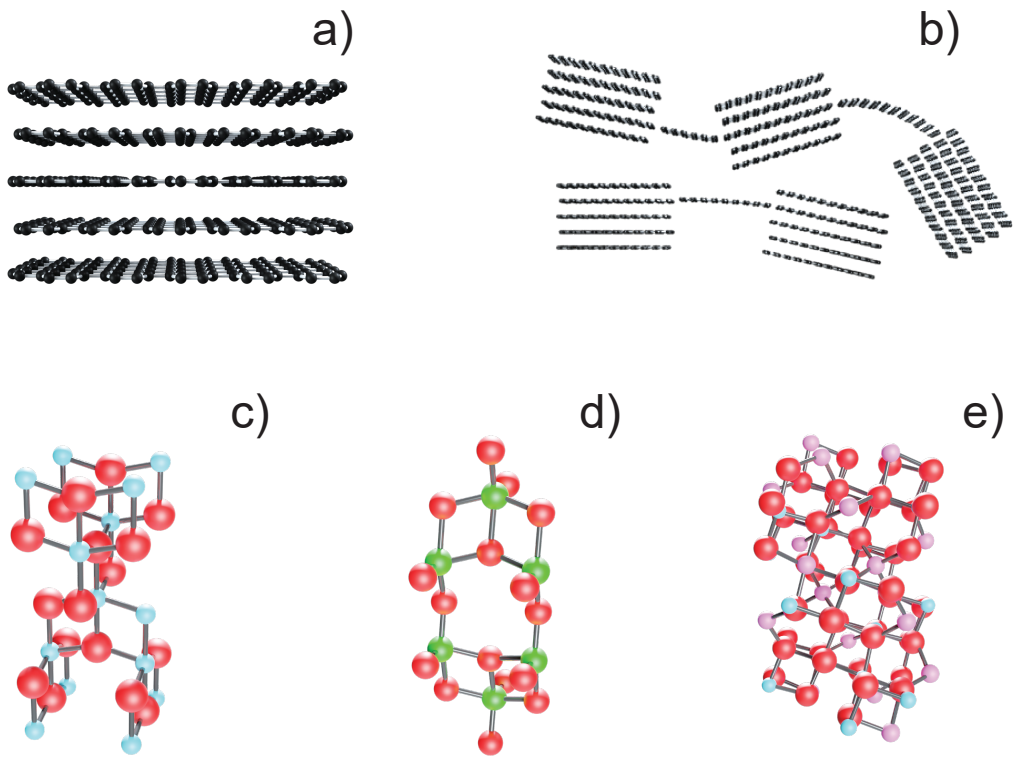


Figure 1.4: Main intercalation anodes: a) graphite, b) hard-carbon, c) TIO_2, d) V_2O_5 and e) LTO. Colours of the balls indicate: black = C, light blue = Ti, green = V, purple = Li.

Examples of other layered intercalation anode materials include transition metal oxides, such as $Li_4Ti_5O_{12}$ (LTO), for LIBs (Figure 1.4c),[48] TiO_2 for LIBs and NIBs,[49–52] or V_2O_5 for KIBs (Figure 1.4d).[53] Unfortunately, these materials have demonstrated lower performance compared to graphite. LTO and TiO_2 for example, showed a capacity of 160 $mAh\,g^{-1}$ and 170-200 $mAh\,g^{-1}$ in LIBs, respectively, while V_2O_5 delivered a high capacity of 500 $mAh\,g^{-1}$, but at a high potential of about 2.5 V. The need for higher energy density batteries drives research toward materials with a high capacity at a low working potential. For these reasons, conversion and alloying materials have been studied.

1.4.2 Conversion materials

Common conversion materials include transition metal oxides,[54, 55] sulfides [56–59], phosphides and fluorides. [60] Their reaction with an alkali metal leads to the formation of an alkali metal-containing phase and a transition metal phase (Figure 1.5a):

$$nA^+ + MX_n + ne^- \rightarrow nAX + M \tag{1.8}$$

Where A is an alkali ion (Li^+, Na^+, K^+), M is a transition metal (Fe, Mn, Co, Cu, Sn) and X is an anionic specie (O, S, F, P). This can lead to much higher capacities than intercalation materials. Materials such as Co_3P (Figure 1.5b) and Co_3O_4 have been reported to have achieved high capacity with Li (1250 $mAh\,g^{-1}$ and 1468 $mAh\,g^{-1}$, respectively).[61–63] Similar transition metal oxides, including Fe_2O_3 (Figure 1.5c) have been reported with Na and K.[64–66]

Unfortunately, this kind of reaction faces several challenges. First, the reaction leads to a structural reorganisation of phases that can result in volume changes, irreversible capacity on the first cycle and also poor cycling. They also show a large hysteresis (difference of potential between charge and discharge) while cycling, leading to an intrinsic energy loss at every cycle.[67] Nanosizing of the particles or the preparation of conversion material-carbon composites are strategies that are currently used to improve the

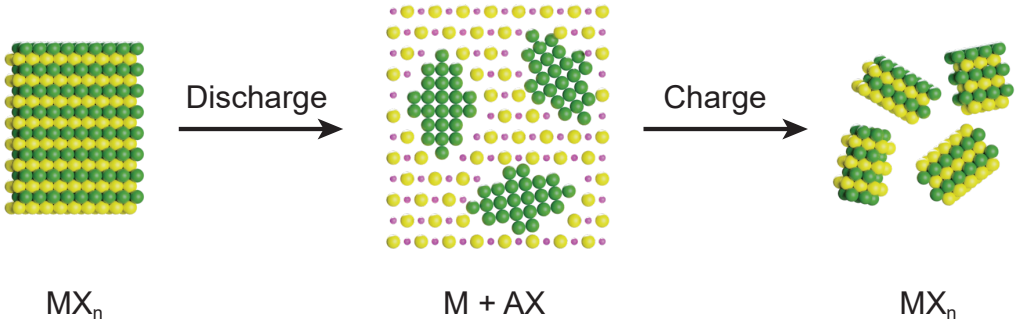


Figure 1.5: Schematic of conversion reaction. Green = transition metal (Fe, Mn, Co, Cu, Sn), yellow = anionic specie (O, S, F, P), purple = alkali metal (Li, Na or K).

performance of this class of materials.[68]

1.4.3 Alloying materials

Alloying materials are elements such as Si, Ge, Sn and P that react with an alkali ion to form a single phase, according to the reaction:

$$xA^{+} + M + xe^{-} \rightarrow A_xM \tag{1.9}$$

Si has been widely studied because of its reaction with Li, which results in a high theoretical capacity of 4200 mAh g^{-1}.[69] However, although sodiated and potassiated Si alloys have been predicted, no successful electrochemical alloying with Na and K has been achieved so far.[70, 71] On the other hand, Ge, Sn and P are able to form alloys with all three alkali ions. However, like conversion materials, these materials suffer from a large volume expansion (approximately 400% in the Si case) when cycling, which leads to loss of electrical contact and delamination of the active material from the current collector, resulting in a poor cycle life.[72] Past works with Si demonstrated how the use of nanosized particles can increase the performance of the material with Li. Liu et al. demonstrated a correlation between the particle size of crystalline Si and the formation of cracks on the particle during lithiation.[73] In particular, they investigated the importance

of the particle size in the formation of cracks and fracture of the particle when alloying. This way, they were able to identify the critical particle size of crystalline Si (150 nm) i.e. the size above which the particles would crack upon lithiation. Amorphous Si was also tested in a similar manner by McDowell et al., who showed that particles up to 870 nm in diameter would not crack, mainly due to the isotropic diffusion of the lithium into the material.[74] Ge and Sn have also been studied as they can successfully alloy with the three alkali ions, with a high theoretical capacity with the three alkali ions. In particular, Ge can form $Li_{22}Ge_5$, NaGe or KGe, with theoretical capacities of 1623, 369 and 369 $mAh\,g^{-1}$, respectively.[75–77] Sn on the other hand has the ability to form phases such as $Li_{4.4}Sn$, $Na_{15}Sn_4$ and KSn, with theoretical capacities of 993, 847 and 226 $mAh\,g^{-1}$.[75, 78, 79] However, materials reported using these elements have shown low capacities and fast capacity decay over the first few cycles so far, due to failure of the electrodes caused by the volume expansion of the particles. Among the alloying materials, P delivers the highest capacity due to the formation of Li_3P, Na_3P and KP, with theoretical capacities of 2596 $mAh\,g^{-1}$ for Li and Na and 865 $mAh\,g^{-1}$ with K, at relatively low potentials (0.9 V, 0.2 V and 0.5 V with Li, Na and K, respectively).[46, 80, 81] Electrode materials prepared with this element have demonstrated high capacity, but fast capacity fading (related to the volume expansion of P) over the first 20-30 cycles is a common issue.[82, 83]

The choice of electrode materials is important for the development of high energy density batteries. Among the type of anode materials discussed, alloying materials are both able to achieve the highest capacities whilst also reacting at low potentials. In particular, P is the material that offers the highest theoretical capacity (second only to Si in LIBs) and is able to work with all three alkali ions. The development of a high performing material, however, requires a careful optimization of the components of the electrode. In particular, the electrochemically active material needs to be mixed with a conductive carbon additive to improve the electronic conductivity of the electrode and a binder to ensure its adhesion to the current collector. These factors can heavily affect

the performance of the electrode. Therefore these parameters need to be carefully tuned in order to allow its application in LIBs, NIBs and KIBs.

1.5 Phosphorus: an anode of choice

Phosphorus can successfully alloy with all three alkali ions (Li, Na and K) with a high theoretical capacity (2596 $mAh\,g^{-1}$ with Li and Na and 865 $mAh\,g^{-1}$ with K), and therefore it is an ideal anode material to investigate. However, it exists in different allotropes, and an accurate analysis of the most common ones is required to identify the one that combines safety and low cost, parameters that are required to allow its commercialisation. The most common allotropes of P are named after their color: white phosphorus (WP), red phosphorus (RP) and black phosphorus (BP). WP has a crystal structure composed of P_4 molecules packed together, Figure 1.6a. However, it is the least stable and most dangerous of the allotropes: it is pyrophoric when exposed to air and the reaction develops toxic P_2O_5 gas. Therefore, its use is not recommended at industry scale.

RP is the amorphous allotrope of phosphorus. It is a derivative of WP, where a P-P bond in the P_4 molecule is dissociated and new bonds between adiacent P_4 tetrahedron are formed, thus forming a polymeric chain (Figure 1.6b). It was first obtained by treating WP at high temperature (about 230-300 °C) in vacuum or inhert atmosphere.[84, 85] Unlike WP, RP is very stable and safe in air. It is also widely commercially available and inexpensive. Unfortunately, it has a very low electronic conductivity of about $10^{-14}\,S\,cm^{-1}$.

BP can be obtained from RP by applying high temperature and pressure.[86, 87] This leads to the formation of a crystalline layered structure similar to graphite.(Figure 1.6c) In the crystal P-P bonds form a puckered honeycomb structure where adjacent layers are held together by van der Waals forces. However, differently from graphite, the hexagonal arrangement of P atoms is puckered and each atom bond with three other P atoms, with a lone electron pair situated in the sp^3 hybrid orbital, which is responsible of the

increased electronic conductivity of this allotrope ($1\,S\,cm^{-1}$). However, its cost is much higher because of the conditions required for its preparation. 35 mg of lab scale high-purity (> 99.99%) BP, for example, can be sold at 1150 USD (32,857 USD g^{-1}), while 1 kg of RP can be sold for as low as 125 USD (0.125 USD g^{-1}, prices obtained from Sigma Aldrich).

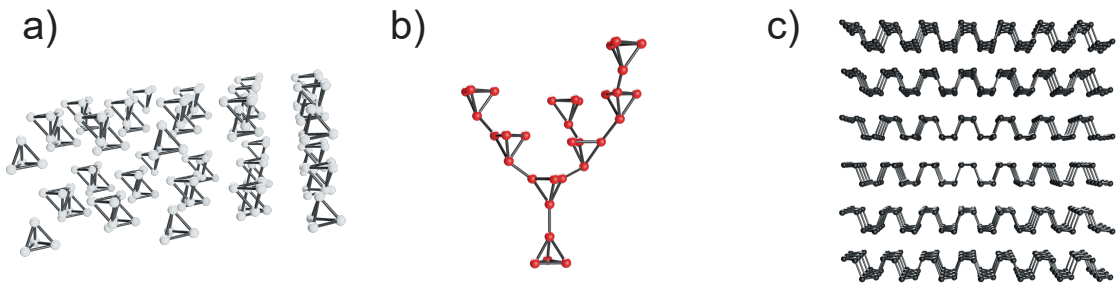


Figure 1.6: Main phosphorus allotropes. a) White phosphorus, (b) red phosphorus and (c) black phosphorus.

The allotropes that are mainly used in the research on phosphorus-based anode materials are RP and BP. Their reaction with the alkali ions is similar, with both allotropes forming the phases Li_3P, Na_3P and KP as final products. However, BP has been reported to undergo an initial intercalation step, where Li^+ or Na^+ ions insert between its layers.[88] Mayo et al. and Yang et al. reported the predicted reaction paths that the alloying reaction of phosphorus with Li, Na and K should follow. They suggested that Li alloying with P should go through the phases $P \rightarrow LiP_7 \rightarrow Li_3P_7 \rightarrow LiP \rightarrow Li_3P$, while Na alloying should follow the path $P \rightarrow Na_3P_{11} \rightarrow Na_3P_7 \rightarrow NaP \rightarrow Na_5P_4 \rightarrow Na_3P$; K alloying on the other hand is predicted to undergo this reaction path: $P \rightarrow K_{3P11} \rightarrow K_2P_3 \rightarrow KP$.[89, 90] The formation of the final crystalline product of the alloying with Li, Na and K has been confirmed via XRD or NMR by a number of publications.[66, 81, 91] Moreover, it has been confirmed that the crystalline structure of BP is not recovered after full delithiation, but an amorphous phosphorus phase is obtained, with different properties than BP.[92] However, little is known about the real reaction path that is followed. Recent reports by Sottmann et al. and Marbella et al. showed that the reac-

tion path of the alloying and dealloying reactions of Na with RP may be different.[93, 94] Marbella et al. showed that the alloying reaction goes through the formation of the phases P $\rightarrow$ NaP $\rightarrow$ Na_3P while the dealloying reaction goes through the formation of the phases $Na_3P \rightarrow Na_{2.6}P \rightarrow Na_{2.36}P \rightarrow$ P and that the intermediates that were formed were amorphous. However, a similar study concerned about Li and K is still missing. Knowing if intermediate phases are formed during the reaction and if they are crystalline or amorphous can help elucidate the mechanism of the reaction and if the possible formation of crystalline intermediates can trigger stresses at the phase boundary that can lead to stresses that can cause cracks on the particles. This is very important, as phosphorus also suffer from huge volume expansion (168%, 332% and 162% in the case of RP alloying with Li, Na and K, respectively) that leads to failure of the material, loss of electrical contact and low cycle life. Currently, solving the problem of volume expansion is the main focus of the research on these materials. Possible ways to overcome these issues are (1) the preparation of mixtures of phosphorus and carbon materials to form composites (P/C composites), thus increasing the electronic conductivity and ensuring the electric contact between the particles; or (2) the nanosizing of P particles in order to mitigate the deleterious effect of their volume expansion to the electrode material and prolong its cycle life.

We can distinguish between four main ways to prepare phosphorus-based electrodes in order to achieve these two strategies:

- Mechanical milling
- Vaporization-condensation
- Sonication
- Chemical synthesis

Mechanical milling is a process where a material is ground in a ball mill at a high energy to reduce its particle size and distribution. In this process, the material is placed

with some stainless steel, zirconia or tungsten carbide balls in a jar and is rotated at a high frequency. The energy developed by the collision between the balls causes the particles to break, decreasing their size. This method is often used not only to reduce the particle size distribution of phosphorus, but also to mix it with carbon additives, in order to obtain a homogeneous composite in one single step. Among all the methods, this is by far the most reported in the literature thanks to its ease of application, safety and scalability. One of the first works that showed the preparation of a P/C composite by ball milling was presented by Park et al. in 2007. They showed a RP-Super P composite with a 7:3 mass ratio between the components.[92] This composite showed poor performance when fully cycled down to 0.01 V vs Li^+/Li but excellent stability if partly cycled to 0.78 V vs Li^+/Li (Figure 1.7a). The capacity developed, however, was well below the theoretical capacity because the full potential of the material was not exploited. This work suggested that the main cause of material failure was the volume expansion of phosphorus and the damages that it caused to the electrode. Kim et al. demonstrated how a phosphorus-to-carbon mass ratio equal to 7:3 in the composite was a good balance for obtaining a mixture with high capacity and rate capability.[81] In the same period, Qian et al. developed a composite for NIBs with the same mass ratio but using carbon black as carbon additive.[95] Their work showed two important effects. It was shown how the high energy developed during ball milling could cause the phase conversion from RP to BP after only 6 h and full conversion of BP to amorphous phosphorus after 24 h (Figure 1.7b). Moreover, they showed how the addition of additives to the electrolyte such as fluoroethylene carbonate (FEC) would enhance the cycle life of the material in NIBs (Figure 1.7c). This was related to the stability of the solid-electrolyte interphase (SEI), a passivation layer that forms at low potentials on the surface of the negative electrode, which is composed of decomposition products of electrolyte and its additives, as suggested by Komaba et al.[96]

Later, Ramireddy et al. tested a RP-graphite composite with Li and Na (Figure 1.7d,e).[82] However, despite the high capacity on the first few cycles, the cycle

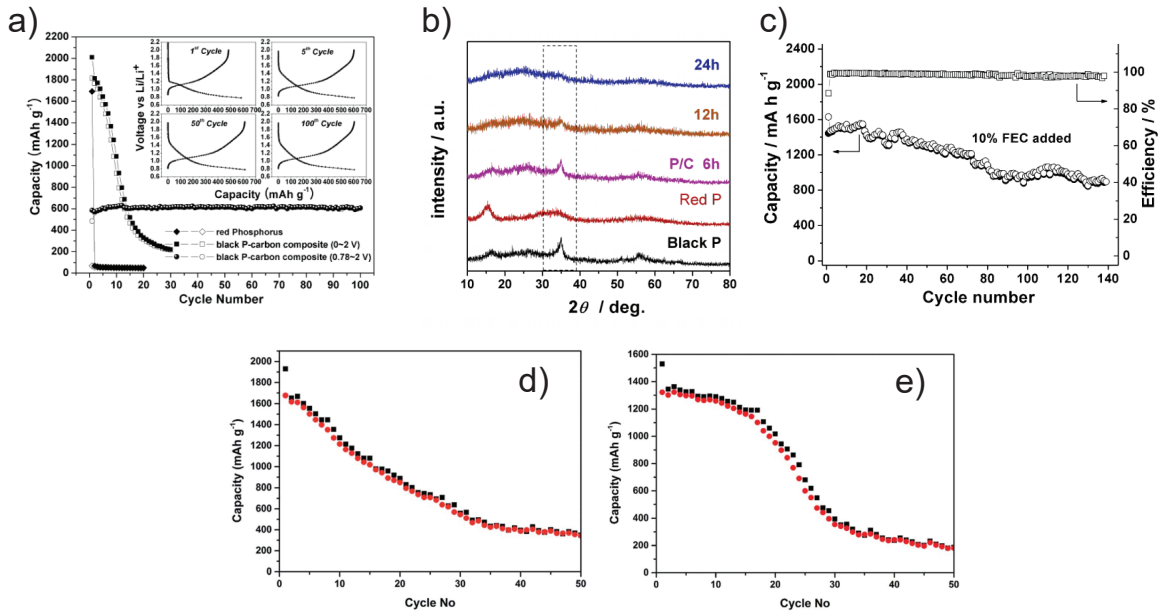


Figure 1.7: Electrochemical performance of a BP/carbon composite prepared by Park et al., and cycled in the range 0.78 - 2 V and 0.01 - 2 V vs Li^+/Li.[92] Conversion of RP to BP and to amorphous P induced by high-energy ball milling.[95] Effect of FEC used as additive in NIBs electrolytes.[95] Electrochemical performance of a RP/carbon nanocomposite prepared by Ramireddy et al. and tested with Li (d) and Na (e).[82]

life was very poor, with pronounced capacity fading after 20 cycles. The cause was the volume expansion of the particles and consequent loss of electrical contact between them. This composite was also tested with K, and the performance was similar.[83] Although it is known that the particle size distribution of phosphorus is important to the stability of the electrode while cycling, it is still not clear what particle size was used in these experiments, because once the preparation of the composite is complete, the measurement of the particle size of the components (phosphorus and carbon) is challenging.

The vaporization-condensation method takes advantage of the ability of RP to sublimate at temperatures higher than 400 °C. Generally, RP and a carbon-based additive are placed in an evacuated ampoule and treated at temperatures as high as 600 °C. In these conditions, RP will sublimate and fill the atmosphere of the ampoule as P_4. The temperature is then gradually decreased to RT, allowing phosphorus to crystallize in the form of nanoparticles on the carbon additive as WP. Due to the dangerous nature of WP, the obtained composite is generally kept at about 200 °C for several hours to convert WP

to RP but also washed with CS_2, the only solvent known that can dissolve WP. Previously reported materials that have been prepared following this method showed superior performance and high stability with the three alkali ions (Figure 1.8).[97, 98] However, this method raises concerns over the safety of the process, due to the formation of WP, and the small amount of material that can be processed, which hinders its scalability.

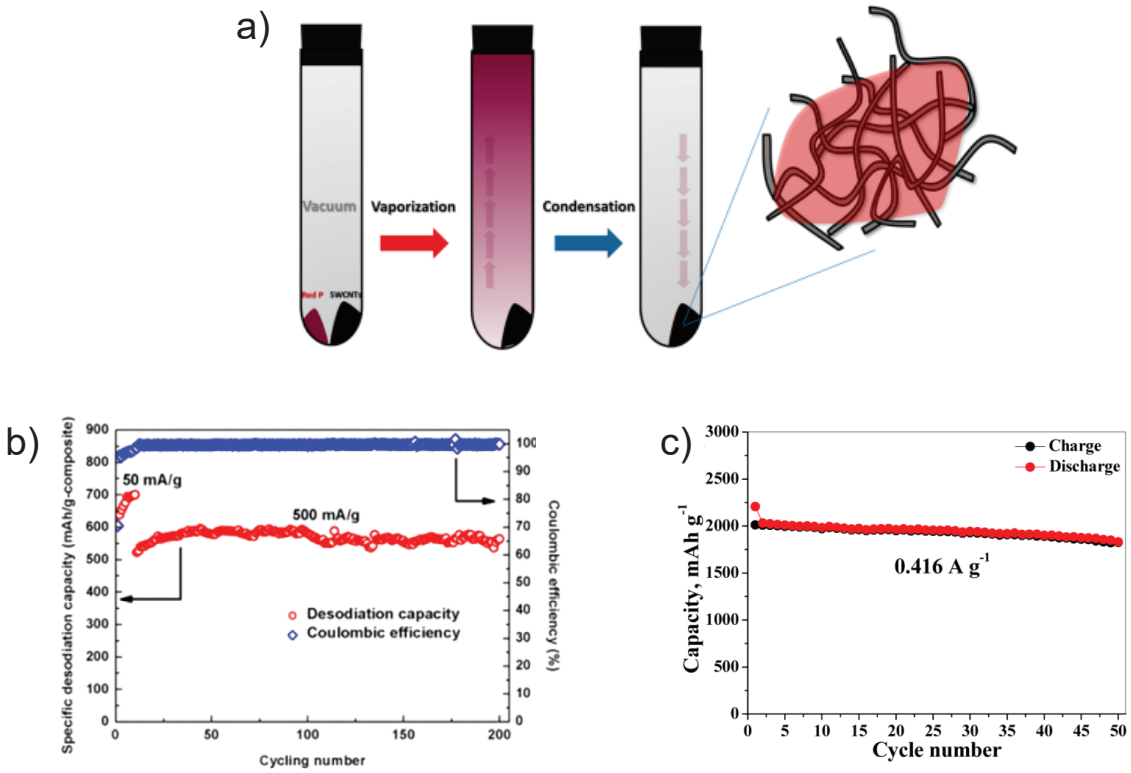


Figure 1.8: a,b) Schematic of vaporization-condensation process used by Zhu et al. and electrochemical performance of the RP-single wall carbon nanotube composite for NIBs from [97]. Electrochemical performance of the BP/ketjenblackmultiwalled carbon nanotubes composite for NIBs prepared by Xu et al. using the same process.[98]

Sonication is a process where sound energy is transferred to a solution (generally water based) where a material is dispersed. The energy released into the system can lead to the pulverisation of the particles of the dispersed material, reducing its particle size distribution. In some cases, it has also been used to prepare P-C composites, as reported by Subramaniyam et al.[99] According to Chen et al., the energy developed by this process can lead to the conversion of RP to BP, improving the performance of the resulting

composite with Li.[100] To date, this technique is not widely used, mainly because of the small amount of material that can be processed compared to the large amount of chemical waste that is produced. So far, composites prepared with this material have only been reported with Li and there are no studies related to Na and K.

Chemical synthesis of phosphorus can be described as a bottom-up approach compared to ball milling. In this case, in fact, RP is chemically synthesized in order to obtain particles with a narrow size distribution. A P precursor is generally reduced to produce amorphous P nanoparticles, identified in all past works as RP. Chang et al. reported a synthetic procedure where PI_3 is used as the precursor and ethylene glycol (EG) is used as the reducing agent (Figure 1.9a,b).[101] The addition of cetyl trimethyl ammonium bromide (CTAB) as a surfactant allowed the synthesis of spherical RP nanoparticles with an average size of 100 nm. The composite prepared with this material showed superior performance with Li, both in terms of cycle life and rate capability. The authors stated that this was related by the small uniform size of the spherical RP particles that shortens the transport distance of Li^+ ions alloying-dealloying and electrons. Zhou et al. also reported a synthesis where PCl_3 was used as the precursor that was reduced by NaN_3, with formation of RP particles and evolution of N_2 gas.[102] The formation of the gas during the reaction led to the formation of hollow spherical RP particles, which also showed superior performance with Li (Figure 1.9c,d). However, the low yields of these reactions (20-40%) and the large amount of chemical waste produced hinders the scalability of this procedure.

The methods described earlier all concern about the synthesis of a P/C composite that could work with Li, Na or K. However, although it is very clear that the particle size of RP has a heavy influence on the performance of the electrode, little is known about the ideal particle size distribution of RP that can prevent the failure of the electrode after few cycles. Ball milling is a great technique to investigate this effect, as it allows to control and reduce the particle size distribution of RP and to produce a composite in a safer manner compared to other techniques. Past reports, however, mainly concern the

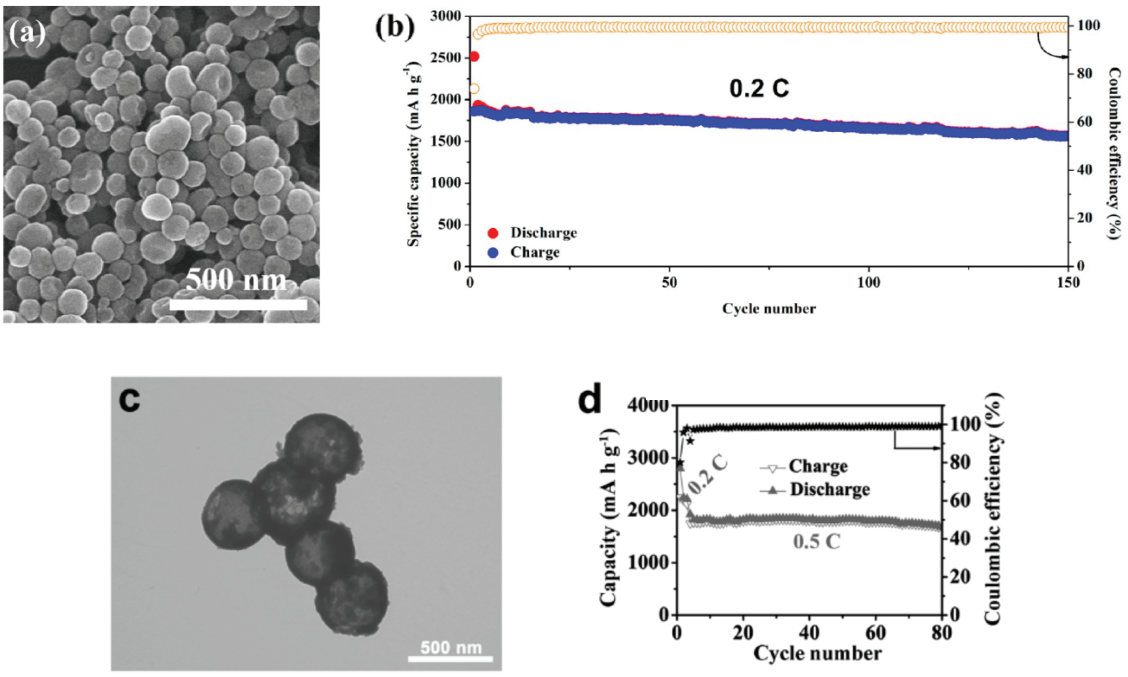


Figure 1.9: RP particles prepared by chemical synthesis. a,b) Spherical RP particles synthesized using PI_3 as precursor and reduced with EG and electrochemical performance from [101]. c,d) Hollow RP particles synthesized using PCl_3 and NaN_3 and electrochemical performance from [102].

synthesis of one composite and the comparison between different materials from different papers does not offer any new information, as different milling conditions operated with different instruments can lead to totally different results.[81, 92, 95] Ramireddy et al. in their work offered a comparison between two RP/C composite prepared in the same work.[82] However, their study was not systematic, as the two composites were prepared with different milling conditions and instruments. A systematic study (as for example testing composites that have different P particle size distribution or the effect of milling time with C) is therefore required in order to understand and optimize the performance of P/C composites, and this is one of the main concerns of this thesis. Moreover, the failure of the composite is often referred to in literature as a failure due to the fracture and pulverization of P particles.[92, 102, 103] However, there is no literature to date that shows the evidence of fractured or cracked P particles, differently from other alloying materials such as Si.[73] This study would be beneficial to understanding the mechanical

behaviour of P particles during the reaction, if fracture or cracking of the particle occurs and the possible causes of the failure of the material. This will also be covered in this thesis.

1.6 Aim of this project

As reported in this chapter, the production of anodes with both high capacity and low working potential is key for the development of alternative devices to LIBs, such as NIBs or KIBs. Alloying anodes, phosphorus in particular, are able to satisfy the requirements needed to make these devices competitive to LIBs. Unfortunately, issues related to this material, such as the volume expansion and resulting low cycle life, need to be addressed in detail to allow its use. The main focus of this project is to provide a better understanding of the mechanism of volume expansion related to the alloying reaction of phosphorus with Li, Na and K at a particle level. In particular, the attention of this study was focused on RP, being a good balance between cost and safety compared to the other allotropes. To achieve this, a detailed study of the mechanical and electrochemical properties of RP has been conducted. Furthermore, a study at the composite level is provided, with a detailed analysis of the effect of the particle-size distribution of RP and the mixing time of RP with graphite on the electrochemical properties of a RP-graphite composite. Finally, a brief study of the effects of different electrolytes on the performance of the composite is shown, opening up future studies on the optimisation of this aspect.

In Chapter 3, the study of the volume expansion and the evolution of stresses on the particle during the reaction is presented. Mechanical properties (such as Young's modulus, bulk modulus and toughness) and electrochemical properties (such as diffusivity) have been measured for the first time to allow the development of a model which simulates the expansion of particles and the stresses that accumulate on them. The model is then validated using in-situ TEM observations.

In Chapter 4, ball milling is used to study the effect of the particle size distribution on

the electrochemical properties of RP. A composite with different particle size distribution of RP and graphite is prepared and then tested with Na. Na is used to eliminate any contribution of graphite to the performance, due to the inability of Na to intercalate in graphite, and also because Na induces the largest volume expansion on RP among the three alkali ions. A particle-size distribution of RP can then be identified to allow for the synthesis of composites with long cycle life.

In Chapter 5, the composite optimized in Chapter 4 is tested with potassium, showing excellent performance, among the best performing anodes reported so far.

Finally, in Chapter 6, a comparison between the electrochemical performance of this composite with the three alkali metals is shown, focusing in particular on the effect of different electrolyte mixtures on the electrode performance.

1.7 References

1. Le Quéré, C. *et al.* Temporary reduction in daily global CO_2 emissions during the COVID-19 forced confinement. *Nature Climate Change* **10,** 647–653 (2020).
2. Davis, S. C. *et al. Transportation Energy Data Book* 35th ed. (2016).
3. Tarascon, J.-M. *et al.* Issues and challenges facing rechargeable lithium batteries. *Nature* **414,** 359–367 (2001).
4. Armand, M. *et al.* Building better batteries. *Nature* **451,** 652–657 (2008).
5. *Rechargeable Lithium Batteries* (Elsevier, 2015).
6. Bae, K. Y. *et al.* Energy-Density Improvement in Li-Ion Rechargeable Batteries Based on $LiCoO_2$ + LiV_3O_8 and Graphite + Li-Metal Hybrid Electrodes. *Materials* **12,** 2025 (2019).
7. Duan, J. *et al.* Building Safe Lithium-Ion Batteries for Electric Vehicles: A Review. *Electrochemical Energy Reviews* **3,** 1–42 (2020).

8. Whittingham, M. S. The Role of Ternary Phases in Cathode Reactions. *Journal of The Electrochemical Society* **123,** 315 (1976).

9. Mizushima, K. *et al.* Li_xCoO_2 (0<x<-1): A new cathode material for batteries of high energy density. *Materials Research Bulletin* **15,** 783–789 (1980).

10. *Batteries for Sustainability* (ed Brodd, R. J.) (Springer New York, New York, NY, 2013).

11. *Principles and Applications of Lithium Secondary Batteries* (ed Park, J.-K.) (Wiley-VCH Verlag GmbH & Co. KGaA, Weinheim, Germany, 2012).

12. Liu, Q. *et al.* Approaching the capacity limit of lithium cobalt oxide in lithium ion batteries via lanthanum and aluminium doping. *Nature Energy* **3,** 936–943 (2018).

13. Chen, H. *et al.* Progress in electrical energy storage system: A critical review. *Progress in Natural Science* **19,** 291–312 (2009).

14. Schäfer, A. W. *et al.* Technological, economic and environmental prospects of all-electric aircraft. *Nature Energy* **4,** 160–166 (2019).

15. *Electric Vehicle Outlook 2020* (BloombergNEF, 2020).

16. Tarascon, J.-M. Is lithium the new gold? *Nature Chemistry* **2,** 510–510 (2010).

17. *Mineral Commodity Summaries* tech. rep. (2020).

18. Rajagopalan, R. *et al.* Advancements and Challenges in Potassium Ion Batteries: A Comprehensive Review. *Advanced Functional Materials* **30,** 1909486 (2020).

19. Ji, B. *et al.* A fluoroxalate cathode material for potassium-ion batteries with ultra-long cyclability. *Nature Communications* **11,** 1225 (2020).

20. Liu, C. *et al.* Understanding electrochemical potentials of cathode materials in rechargeable batteries. *Materials Today* **19,** 109–123 (2016).

21. Komaba, S. *et al.* Electrochemically Reversible Sodium Intercalation of Layered $NaNi_{0.5}Mn_{0.5}O_2$ and $NaCrO_2$. *ECS Transactions* **16,** 43–55 (2019).

22. Yabuuchi, N. *et al.* P2-type $Na_x[Fe_{1/2}Mn_{1/2}]O_2$ made from earth-abundant elements for rechargeable Na batteries. *Nature Materials* **11,** 512–517 (2012).

23. Deng, T. *et al.* Layered P2-Type $K_{0.65}Fe_{0.5}Mn_{0.5}O_2$ Microspheres as Superior Cathode for High-Energy Potassium-Ion Batteries. *Advanced Functional Materials* **28,** 1800219 (2018).

24. Kim, H. *et al.* Investigation of Potassium Storage in Layered P3-Type $K_{0.5}MnO_2$ Cathode. *Advanced Materials* **29,** 1702480 (2017).

25. Hosaka, T. *et al.* Research Development on K-Ion Batteries. *Chemical Reviews* **120,** 6358–6466 (2020).

26. Hurlbutt, K. *et al.* Prussian Blue Analogs as Battery Materials. *Joule* **2,** 1950–1960 (2018).

27. Zhu, B. *et al.* Towards high energy density lithium battery anodes: silicon and lithium. *Chemical Science* **10,** 7132–7148 (2019).

28. Andre, D. *et al.* Future high-energy density anode materials from an automotive application perspective. *Journal of Materials Chemistry A* **5,** 17174–17198 (2017).

29. Goriparti, S. *et al.* Review on recent progress of nanostructured anode materials for Li-ion batteries. *Journal of Power Sources* **257,** 421–443 (2014).

30. Hassoun, J. *et al.* Review—Advances in Anode and Electrolyte Materials for the Progress of Lithium-Ion and beyond Lithium-Ion Batteries. *Journal of The Electrochemical Society* **162,** A2582–A2588 (2015).

31. Li, Y. *et al.* Intercalation chemistry of graphite: alkali metal ions and beyond. *Chemical Society Reviews* **48,** 4655–4687 (2019).

32. Moriwake, H. *et al.* Why is sodium-intercalated graphite unstable? *RSC Advances* **7,** 36550–36554 (2017).

33. Okamoto, Y. Density Functional Theory Calculations of Alkali Metal (Li, Na, and K) Graphite Intercalation Compounds. *The Journal of Physical Chemistry C* **118,** 16–19 (2014).

34. Jian, Z. *et al.* Carbon Electrodes for K-Ion Batteries. *Journal of the American Chemical Society* **137,** 11566–11569 (2015).

35. Zhang, W. *et al.* Approaching high-performance potassium-ion batteries via advanced design strategies and engineering. *Science Advances* **5,** eaav7412 (2019).

36. Stevens, D. A. *et al.* High Capacity Anode Materials for Rechargeable Sodium-Ion Batteries. *Journal of The Electrochemical Society* **147,** 1271 (2000).

37. Dou, X. *et al.* Hard carbons for sodium-ion batteries: Structure, analysis, sustainability, and electrochemistry. *Materials Today* **23,** 87–104 (2019).

38. Vaalma, C. *et al.* A cost and resource analysis of sodium-ion batteries. *Nature Reviews Materials* **3,** 18013 (2018).

39. Lu, J. *et al.* High-Performance Anode Materials for Rechargeable Lithium-Ion Batteries. *Electrochemical Energy Reviews* **1,** 35–53 (2018).

40. Pierson, H. O. *Handbook of Carbon, Graphite, Diamond and Fullerenes* (Noyes Publications, 1993).

41. Allart, D. *et al.* Model of Lithium Intercalation into Graphite by Potentiometric Analysis with Equilibrium and Entropy Change Curves of Graphite Electrode. *Journal of The Electrochemical Society* **165,** A380–A387 (2018).

42. Asenbauer, J. *et al.* The success story of graphite as a lithium-ion anode material – fundamentals, remaining challenges, and recent developments including silicon (oxide) composites. *Sustainable Energy & Fuels* (2020).

43. Nishitani, R. *et al.* In situ observation of staging in potassium-graphite intercalation compounds. *Physical Review B* **27,** 6572–6575 (1983).

44. Xu, J. *et al.* Recent Progress in Graphite Intercalation Compounds for Rechargeable Metal (Li, Na, K, Al)-Ion Batteries. *Advanced Science* **4,** 1700146 (2017).

45. Sun, N. *et al.* Facile synthesis of high performance hard carbon anode materials for sodium ion batteries. *Journal of Materials Chemistry A* **3,** 20560–20566 (2015).

46. Wu, F. *et al.* Expanding Interlayer Spacing of Hard Carbon by Natural K + Doping to Boost Na-Ion Storage. *ACS Applied Materials & Interfaces* **10,** 27030–27038 (2018).

47. Li, Y. *et al.* Amorphous monodispersed hard carbon micro-spherules derived from biomass as a high performance negative electrode material for sodium-ion batteries. *Journal of Materials Chemistry A* **3,** 71–77 (2015).

48. Yi, T.-F. *et al.* Recent advances of $Li_4Ti_5O_{12}$ as a promising next generation anode material for high power lithium-ion batteries. *Journal of Materials Chemistry A* **3,** 5750–5777 (2015).

49. Borghols, W. J. H. *et al.* Impact of Nanosizing on Lithiated Rutile TiO_2. *Chemistry of Materials* **20,** 2949–2955 (2008).

50. Dambournet, D. *et al.* Tailored Preparation Methods of TiO_2 Anatase, Rutile, Brookite: Mechanism of Formation and Electrochemical Properties †. *Chemistry of Materials* **22,** 1173–1179 (2010).

51. Amine, K. *et al.* Nanostructured Anode Material for High-Power Battery System in Electric Vehicles. *Advanced Materials* **22,** 3052–3057 (2010).

52. Yan, Z. *et al.* A tightly integrated sodium titanate-carbon composite as an anode material for rechargeable sodium ion batteries. *Journal of Power Sources* **274,** 8–14 (2015).

53. Liu, C. *et al.* Potassium vanadate $K_{0.23}V_2O_5$ as anode materials for lithium-ion and potassium-ion batteries. *Journal of Power Sources* **389,** 77–83 (2018).

54. Yu, S.-H. *et al.* Conversion Reaction-Based Oxide Nanomaterials for Lithium Ion Battery Anodes. *Small* **12,** 2146–2172 (2016).

55. Alcántara, R. *et al.* $NiCo_2O_4$ Spinel: First Report on a Transition Metal Oxide for the Negative Electrode of Sodium-Ion Batteries. *Chemistry of Materials* **14,** 2847–2848 (2002).

56. Lakshmi, V. *et al.* Nanocrystalline SnS_2 coated onto reduced graphene oxide: demonstrating the feasibility of a non-graphitic anode with sulfide chemistry for potassium-ion batteries. *Chemical Communications* **53,** 8272–8275 (2017).

57. Yu, D. Y. W. *et al.* Bulk antimony sulfide with excellent cycle stability as next-generation anode for lithium-ion batteries. *Scientific Reports* **4,** 4562 (2015).

58. Zheng, F. *et al.* Sn – MoS_2 – C@C Microspheres as a Sodium-Ion Battery Anode Material with High Capacity and Long Cycle Life. *Chemistry - A European Journal* **23,** 5051–5058 (2017).

59. Liu, Y. *et al.* Boosting potassium-ion batteries by few-layered composite anodes prepared via solution-triggered one-step shear exfoliation. *Nature Communications* **9,** 3645 (2018).

60. Wang, F. *et al.* Conversion Reaction Mechanisms in Lithium Ion Batteries: Study of the Binary Metal Fluoride Electrodes. *Journal of the American Chemical Society* **133,** 18828–18836 (2011).

61. Du, Y. *et al.* In Situ Growth of CoP_3/Carbon Polyhedron/CoO/NF Nanoarrays as Binder-Free Anode for Lithium-Ion Batteries with Enhanced Specific Capacity. *Small* **16,** 1907468 (2020).

62. Shi, Y. *et al.* Co_3O_4 and its composites for high-performance Li-ion batteries. *Chemical Engineering Journal* **343,** 427–446 (2018).

63. Liu, X. *et al.* Co_3O_4/C nanocapsules with onion-like carbon shells as anode material for lithium ion batteries. *Electrochimica Acta* **100,** 140–146 (2013).

64. Li, H. *et al.* Coating Fe_2O_3 with graphene oxide for high-performance sodium-ion battery anode. *Composites Communications* **1,** 48–53 (2016).

65. Zhao, W. *et al.* Carbon-coated CoP_3 nanocomposites as anode materials for high-performance sodium-ion batteries. *Applied Surface Science* **445,** 167–174 (2018).

66. Sultana, I. *et al.* K-ion and Na-ion storage performances of Co_3O_4–Fe_2O_3 nanoparticle-decorated super P carbon black prepared by a ball milling process. *Nanoscale* **9,** 3646–3654 (2017).

67. Cabana, J. *et al.* Beyond Intercalation-Based Li-Ion Batteries: The State of the Art and Challenges of Electrode Materials Reacting Through Conversion Reactions. *Advanced Materials* **22,** E170–E192 (2010).

68. Li, J. *et al.* Phase evolution of conversion-type electrode for lithium ion batteries. *Nature Communications* **10,** 2224 (2019).

69. Huggins, R. A. Lithium alloy negative electrodes. *Journal of Power Sources* **81-82,** 13–19 (1999).

70. Wang, J. *et al.* Recent progress of silicon composites as anode materials for secondary batteries. *RSC Advances* **6,** 87778–87790 (2016).

71. Sultana, I. *et al.* Potassium-Ion Battery Anode Materials Operating through the Alloying-Dealloying Reaction Mechanism. *Advanced Functional Materials* **28,** 1703857 (2018).

72. Beaulieu, L. Y. *et al.* Colossal Reversible Volume Changes in Lithium Alloys. *Electrochemical and Solid-State Letters* **4,** A137 (2001).

73. Liu, X. H. *et al.* Size-Dependent Fracture of Silicon Nanoparticles During Lithiation. *ACS Nano* **6,** 1522–1531 (2012).

74. McDowell, M. T. *et al.* In Situ TEM of Two-Phase Lithiation of Amorphous Silicon Nanospheres. *Nano Letters* **13,** 758–764 (2013).

75. Obrovac, M. N. *et al.* Alloy Negative Electrodes for Li-Ion Batteries. *Chemical Reviews* **114,** 11444–11502 (2014).

76. Baggetto, L. *et al.* Germanium as negative electrode material for sodium-ion batteries. *Electrochemistry Communications* **34,** 41–44 (2013).

77. Zhang, W. *et al.* Unraveling the effect of salt chemistry on long-durability high-phosphorus-concentration anode for potassium ion batteries. *Nano Energy* **53,** 967–974 (2018).

78. Liu, Y. *et al.* Ultrasmall Sn Nanoparticles Embedded in Carbon as High-Performance Anode for Sodium-Ion Batteries. *Advanced Functional Materials* **25,** 214–220 (2015).

79. Zhang, W. *et al.* Phosphorus-Based Alloy Materials for Advanced Potassium-Ion Battery Anode. *Journal of the American Chemical Society* **139,** 3316–3319 (2017).

80. Qian, J. *et al.* Reversible 3-Li storage reactions of amorphous phosphorus as high capacity and cycling-stable anodes for Li-ion batteries. *Chemical Communications* **48,** 8931 (2012).

81. Kim, Y. *et al.* An Amorphous Red Phosphorus/Carbon Composite as a Promising Anode Material for Sodium Ion Batteries. *Advanced Materials* **25,** 3045–3049 (2013).

82. Ramireddy, T. *et al.* Phosphorus–carbon nanocomposite anodes for lithium-ion and sodium-ion batteries. *Journal of Materials Chemistry A* **3,** 5572–5584 (2015).

83. Sultana, I. *et al.* High capacity potassium-ion battery anodes based on black phosphorus. *Journal of Materials Chemistry A* (2017).

84. Han, X. *et al.* Promise and Challenge of Phosphorus in Science, Technology, and Application. *Advanced Functional Materials* **28,** 1803471 (2018).

85. DeWitt, T. W. *et al.* Conversion of Liquid White Phosphorus to Red Phosphorus. I. Kinetics of the Reaction 1. *Journal of the American Chemical Society* **68,** 2305–2309 (1946).

86. Yi, Y. *et al.* Two-dimensional black phosphorus: Synthesis, modification, properties, and applications. *Materials Science and Engineering: R: Reports* **120,** 1–33 (2017).

87. *Black Phosphorus* (eds Inamuddin *et al.*) (Springer International Publishing, Cham, 2020).

88. Kim, S. *et al.* Orientation-Dependent Intercalation Channels for Lithium and Sodium in Black Phosphorus. *Advanced Materials* **31,** 1904623 (2019).

89. Mayo, M. *et al.* Ab Initio Study of Phosphorus Anodes for Lithium- and Sodium-Ion Batteries. *Chemistry of Materials* **28,** 2011–2021 (2016).

90. Yang, W. *et al.* First-Principles Study of Black Phosphorus as Anode Material for Rechargeable Potassium-Ion Batteries. *Electronic Materials Letters* **16,** 89–98 (2020).

91. Marino, C. *et al.* Nanoconfined phosphorus in mesoporous carbon as an electrode for Li-ion batteries: Performance and mechanism. *Journal of Materials Chemistry* **22,** 22713–22720 (2012).

92. Park, C.-M. *et al.* Black Phosphorus and its Composite for Lithium Rechargeable Batteries. *Advanced Materials* **19,** 2465–2468 (2007).

93. Sottmann, J. *et al.* Chemical Structures of Specific Sodium Ion Battery Components Determined by Operando Pair Distribution Function and X-ray Diffraction Computed Tomography. *Angewandte Chemie - International Edition* **56,** 11385–11389 (2017).

94. Marbella, L. E. *et al.* Sodiation and Desodiation via Helical Phosphorus Intermediates in High-Capacity Anodes for Sodium-Ion Batteries. *Journal of the American Chemical Society* **140,** 7994–8004 (2018).

95. Qian, J. *et al.* High Capacity and Rate Capability of Amorphous Phosphorus for Sodium Ion Batteries. *Angewandte Chemie* **125,** 4731–4734 (2013).

96. Komaba, S. *et al.* Fluorinated Ethylene Carbonate as Electrolyte Additive for Rechargeable Na Batteries. *ACS Applied Materials & Interfaces* **3,** 4165–4168 (2011).

97. Zhu, Y. *et al.* Red Phosphorus–Single-Walled Carbon Nanotube Composite as a Superior Anode for Sodium Ion Batteries. *ACS Nano* **9,** 3254–3264 (2015).

98. Xu, G.-L. *et al.* Nanostructured Black Phosphorus/Ketjenblack–Multiwalled Carbon Nanotubes Composite as High Performance Anode Material for Sodium-Ion Batteries. *Nano Letters* **16,** 3955–3965 (2016).

99. Subramaniyam, C. M. *et al.* Unlocking the potential of amorphous red phosphorus films as a long-term stable negative electrode for lithium batteries. *Journal of Materials Chemistry A* **5,** 1925–1929 (2017).

100. Chen, X. *et al.* A black/red phosphorus hybrid as an electrode material for high-performance Li-ion batteries and supercapacitors. *Journal of Materials Chemistry A* **5,** 6581–6588 (2017).

101. Chang, W.-C. *et al.* Solution Synthesis of Iodine-Doped Red Phosphorus Nanoparticles for Lithium-Ion Battery Anodes. *Nano Letters* **17,** 1240–1247 (2017).

102. Zhou, J. *et al.* Wet-Chemical Synthesis of Hollow Red-Phosphorus Nanospheres with Porous Shells as Anodes for High-Performance Lithium-Ion and Sodium-Ion Batteries. *Advanced Materials* **29,** 1700214 (2017).

103. Liu, W. *et al.* Recent progress in phosphorus based anode materials for lithium/sodium ion batteries. *Energy Storage Materials* **16,** 290–322 (2019).

Chapter 2

Instruments and Methods

2.1 Synthesis Techniques

2.1.1 Ball milling

The RP-graphite composite used in chapters 3-6 was prepared by a two-steps ball milling procedure. The first step concerns the reduction and control of the particle size of RP. 3.4 g of commercial RP (Fisher, -100 mesh, 98.9%) was placed in a 45 ml zirconia jar (Fritsch Pulverisette 7) with the addition of 10 ml of EG (Sigma Aldrich, 99.8%) and 180 zirconia balls (5 mm ⌀, balls-to-powder mass ratio: 70:1), then sealed in argon atmosphere. The material was wet milled at a milling frequency of 500 rpm for up to 60 h. The sample was collected from the jar and washed 3 times with equal volumes of water and ethanol by centrifugation at 14,000 rpm. Then, the resulting material was dried at 100 °C under vacuum overnight. The preparation of the RP-graphite composite takes place in the second step. The RP obtained from the first step is mixed with graphite (TIMCAL, SFG6) with a P/C mass ratio of 7/3. The mixture is placed in a 12 ml stainless steel jar (Retsch PM100) with the addition of 5 stainless steel balls (10 mm ⌀). The balls-to-powder mass ratio was 20:1. The mixture was then ball milled at a milling frequency of 500 rpm for a maximum time of 48 h. The resulting composite was then stored in a

glovebox.

In Chapter 3, the first step of this procedure (the wet milling of RP) was used to prepare ball milled RP particles that have been tested in an in-situ TEM to study the volume expansion of RP upon alloying with Li, Na and K. A RP-graphite composite prepared by wet milling RP for 60 h and mixing it with graphite for 48 h was used as active material in the GITT experiments.

In Chapter 4, the two step procedure was used to optimize the particle-size distribution of RP in a RP-grahite composite. The composites prepared to study the effect of the particle-size distribution of RP were prepared by wet milling RP for 12, 18 and 60 h and then the RP was ball milled with graphite for 24 h. To test the effect of the mixing time with graphite, the RP was wet milled for 60 h, then three composites were prepared with different mixing time with graphite: 1, 24 and 48 h.

In Chapter 5 and 6, the RP-composite that is shown was prepared by wet milling RP for 60 h, then mixed with graphite for 48 h.

2.1.2 Chemical synthesis

Spherical RP particles used in Chapter 3 were synthesized adapting a procedure reported by Chang et al.[1] The entire procedure was operated in a glovebox to prevent oxidation of the chemically synthesized particles. PI_3 (99%, Sigma Aldrich) was dissolved in iodobenzene (98%, Sigma Aldrich) to obtain a solution with a 1.5 M concentration. A second solution containing EG (99.8%, Sigma aldrich) and CTAB (98%, Sigma aldrich) with a 0.016 M concentration was prepared. The second solution (15 ml) was put under vigorous stirring at 1000 rpm using a magnetic stirrer and the PI_3 solution (5 ml) was added dropwise over 5 minutes. The color of the solution quickly changes to bright orange, indicative of the success of the reaction. The mixture was stirred for 30 minutes, then it was collected in a centrifuge tube. The powder was washed three times using dry ethanol and collected by centrifugation at 14,000 rpm. The product was then dried at 100 °C overnight under vacuum and stored in a glovebox. This procedure allows for the production of spherical RP particles with an average particle size of 130 nm.

In Chapter 3, this procedure is used to prepare spherical RP particles that are tested with an in-situ TEM to study the volume expansion of RP upon alloying with Li, Na and K.

2.1.3 Electrode production

The electrodes produced in this work concern two materials in particular:

- RP-graphite composite
- graphite (pristine SFG6)

The electrodes containing RP-graphite composites were prepared following the procedure explained below.

The RP-graphite composite, was mixed together with Super P carbon (TIMCAL) and polyacrylic acid (PAA) binder (450 kDa, Sigma Aldrich) in a 8:1:1 mass ratio in an agate mortar for about 15 minutes. PAA polymer was chosen as poor performance have been reported with PVDF and CMC is only soluble in water, which could react with RP to form oxides.[2] Its length was also accurately selected among a shorter (1.8 KDa) and a longer chain (3000 KDa) as it results in the formation of a highly stable casting on the current collector. NMP was then added dropwise as the solvent to the mixture to allow the solubilization of the binder and the formation of a homogeneous slurry. The slurry was hand mixed for another 15 minutes. The obtained ink was cast on a copper foil using a blade. The casting was then left to dry overnight to allow the slow evaporation of the solvent from the material, then it was heated up to 100 °C under vacuum to completely remove any trace of solvent. The mass loading of phosphorus on the casting was in the order of 1-1.2 $\mathrm{mg\,cm^{-2}}$. For the electrochemical experiments, disks 1 cm ⌀ large were cut from the casting using a hole puncher.

The electrodes containing pristine SFG6 were prepared by hand mixing graphite (TIMCAL) and PAA binder (450 kDa, Sigma Aldrich) in an agate mortar in a 9:1 mass ratio, with a procedure similar to the one used to prepare RP-graphite containing electrodes. The resulting casting had a mass loading of graphite of about 1 $\mathrm{mg\,cm^{-2}}$. Disks 1 cm ⌀ large were cut from the casting using a hole puncher.

This process was used to prepare all the electrodes shown in this thesis.

The electrodes that have been used for the Raman operando experiment in Chapter 5 have been prepared following the same procedure, with the only exception that a copper grid was used a current collector instead of a copper foil. Detailed procedure of the preparation of the operando cell is provided in Section 2.2.2. This procedure was used in the operando Raman experiment, shown in Chapter 5.

2.2 Material Characterization

2.2.1 DLS

Dynamic light scattering (DLS) is a technique that allows the measurement of the particle-size distribution of a sample using the phenomenon of light scattering. This technique is based on the rate of Brownian motion of the particles in a solvent. Big particles in fact diuse slower than smaller particles. A light source, a LASER (Light Amplification by Stimulated Emission of Radiation) in this case, is used to illuminate the sample and the light is then scattered by the particles suspended in it. Due to the motion of the particles in the solution, the intensity of the light oscillates and the fluctuation of intensity is measured over time. This is strictly dependent on the size of the particles since small particles will diffuse faster (resulting in a faster fluctuation) then big particles. Consecutive snapshots of the scattered intensity are taken over time and correlated to the starting one (autocorrelation function). After some time the scattered intensity plot will have close to 0 correlation to the starting pattern, because of the motion of the particles. The time needed to reach this zero-correlation point depends on the diffusion speed of the particles and so on their size. By fitting the autocorrelation function, we can extract the translational diffusion coefficient D. This is used to calculate the hydrodynamic size of the particles, which is the size of a spherical particle that would move at the same speed as the particle sampled. This is done using the Stokes-Einstein equation (Eq. 2.1):

$$\mathrm{d_h} = \frac{\mathrm{kT}}{3\pi\eta\mathrm{D}} \tag{2.1}$$

where k is the Boltzmann constant, T is the temperature, η is the viscosity of the solution and D is the traslational diffusion coefficient. The result is a plot of the intensity scattered by different sizes of particles present in the sample. This can then be converted to a number or volume based distribution.

In this work, a Horiba DLS analyzer. The sample was prepared by mixing 20 mg of

the powder with 20 mg of distilled water. The solution was then sonicated using a probe sonicator for 1 minute to allow for the separation of the aggregates. The dispersion was then added to the main tank of the DLS analyzer, where the analysis was performed. Two lasers, 633 nm and 466 nm were used to determine the particle size distribution.

In Chapter 3, DLS is used to characterize the particle size distribution of commercial RP and ball milled commercial RP particles.

In Chapter 4, this technique is used to measure and control the particle size distribution of RP during wet milling, and also to measure the particle size distribution of the RP-graphite composite.

2.2.2 Raman

Raman spectroscopy, named after the homonymous effect, is a method that allows the study of surfaces of materials. In this method, light radiation coming from a LASER source interacts with matter. This interaction can occurr in three different ways:

- the radiation is scattered back without releasing or acquiring energy (Rayleigh scattering);
- the radiation releases energy to the sample, and the radiation scattered has a lower energy (Stokes);
- the radiation acquires energy from the sample, and the radiation scattered has a higher energy (anti-Stokes).

The interaction between the radiation and the matter induces a dipole moment to the system, according to the polarizability tensor of the sample:

$$\mu = \alpha E \tag{2.2}$$

where μ is the dipole moment of the sample, α is the polarizability tensor and E the electric field. The dipole moment is non-zero if the polarizability of the vibration modes of the sample at equilibrium is also non-zero:

$$\frac{\delta\alpha}{\delta x_{eq.}} \neq 0 \tag{2.3}$$

This condition is true in cases of vibrations like symmetric stretching or bending. A LASER source is used because of the low intensity of the Raman effect. The use of a high intensity, monochromatic and coherent source makes the phenomenon easier to detect and measure.

The instrument used in this work is a Renishaw InVia microscope. In Chapter 3, this technique is used to characterize chemically synthesized spherical RP particles, commercial RP and ball milled commercial RP. A 785 nm laser was used. Single acquisitions

were made with a 1% laser intensity, for 1 s exposure time. In Chapter 4 and 5, this method is used to study the changes occurring to RP when wet milled with EG and ball milled with graphite. In Chapter 4, a 785 nm laser was used. Single acquisitions were made with a 1% laser intensity, for 1 s exposure time. In Chapter 5, the cell used for the Raman operando experiment is a modified 2032 coin cell where a 4 mm ⌀hole was drilled from the positive side and a sapphire window (7mm ⌀) was glued with epoxy to allow the sampling of the electrode material inside the cell. A schematic of the cell is shown in Figure 2.1. The assembling procedure is the same followed for standard coin cells.

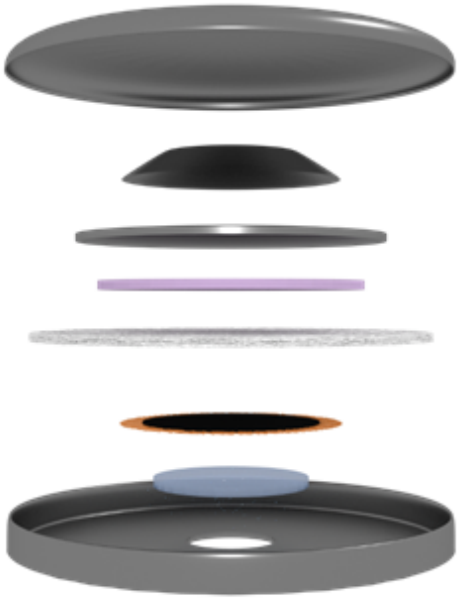


Figure 2.1: a) Schematic of the cell used for the Raman operando experiment. From top to bottom: cap, spring, spacer, K disk, glass fiber separator, copper grid with electrode material, sapphire window, case.

A 512 nm laser was used for the operando Raman experiment. 10 stacked acquisitions were performed using a 5% laser intensity for a 10 s exposure time.

2.2.3 X-ray diffraction

X-ray Diffraction (XRD) is a method used to analyze crystal structures of materials. This method uses a coherent X-Ray radiation that is directed to the sample. The radiation can interact elastically with the atoms in the crystal structure, and are scattered conserving their energy:

$$\Delta E = E_s - E_i = 0 \tag{2.4}$$

Where E_s is the energy of the scattered radiation and E_i is the energy of the incident radiation. Based on the scattering angle, the radiation waves can interfere with each other in a destructive or constructive way. The constructive interference is described by Bragg's law:

$$n\lambda = 2d\sin(\vartheta) \tag{2.5}$$

where n is an integer number (generally 1), λ is the wavelength of the radiation, d is the distance between two crystallographic planes and ϑ is the glancing angle between the radiation and the crystallographic plane. By varying the glancing angle, we obtain a diffractogram that reports the intensity of the diffracted radiation with respect of the angle (reported as 2ϑ). Peaks are located where the Bragg's relation is satisfied and so confirms the existence of crystallographic planes that are separated by d. With this method is therefore possible the identification of crystalline phases that are present in is a sample, based on the radiation that is diffracted by it.

The instrument used in this work is Rigaku Smartlab X-Ray diffrattometer with a Cu $K_{\alpha 1}$ radiation and a 3 kW rotating anode X-Ray generator. Patterns were collected in $\vartheta/2\vartheta$ with a step size of 0.02.

In Chapter 3, XRD is used to characterize the RP samples that are mechanically and electrochemically tested, to check for the presence of impurities.

In Chapter 4 and 5, XRD are used to study the changes occurring to the RP-graphite

composite after ball milling. This technique is also used to find crystalline impurities that could form after wet milling of RP in Chapter 4.

2.2.4 Photoelectron spectroscopy

Photoelectron spectroscopy (PES) is a surface analysis technique that allows to quantitatively measure the elemental composition of the first few nanometers of the surface of a sample. In this technique, when a beam (X-ray or UV radiation) irradiates the sample, the energy can be absorbed by the core electrons of the atoms present on the surface. These electron can then be ejected as photoelectrons. The kinetic energy of these photoelectrons ($KE_{photoelectron}$) can be measured by an energy analyser and, knowing the energy of the incident beam (E_{beam}), it is possible to calculate their binding energy (E_b), which is unique for specific elements:

$$E_b = E_{beam} - KE_{photoelectron} - \varphi \tag{2.6}$$

where φ is the work function that is specific to the spectrometer.

In this work, energy-tuned PES measurements were performed at the Surface and Interface Structural Analysis beamline (I09) at Diamond Light Source in Oxfordshire, UK. Hard X-ray PES (HAXPES) and soft X-ray PES (SOXPES) measurements were performed using excitation energies of 2350 eV and 3^{rd} order light 7050 eV monochromatized by a Si(111) double-crystal monochromator for HAXPES and 1090 eV using a plane grating monochromator for SOXPES. A pass energy of 50 eV for soft X-rays and pass energies of 70 eV and 200 eV for 2.35 keV and 7.05 keV were used to record spectra. A VG Scienta EW4000 analyzer was used to analyze the signal. The spot is estimated to be approximately 300 µm

In Chapter 4, the experiment was made on the RP-graphite composite ball milled for 48 h. The material was loaded on a copper plate via a copper tape and loaded at the synchrotron. The binding energies of the spectra were calibrated on the C=C sp^2 bond from carbon black, which is located at 284.2 eV in the C1s spectra. CasaXPS was used to analyze the spectra. The fit was operated using a Shirley background and a Gaussian/Lorentzian peak shape GL(30) was used. The probing depth shown in Chapter 4

was calculated using the TPP-2M equation for both P and C.

2.2.5 Scanning electron microscopy

Scanning electron microscopy (SEM) is a microscopy technique where the image of the sample is generated by the use of an electron beam. The electron beam is generated in the instrument using a source such as a tungsten filament cathode, a lantanum hexaboride (LaB_6) wire or a field emission gun. The beam is then accelerated in the instrument via a potential difference and is focused on the sample. The interaction produces the emission of radiation or electrons from the sample which can be detected by an analyzer. The electrons that can be emitted by the sample consist of mainly two types:

- backscattered electrons (these are electrons that elastically interact with the sample);
- secondary electrons (electrons that are ejected from the conduction band of the sample, due to an inelastic interaction of the electron beam);

The secondary electrons make up the majority of the electrons detected by the analyzer. When they interact with the detector, a current is produced which is then converted to image. The intensity of the contrast in the image directly depends on the morphology of the sampled material, which is why this method allows for the study of the morphology of nanosized and microsized materials. Energy dispersive X-ray analysis (EDX) is often used with this technique. The radation emitted from the sample is collected and its energy can be traced back to specific elements in the sample. The technique can be used for elemental analysis.

In this work, a Zeiss Merlin SEM with an acceleration voltage of 1kV and a probe current of 100 µA was used. The samples were loaded on a copper grid with a thin holey carbon film. The powder samples were prepared by dispersion of the powders in acetonitrile and added dropwise to the copper grid in a glovebox. Energy dispersive X-ray analysis (EDX) was performed to analyze the elemental composition of the samples.

In Chapter 4, this technique is used to investigate the morphology of commercial RP and ball milled RP. Moreover, the samples used for the cross sectional analysis were

prepared using RP-graphite electrodes (preparation explained in Section 2.1.3). The electrodes were cut and the side was polished using a Precision Etching Coating System (PECS) Gatan II. EDX analysis was also performed on both the powder samples and the cross section of the electrodes to analyze the elemental distribution.

2.2.6 Transmission electron microscopy

Transmission electron microscopy (TEM) is a technique used for the study of the morphology of a sample. In a TEM, an electron beam is generated using an electron gun and is focused on the sample using condenser lens. The beam is accelerated by an applied potential and passes through the sample (which is deposited onto a nickel or copper grid). Parts of the beam are transmitted depending on the thickness and the electron density of the sample. The transmitted beam is focused by the objective lens on a phosphor screen, and is then converted to image. The darker areas on the image show the zones where fewer electrons were able to pass through the sample, while brighter areas show the zones where the intensity of the transmitted beam is higher.

In Chapter 3, the in-situ TEM experiments were performed using FEI Tecnai G2 F20 X-Twin TEM at the acceleration voltage of 200 kV. A STM-TEM holder (Nanofactory Instruments Dual-Probe) was used to apply bias between RP and Li, Na or K metal electrodes. Cu and W wires were used to load RP and the alkali metals, respectively. A relative bias of -1.5 V was applied to cause the alkali ions to be transferred to RP through the natural oxide layer present on the alkali metal. These experiments were performed with our collaborators Prof. Hyun-Wook Lee and Tae-Ung Wi (Ulsan National Institute of Science and Technology, Ulsan, South Korea). The data from the experiments performed on the spherical RP particles were analysed by a Matlab script that measured the change in size of the particles by fitting their shape using ellipsoids. The data from the experiments performed on the ball milled RP particles were instead analysed by ImageJ and the sizes measured using a line tool. In Chapter 4 and Chapter 5, a JEOL 3000F Field emission gun TEM operated at 300 kV was used to characterize the composites. EDX measurement in the TEM were performed using a built-in Oxford Instruments X-Max detector. The TEM analysis on the composite was performed by a DPhil student in the group, Albert W. Xiao (University of Oxford).

2.2.7 Pthycographic X-ray computer tomography

Pthycographic X-ray computer tomography (PXCT) is an imaging technique that is based on the analysis of the interference pattern of an incident X-ray beam with a sample. Monocromatic X-rays are directed to the sample which is rotated through 180 degrees. For each angle, the radiation scattered by the sample is collected as a diffraction pattern. The collected patterns are then processed through an iterative algorithm which provides a grayscale 3D reconstructed model of the sample analized, where the brightness is related to the absorption of the X-rays in the sample. The absorption coefficient of the beam is related to the density and atomic number of different materials in the sample, and this allows for a qualitative analysis of the morphology and composition of the sample.

In this work, PXCT analysis shown in Chapter 5 was conducted on the I13 beamline at Diamond Light Source in the United Kingdom. The RP-graphite electrode samples were prepared as pristine then fragmented and loaded into a borosilicate glass capillary (diameter of capillary = 100 µm). The end of capillary was sealed by polymer clay and cyanoacrylate adhesive. The capillary was prepared in an Ar-filled glovebox to prevent air exposure of sample. A monochromatic beam of 15 k eV was selected with a fixed sample-detector distance of 9.5 m, and the spatial resolution of each pixel was 55 nm. For each ptychographic tomography scan of phosphorus sample, 900 projections were taken equiangularly from -90 to 90. For each projection, a region of $26\,\mu m^2 \times 26\,\mu m^2$ was scanned with a step size of $1.5\,\mu m^2 \times 1.5\,\mu m^2$, with an exposure time of 0.05 s. The obtained projections were processed by using the software Blender. The components that have been identified in the acquired data were subdivided into three regions: RP, C (graphite) and C (Super P). Light grey areas present in the sample were assigned to RP, being the component with the highest electron density in the sample. Dark grey areas were identified as Super P carbon, being the material with the lowest density in the sample, while the remaining areas were identified as graphite.

The PXCT analysis on the electrode material was performed by a postdoc in the group, Dr. Hyeon Jeong Lee (University of Oxford) at Diamond Light source.

2.2.8 Surface area analysis

The surface area of a sample can be measured by considering the dynamics of a gas that adsorbs/desorbs from it. This theory was developed by S. Brunauer, P.H. Emmett and E. Teller, who developed the BET equation that describes the multy-layer adsorption dynamic of a gas on a material:

$$\frac{1}{v[(P_0/P)-1]} = \frac{1}{v_m c} + \frac{c-1}{v_m c}\left(\frac{P}{P_0}\right) \tag{2.7}$$

Where P and P_0 are the equilibrium and saturation pressure of the adsorbates, v is the volume of adsorbed gas, v_m is the volume of the monolayer of adsorbed gas and c is the BET constant, expressed as

$$c = \exp\left(\frac{E_1 - E_L}{RT}\right) \tag{2.8}$$

where E_1 and E_L are the heat of adsorption of the first adsorbed layer and for higher layers, respectively.

This equation assumes the following:

- gas molecules physically adsorb on a solid in layers;
- there is only interaction between adiacent layers of adsorbed gas;
- Langmuir theory can be applied to each layer;
- the interaction between the layers is independent from their position;

By plotting Equation (2.7) as a straight line where $x = P/P_0$ and $y = 1/v[(P_0/P)-1]$ we obtain a linear relationship whit intercept I and slope m that can be used to calculate the molar volume and c:

$$v_m = \frac{1}{m+I} \tag{2.9}$$

$$c = 1 + \frac{m}{I} \tag{2.10}$$

which can be used to calculate the total surface area:

$$A_{total} = \frac{v_m N s}{V} \tag{2.11}$$

where N is the Avogadro number, s the adsorption cross section of the adsorbing species and V the molar volume of the gas that is adsorbed on the sample. The specific surface area of the material is then given by dividing the total surface area A_{total} by the mass of the sample:

$$A = \frac{A}{mass} \tag{2.12}$$

In this work, the instrument used was a Micrometric 3Flex Surface characterization analyzer, coupled with a Flowprep 060 for the sample preparation. The gas used was a N_2/He mix with 30% nitrogen. The samples where degassed prior to analysis at 100 °C overnight.

In Chapter 3, this technique was used to measure the surface area of commercial RP ball milled for 60 h, that was later used to calculate the diffusivity using GITT (Section 2.3.2).

2.2.9 Compression test

Compression testing is a technique used to measure the mechanical properties of a material. The sample is compressed between two plates under an applied load and the compressive stress is measured in function of the displacement. A load-displacement curve is obtained and allows for the measurement of mechanical properties such as the yield stress and the bulk modulus. The results of the experiment can be separated into two segments: loading and unloading. Loading occurs mainly in two stages. First, particles rearrange, then they yield on a particle level, as a consequence of the load. This leads to changes in density. The change in density ρ with pressure P is related to the yield stress, σ_{yield} as shown by Heckel:

[3]

$$\frac{d\rho}{dP} = \frac{(1-\rho)}{3\sigma_{\text{yield}}} \tag{2.13}$$

Further rearrangement and integration of the equation allows for the calculation of the yield stress:

$$\ln(\frac{1}{(1-\rho)}) = \frac{P}{3\sigma_{\text{yield}}} + C \tag{2.14}$$

where C is a constant. The fit of the loading curve (where $\ln(\frac{1}{1-\rho})$ is plotted against P) allows for the calculation of the yield stress.

The linear fit of the unloading curve (plotted as P vs volume V) allows for the calculation of the Bulk modulus (B), according to the equation:

$$B = -V_0 \frac{dP}{dV} \tag{2.15}$$

where V_0 is the volume at zero pressure, which can be found by extrapolation from the linear fit.

This allows for the calculation of the bulk modulus of a sample at a specific density (porous material, not fully dense). Repeated compression tests give different bulk moduli

related to the increasing density of the material (reduced porosity). The measured values can be plotted against P and a linear fit allows to calculate the bulk modulus at zero porosity. The linear fit can be expressed with the following equation:

$$\ln\frac{B}{B_0} = -a\varphi \tag{2.16}$$

that allows the calculation of the bulk modulus (where B_0 is the bulk modulus at zero porosity, φ is the porosity and, a a fitting constant).

In Chapter 3, the bulk modulus of RP was measured using this technique. An Instron test rig with a compression die and punch were used to perform the experiment. Three samples with increasing mass (1 g, 1.5 g and 3 g) were loaded to 500 N, 1 kN and 2kN each, with a full unloading in between each step. This procedure was repeated twice. On the first step, particles in the sample rearrange to achieve full compaction. On the second step, the full compaction of the sample has already been achieved, so the contribution from particles rearranging can be discarded. The density of the sample after the experiment was measured by removing the sample from the die and weighing it. The volume of the compressed sample is calculated from the area of the piston and its position for zero volume. Compression tests were performed with our collaborators Dr. Ed Darnbrough and Jack Aspinall (University of Oxford).

2.2.10 Nanoindentation

Nanoindentation is a technique that allows for the measurement of the mechanical properties of a material, such as elastic modulus (or Young's modulus) and the hardness. In this method, a tip is pressed to the surface of a sample at increasing loads. The penetration of the sample into the material is measured and a load-displacement curve is obtained. The hardness of the material (H) can simply be obtained by dividing the maximum load, P_{max} by the residual indentation area (A_r), which is the area of the tip that penetrated into the sample:[4]

$$H = \frac{P_{max}}{A_r} \tag{2.17}$$

The slope of the load-displacement curve, or stiffness (S) can be used to measure the reduced elastic modulus E_r:

$$E_r = \frac{1}{\beta}\frac{\sqrt{\pi}}{2}\frac{S}{\sqrt{A_p(h_c)}} \tag{2.18}$$

where β is a geometrical constant (generally 1) and $A_p(h_c)$ is the projected area of the indentation at the contact depth h_c. The reduced modulus is a contribution of both the elastic modulus of the sample and the nanoindenter tip:[5]

$$\frac{1}{E_r} = \frac{1-\nu_i^2}{E_i} + \frac{1-\nu^2}{E} \tag{2.19}$$

where E_i and ν_i are the indenter's elastic modulus and Poisson's ratio and E and ν are the sample's elastic modulus and Poisson's ratio. In Chapter 3, nanoindentation is used to measure the elastic modulus of RP and its Poisson's ratio. An Agilent G200 with a 40x optical microscope was used to test individual RP particles on an aluminium stub. In-situ single particle nanoindentation was also performed to measure the fracture toughness K_{1C} of the RP. Individual RP particles were indented using a PI88 Hysitron picoindenter with a MIRA 3 Tescan. This allowed for direct real-time observation of the

nanoindentation of the particles and their fracture caused by the load applied by the indenter. The Griffith criterion can be used to calculate K_{1C}:

$$G = \frac{(K_{1C})^2}{E} \tag{2.20}$$

where G is the energy release rate. This value can be calculated by the energy released from the cracking of the particle (the area under the load-displacement curve, Ω) and the area of fracture S, which is measured from the SEM images after the experiment. G can then be calculated as:

$$G = \frac{d\Omega}{dS} \tag{2.21}$$

which allows for the calculation of K_{1C}:

$$K_{1C} = \sqrt{E\frac{d\Omega}{dS}} \tag{2.22}$$

In this work, in-situ testswere performed in a Mira 3 Tescan with a PI 88 Hysitron picoindenter that allowed for observation of particle cracking and calculation of a fracture toughness, K_{1C}, via fracture area analysis and energy to fracture. Ex-situ tests were performed using a G200 Agilent (KLM) utilising constant stiffness measurements to find an elastic modulus, E, and hardness H.

Nanoindentation experiments were performed with our collaborator Dr. Ed Darnbrough (University of Oxford).

2.3 Electrochemical Characterization

2.3.1 Galvanostatic cycling

In a galvanostatic cycling (GC), a constant current is applied to a cell overtime to study the changes of the potential of the cell and its capacity. This experiment allows to study the performance and the reversibility of the reaction occurring inside the cell. This analysis can be operated via a cutoff voltage control (CVC) where it is performed in a predefined potential range. From the experiment, galvanostatic profile with the potential plotted against the capacity is obtained. The shape of the profile is strictly related to the nature of the reaction of the material that is subject of study. The efficiency of a charge/discharge cycle, referred to as coulombic efficiency, can be be expressed as:

$$\eta_C = \frac{Q_{discharge}}{Q_{charge}} \tag{2.23}$$

Where $Q_{discharge}$ and $Q_{discharge}$ are the capacities showed by the cell in discharge and charge, respectively. The intensity of the current applied to the system is important, as the performance of the material may vary. In literature, this value is often reported as current rate (or C-rate) which is the amount of current that needs to be applied to a material to achieve full charge. This means that a current of 1C will charge the cell in 1 h, while a current of C/10 will charge it in 10 h.

In this work a Bio-logic VMP3 and a BCS were used to perform 3-electrodes cell (EL-cell) and 2-electrodes cell (2032 coin cell) experiments, respectively.

In Chapter 4, GC experiments were performed in coin cell using RP-graphite composite as active material and Na as both the counter and reference electrode. A current of C/15 was applied to test the cycle life of the material and increasing C-rates (up to 1C) were applied to test the rate capability of the composite. The electrolyte used was $NaPF_6$ 1M in a mixture of ethylene carbonate and diethyl carbonate (EC:DEC, 1:1 ratio).

In Chapter 5, the electrochemical tests performed on the composite with K were

performed on a three electrodes EL-cell where two K electrodes were used as the counter and the reference electrode, respectively, and RP-graphite composite was used as active material. A current of C/10 and 1C was used to test the cycle life of the material and increasing C-rates up to 5C were used to test the rate capability of the composite.

In Chapter 6, the GC tests were performed using three electrolites for each alkali ion. The electrolytes used are listed in the following table:

Alkali ion	Li	Na	K
Electrolyte	$LiPF_6$ 1M in EC:DEC	$NaPF_6$ 1M in EC:DEC	KPF_6 0.7M in EC:DEC
	$LiPF_6$ 1M in EC:DEC + FEC 10%	$NaPF_6$ 1M in EC:DEC + FEC 10%	KPF_6 0.7M in EC:DEC + FEC 10%
	LIFSI 1M in EC:DEC	NaFSI 1M in EC:DEC	KFSI 1M in EC:DEC

Table 2.1: Electrolytes used for the electrochemical tests in Chapter 6.

2.3.2 Galvanostatic intermittent titration technique

Galvanostatic intermittent titration technique (GITT) is an electrochemical method that is used to measure the diffusivity of ions in a material. In this technique, current pulses are applied to the cell (positive during charge and negative during discharge) and are followed by a relaxation time where no current is applied. The changes in potential with time are measured throughout the experiment. When a current is applied (for example during the charging step) a quick jump in potential can be observed. This is proportional to the iR drop, where i is the current R is the sum of the charge transfer resistance and the uncompensated resistance. Then the potential slowly increases, due to the galvanostatic pulse. When the pulse stops, the relaxation time starts and a drop in potential proportional to the iR drop can be observed. Then the potential slowly reaches a steady state, when the concentration in the electrode becomes homogeneous due to the ion diffusion. The behaviour is the opposite when a negative current is applied. These current pulses are applied several times until the material is fully charged or discharged.

The diffusion coefficient of the ion can be calculated at each step the following equation:[6, 7]

$$\mathrm{D} = \frac{4}{\pi}\left(\frac{\mathrm{i}\Omega_\mathrm{M}}{\mathrm{Z_A FS}}\right)^2\left[\frac{(\mathrm{dV_{ss}/d\delta})}{(\mathrm{dV_{ca}/d\sqrt{t}})}\right]^2\left(\tau \ll \frac{\mathrm{L}^2}{\mathrm{D}}\right) \tag{2.24}$$

where i is the current applied, Ω_M is the molar volume of the electrode material at each step ($\mathrm{cm^3\ mol^{-1}}$), Z_A is the charge number, F is the Faraday constant (96485 $\mathrm{C\ mol^{-1}}$), S is the electrode/electrolyte contact area ($\mathrm{cm^2}$), $\mathrm{dV_{ss}/d\delta}$ is the difference between two subsequent steady state potential at the end of the relaxation steps ($\mathrm{V_{ss}}$), $\mathrm{dV_{ca}/d\sqrt{t}}$ is the slope of the plot of the potential while the current is applied, linearized by plotting ($\mathrm{V_{ca}}$) versus $\sqrt{\mathrm{t}}$. This equation can be applied when τ (the time duration of the current pulse) is greatly smaller than the characteristic length of the electrode (L).

The use of GITT requires the electron transfer to be comparable to the alkali-ion transport in the system, so that the change can equilibrate at any instant.[8] Unfortu-

nately, RP suffers from a very low electronic conductivity, which makes it necessary to use a RP-graphite composite in order to increase the electronic conductivity and satisfy this requirement. Therefore, the use of GITT required some assumptions to be made. Firstly, we assume that RP is the only active material reacting with the alkali ions in the electrode. Therefore, the current is flowing only to RP and the electrode/electrolyte contact area is the surface area of RP. This way, the contact area can be calculated from the surface area of the ball milled RP measured with BET ($22.9\,m^2\,g^{-1}$) multiplied by the mass of RP on the electrode used in the experiment. Secondly, we assume that the diffusivity of Li and K in graphite is orders of magnitude faster than in RP. The reported values of diffusivity for Li and K are $\approx 10^{-9}\,cm^2\,s^{-1}$ and $\approx 10^{-8}\,cm^2\,s^{-1}$, respectively.[9, 10] In the case of Na, the alkali metal does not intercalate in graphite, as discussed earlier. [11] From this assumption we define that the values we obtain from the experiment are mainly related to the diffusivity of the ions in RP.

The GITT measures shown in Chapter 3 have been performed on the RP-graphite composite (the preparation of the composite and the electrode is explained in Section 2.1.1). A coin cell was used and Li, Na or K metal was used as both the counter and the reference electrode for each measure involving a different alkali ion. The electrolytes used in these measurements are listed in the following table:

Alkali ion	Li	Na	K
Electrolyte	$LiPF_6$ 1M in EC:DEC	$NaPF_6$ 1M in EC:DEC + FEC 10%	KFSI 1M in EC:DEC

Table 2.2: Electrolytes used for the GITT analysis in Chapter 3.

A current pulse was applied to the active material for 30 minutes, followed by a relaxation time of two hours, to allow the system to equilibrate. The current used for the experiment corresponds to a C-rate of C/20, based on the theoretical capacity of RP with each individual alkali metal. The electrodes were all discharged to 0.01 V vs Li^+/Li, Na^+/Na or K^+/K (depending on the metal used) to allow the formation of the SEI, then

charged to 2.5 V vs Li^+/Li, Na^+/Na or K^+/K. The GITT was performed during the dealloying reaction.

2.3.3 Potentiostatic Electrochemical Impedance Spectroscopy

Potentiostatic Electrochemical Impedance Spectroscopy (PEIS) is a technique that is commonly used to measure the internal resistance of a sample, which is defined by the Ohm's law as the ratio between the voltage E and the current I:

$$R = \frac{E}{I} \tag{2.25}$$

In this technique, an AC potential is applied to a cell and the changes in current are measured. Assuming a sinusoidal potential, the potential changes based on the equation"

$$E_t = E_0 \sin(\omega t) \tag{2.26}$$

where E_t is the potential at the time t, E_0 is the amplitude of the signal and ω is the angular frequency, defined as:

$$\omega = 2\pi f \tag{2.27}$$

where f is the frequency expressed in Hz. The changes in current can be also expressed by a sinusoidal change:

$$I_t = I_0 \sin(\omega t + \varphi) \tag{2.28}$$

where I_t is the current at the time t, I_0 is the amplitude of the current and φ is phase that describes the shift of the current in respect to the potential.

The impedance of the system is then calculated as:

$$Z(\omega) = \frac{E_t}{I_t} \tag{2.29}$$

The impedance analysis shown in Chapter 5 was performed on a three electrode cell (EL-Cell) using K as both the counter and the reference electrode and the RP-graphite

composite as the active material. The electrode was prepared following the procedure described in Section 2.1.3. The range of frequencies used in the experiment was 200 kHz - 1Hz. The impedance was performed after each discharge/charge cycle, allowing 1 h of relaxation time prior to the measure, in order to allow the system to equilibrate.

2.4 References

1. Chang, W.-C. *et al.* Solution Synthesis of Iodine-Doped Red Phosphorus Nanoparticles for Lithium-Ion Battery Anodes. *Nano Letters* **17,** 1240–1247 (2017).
2. Nitta, N. *et al.* Influence of Binders, Carbons, and Solvents on the Stability of Phosphorus Anodes for Li-ion Batteries. *ACS Applied Materials & Interfaces* **8,** 25991–26001 (2016).
3. Heckel, R. W. Density-Pressure Relationships in Powder Compaction (1961).
4. Anthony C Fischer-Cripps. *Nanoindentation* (Springer, New York, 2011).
5. MA, D. Determination of Young's modulus by nanoindentation. *Science in China Series E* **47,** 398 (2004).
6. Wen, C. J. Thermodynamic and Mass Transport Properties of "LiAl". *Journal of The Electrochemical Society* **126,** 2258 (1979).
7. Zhu, Y. *et al.* Galvanostatic Intermittent Titration Technique for Phase-Transformation Electrodes. *The Journal of Physical Chemistry C* **114,** 2830–2841 (2010).
8. Wang, R. *et al.* Influence of Conductive additives on the stability of red phosphorus-carbon anodes for sodium-ion batteries. *Scientific Reports* **9,** 1–6 (2019).
9. Wang, S. *et al.* Interfacial Chemistry in Solid-State Batteries: Formation of Interphase and Its Consequences. *Journal of the American Chemical Society* **140,** 250–257 (2018).

10. Levi, M. D. *et al.* Diffusion coefficients of lithium ions during intercalation into graphite derived from the simultaneous measurements and modeling of electrochemical impedance and potentiostatic intermittent titration characteristics of thin graphite electrodes. *Journal of Physical Chemistry B* **101,** 4641–4647 (1997).

11. Moriwake, H. *et al.* Why is sodium-intercalated graphite unstable? *RSC Advances* **7,** 36550–36554 (2017).

Chapter 3

Electrochemo-mechanical properties of RP

3.1 Introduction

This chapter concerns about the study of the volume expansion of RP upon alloying with Li, Na and K and the generation and evolution of stresses on the particle during the reaction and the possibility for the particle to fracture due to those stresses.

Over the course of this chapter, a computational model is developed to investigate the stresses in a RP particle during the reaction and the possibility that these could cause the fracture of the particle. However, the use of the model requires that mechanical and electrochemical properties of RP are known. Because most of these parameters are not yet available in literature, this work is also focused on the measurement for the first time of the elastic and plastic properties and the diffusivity of alkali ions in RP. The mechanical behaviour of single RP particles upon alloying is then evaluated.

3.2 Electrochemo-mechanics

The alloying/de-alloying reaction between alkali metals and RP leads to a huge volumetric expansion/contraction that leads to stress generation at the particle level, which could result in the failure of the material and short cycle life. The amount of stresses in the particle are related to the intrinsic mechanical properties of RP, such as the elastic modulus (or Young's modulus, E) and the Poisson's ratio (ν), as well as the diffusivity of the alkali ions in the particle (D), the partial molar volume of the alkali ions in the particle (Ω), the current density (i), and ultimately the shape and size of the particle. The calculation of the amount of stresses generated in a particle and their relation to the size of the particle can be useful to understand the relation between particle size and the mechanical stability of RP particles during cycling.

A model developed by Zhao et al. has already been developed to tackle a similar problem regarding Si.[1] In their model, a number of assumptions are made:

- The electronic conductivity of the material is orders of magnitude higher than the ionic conductivity. This ensures that the electrons can equilibrate at any time and so their influence can be discarded. This condition is satisfied, as the reported electronic conductivity of RP is about $10^{-}14 Scm^{-}1$, while the average ionic conductivity is about 100 times slower;

- The diffusion of ions in the material is described using a dilute solution model. This way, ions diffuse through interstitial sites and vacancies are not taken into account. The assumption is satisfied as an amorphous material is considered;

- The structure of the host material is slightly affected and can fully recover. Also, material properties remain constant during alloying and de-alloying. Although, the mechanical properties of the resulting material are expected to change, this assumption is correct until the mechanical properties (i.e. young's modulus) stay in the range of 10^2;

- The host material is amorphous. This leads to the assumption that the mechanical and chemical properties as homogeneous and isotropic. This is exactly the case of RP;

- The particle is considered as free standing and there is no interaction with other neighbor particles. In this case, we want to consider only the effect on one single particle, as the interaction between particles (RP-RP and RP-C particles) would be computationally expensive. The performance of the entire electrode will be investigated in chapter 4.

With these assumptions, equations that describe the stress and strain developed during the reaction can be analytically calculated. The total strain in a particle is a combination of the elastic strain (ε^{e}_{ij}) and the chemically induced expansion (ε^{c}_{ij}):

$$\varepsilon_{ij} = \varepsilon^{e}_{ij} + \varepsilon^{c}_{ij} \tag{3.1}$$

The total strain can also be expressed as:

$$\varepsilon_{ij} = \frac{1}{2}\left(u_{i,j} + u_{j,i}\right) \tag{3.2}$$

where u_i is the displacement of the particle.

The chemical strain ε^{c}_{ij} directly depends on the partial molar volume of the ions in the particle, and can be expressed as

$$\varepsilon^{c}_{ij} = \frac{1}{3}\Omega\delta_{ij} \tag{3.3}$$

Where δ_{ij} is a Kronecker delta. Considering a linear relationship between the volume change and the concentration of the alkali metal x (Meaning that the partial molar volume of the alkali metal A is constant in A_xP), and also considering a spherical particle with radius R_0 and an homogeneous current across the surface, the hydrostatic stress can be calculated. The two main types of stresses that are defined are the radial stress σ_r (the

stress towards or away the centre point of the object) and the hoop stress (the stress perpendicular to the radius of the object). These stresses can be calculated using the following equations:

$$\sigma_r = \frac{\Omega E i R_0}{3(1-\nu)FD}\left[-\frac{1}{5}\left(\frac{r}{R_0}\right)^2 + \frac{1}{5} + \frac{4R_0^3}{r^3}\sum_{n=1}^{\infty}\frac{-\lambda_n r\cos(\lambda_n r)+\sin(\lambda_n r)}{\lambda_n^4 R_0^4 \sin(\lambda_n R_0)}\exp(-D\lambda_n^2 t)\right] \tag{3.4}$$

$$\sigma_t = \frac{\Omega E i R_0}{3(1-\nu)FD}\left\{-\frac{2}{5}\left(\frac{r}{R_0}\right)^2 + \frac{1}{5} + \right.$$

$$\left. +2\sum_{n=1}^{\infty}\left[\frac{R_0}{r}\frac{\sin(\lambda_n r)}{\lambda_n^2 R_0^2 \sin(\lambda_n R_0)} - \frac{R_0^3}{r^3}\frac{-\lambda_n r\cos(\lambda_n r)+\sin(\lambda_n r)}{\lambda_n^4 R_0^4 \sin(\lambda_n R_0)}\right]\exp(-D\lambda_n^2 t)\right\}. \tag{3.5}$$

Where it can be seen that both stresses are proportional to the same material properties:

$$\sigma_r, \sigma_t \propto \frac{\Omega E}{1-\nu}\frac{iR_0}{D} \tag{3.6}$$

A mode I crack (formed when the tensile stress is perpendicular to the plane of the crack) is predicted to form on the particle when these stresses are higher than the critical stress (σ_{1C}) of the material. The critical stress can be calculated from the fracture toughness (K_{1C}), the flaw size (r, which acts as stress concentrator) and the crack geometry factor of order one (Ψ):

$$\sigma_{1C} = \frac{K_{1C}}{\Psi\sqrt{2\pi r}} \tag{3.7}$$

Therefore, in order to apply this model to calculate the strain occurring during the alloying reaction of RP particles, values such as D, E and ν are needed. Unfortunately, these values are still missing in the literature and the measurement of these values is crucial to the use of the model. For this reason, this work is primarily focused on the measurement of these properties, which will also act as a reference for the field, adding

to the previously reported bulk moduli values.[2, 3] Afterwards, these values will be implemented into the model to understand the stress generation and propagation in the RP particle. This model was developed in collaboration with Dr. Ying Zhao (Tongji University, Shanghai, China).

3.3 Results and discussion

3.3.1 Electrochemical properties

The measurement of the diffusivities of Li^+, Na^+ and K^+ in RP was operated using GITT analysis (details of this procedure are reported in Section 2.3.2).[4] The GITT profiles are shown in Figure 3.1(a-c) and the results are listed in Appendix A. The GITT analysis was performed during the charging step (de-alloying) to avoid further contribution from the formation of the SEI during the first discharge. The complete alloying of RP with Li, Na and K during the first discharge (thus forming the phases Li_3P, Na_3P and KP) is assumed due to the low current used in the procedure.

At the beginning of the GITT analysis (Figure 3.1d), the observed diffusivity of the lithiated RP particles (corresponding to the Li_3P phase) is about $2 \times 10^{-16}\,cm^2\,s^{-1}$ and increases rapidly to about $1 \times 10^{-15}\,cm^2\,s^{-1}$ as Li+ ions are extracted (increasing state of charge, s.o.c.). When this value is reached, a constant drop in diffusivity is observed as the dealloying reaction progresses, reaching a minimum of $1 \times 10^{-16}\,cm^2\,s^{-1}$. This decrease could be explained by the formation of intermediate phases such as LiP_7 and Li_3P_7, as described by Mayo et al.[5] However, the formation of such phases has never been experimentally observed and the galvanostatic profile does not show plateaus in this region (Figure 3.1e). Finally, when RP is almost charged, the diffusivity increases up to $1 \times 10^{-15}\,cm^2\,s^{-1}$.

When Na de-alloying with RP is considered, however, it is immediately clear that the capacity obtained from RP is lower than the one obtained with Li (Figure 3.1a,b). The reason is still not clear, although it could be related to the non-reactivity of graphite

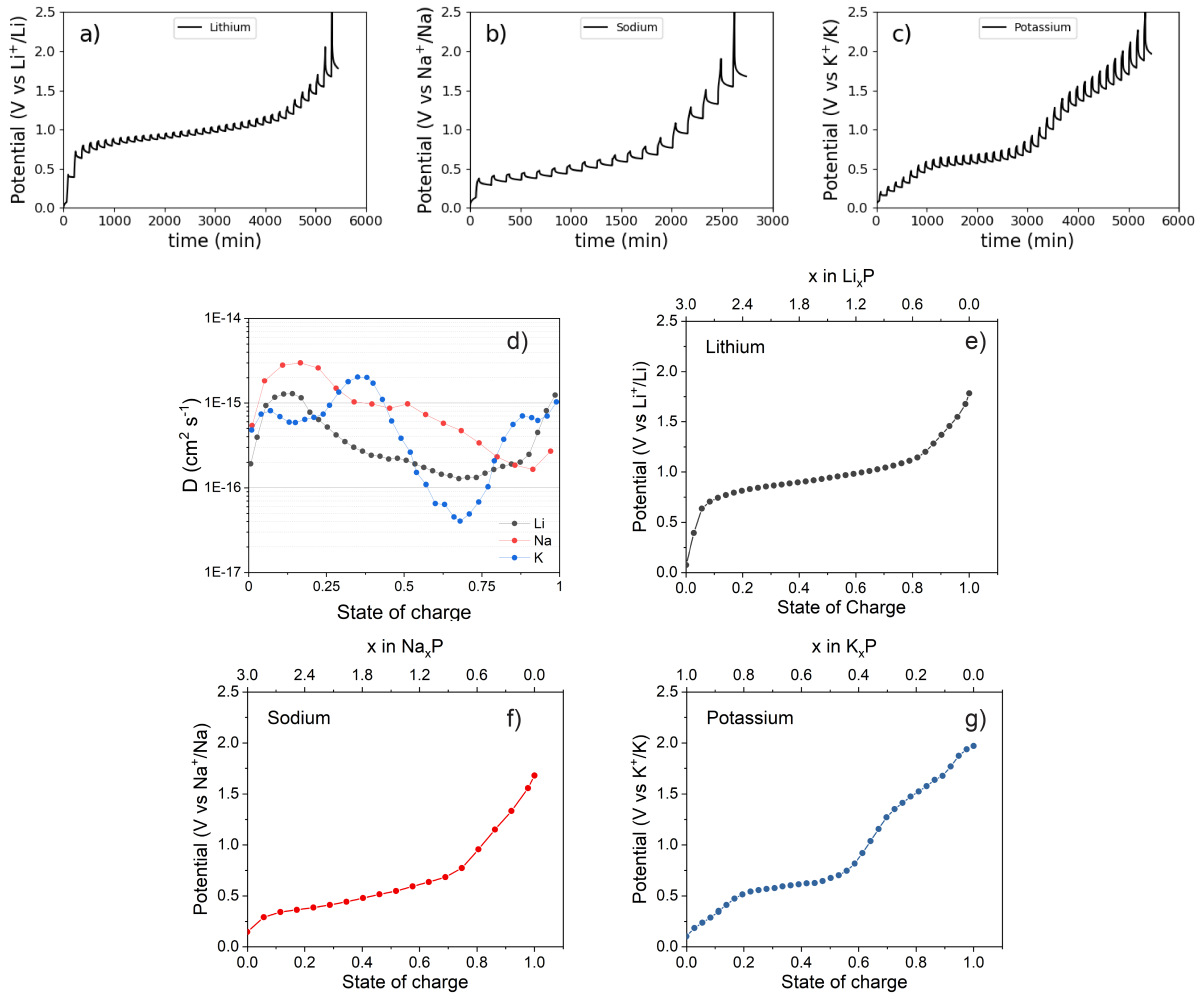


Figure 3.1: a-c) GITT profiles of Li, Na and K, respectively. d) Diffusivity values for lithium, sodium and potassium in RP, calculated using the GITT profiles shown in (a-c), and Equation (2.24). The state of charge is defined as follows: 0 = lithiated, sodiated and potassiated RP; 1 = RP. These values are listed in Appendix A. Charging profiles of (e) Li, (f) Na and (g) K made using steady state potentials taken from the GITT profiles in Figure 3.1a-c.

with Na (which instead react with Li and could contribute to a higher capacity) or to the presence of RP particles that are inactive with Na. For this reason, the GITT analysis has been performed with the assumption that the active RP particles have undergone full sodiation and de-sodiation process. The diffusivity of Na^+ in RP shows a similar trend to that of Li^+. This could be a hint that the two reactions follow a similar pathway (Figure 3.1d). Overall, the diffusivity is higher than Li^+. This could be related to the larger volume expansion upon sodiation (Section 2.3.2). At the beginning, during

the early desodiation steps (from the presumed phase Na_3P), the diffusivity is about $5 \times 10^{-16}\,cm^2\,s^{-1}$ and increases rapidly to a maximum of $3 \times 10^{-15}\,cm^2\,s^{-1}$ when Na^+ ions are removed. Further de-alloying of RP results in a decrease of the diffusivity to a low of $2 \times 10^{-16}\,cm^2\,s^{-1}$. In this region, the formation of Na-poor phases has been described by Mayo et al., however, Marbella et al. suggested that the sodiation and de-sodiation of RP may follow different pathways.[6] In particular, Sottmann et al. described how the sodiation mechanism could follow the reaction path RP $\rightarrow$ NaP $\rightarrow$ Na_3P while the de-sodiation reaction follows the path $Na_3P \rightarrow Na_{2.6}P \rightarrow Na_{2.36}P \rightarrow$ RP.[7] If the assumption of full sodiation of RP particles in this experiment is correct, this could explain the increase in diffusivity observed up to a s.o.c. of about 0.2 (corresponding to the formation of the phase $Na_{2.36}P$) and the linear decrease in diffusivity observed with further dealloying. The final increase in diffusivity is likely related to the formation of the final phase RP.

On the other hand, K shows a completely different trend to Li and Na (Figure 3.1d). We hypotesise that the behaviour is related to a different reaction mechanism. The diffusivity in the fully potassiated RP is observed to be about $5 \times 10^{-16}\,cm^2\,s^{-1}$. However, the de-alloying reaction induces a sharp change in diffusivity that reach a maximum of $2 \times 10^{-15}\,cm^2\,s^{-1}$ when the s.o.c. is about 0.35 and a minimum of $4 \times 10^{-17}\,cm^2\,s^{-1}$ when the s.o.c. is about 0.68. The galvanostatic profile shows the presence of three different plateaus (Figure 3.1g), a large one at about 0.5 V vs K^+/K, a smaller one at about 1.25 V vs K^+/K and a tiny one at about 2 V vs K^+/K. If the dealloying reaction path is similar to the alloying reaction, the result is consistent with the predictions by Yang et al. In fact, they suggested that intermediate phases should form before the formation of the final phase, KP.[8] Both RP and BP show a similar galvanostatic profile, suggesting that their reaction path is also similar.[9, 10] The concentration of K seen where the sharp changes in diffusivity are observed are close to the phases predicted by Yang et al. ($K_{0.27}P$, $K_{0.66}P$ and KP). This suggests that the changes in diffusivity could be a result of the complete formation of these phases during the reaction. However, more in-depth

study is required to better understanding the reaction path of RP with the alkali ions and further confirm if such intermediate phases are formed.

Due to the large computational cost that would be required to run a simulation that takes into account the change in diffusivity with the concentration of the ions and due to the number of assumptions made to perform the experiment, we decided to consider an average value for the three ions: $5 \times 10^{-16}\,\mathrm{cm^2\,s^{-1}}$. This is expected to underestimate or overestimate the stresses that will be calculated on the model by a factor of 10, if the highest and the lowest diffusivity values are taken in consideration ($1\text{x}10^{-15}$ and $1 \times 10^{-17}\,\mathrm{cm^2\,s^{-1}}$).

3.3.2 Mechanical properties

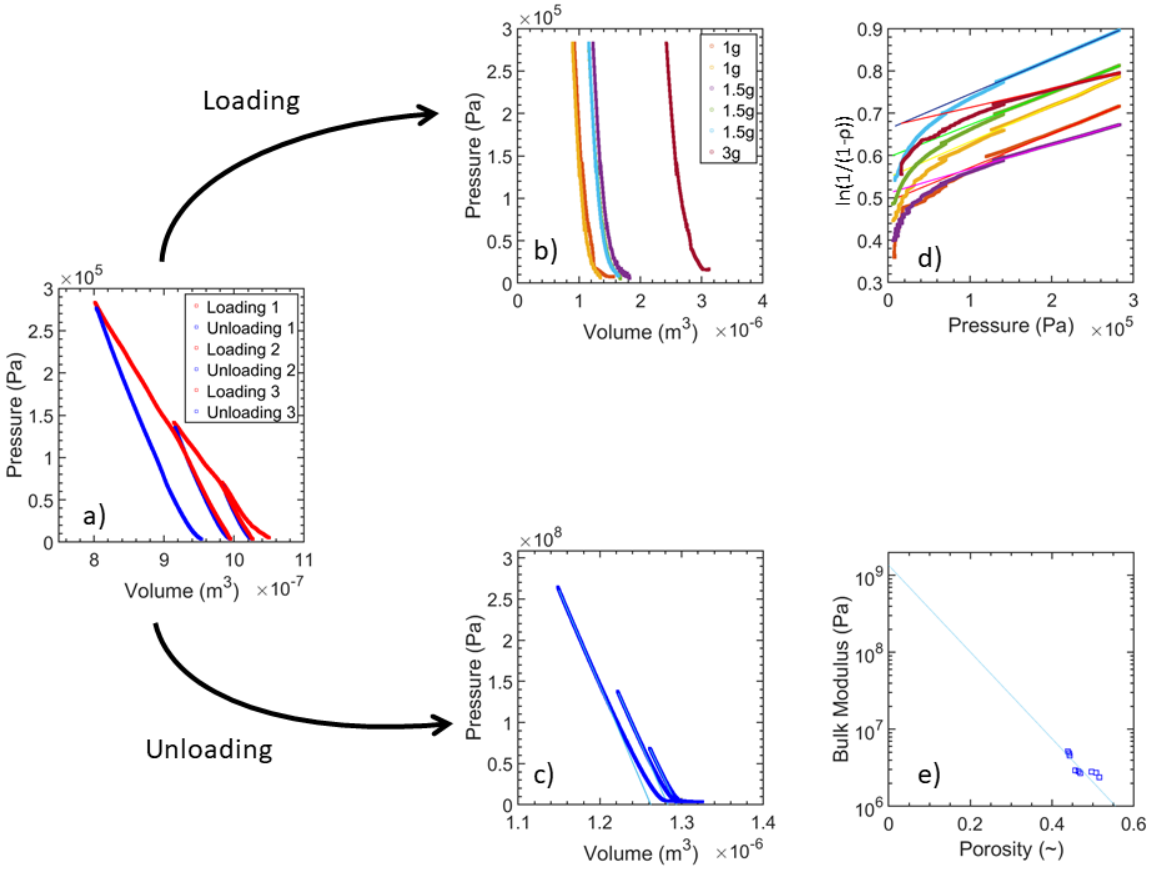


Figure 3.2: a) Example load/unload test, b) loading curves used to find the yield stress of powder, c) unloading curves fitted for bulk modulus, d) density fitted vs pressure applied and e) Bulk modulus vs volume fraction fitted with Equation (2.16).

To understand the influence that deformation has on the cyclability of RP, it is paramount that both the reversible change (related to mechanical properties such as elastic modulus, E, and Poisson's ratio, ν) and the irreversible change (e.g. fracture toughness, K_{1C}, and yield stress, σ_{yield}) are investigated.

To study the elastic and plastic response of RP, powder compression tests were conducted on commercial RP. Details of this technique are provided in Section 2.2.9. Unfortunately, no fully dense RP sample is available, so this approach has been applied to powders with a range of densities. The results of the compression tests are shown in Figure 3.2. Samples of commercial RP powder were loaded/unloaded sequentially three times to 500 N, 1kN and 2kN. Figure 3.2a shows an example of a repeated loading/unloading experiment performed on one sample. The loading and unloading curves were then extracted and processed to acquire the information needed.

The loading curves shown in Figure 3.2b, are characteristic of powder with different masses being compressed by an increasing pressure P, where at low P the reorientation of particles and their compaction occurs, while at high P the particles start to yield locally. This last region is mostly linear and can be easily fitted. The density of the samples was then calculated (as explained in Section 2.2.9) and plotted against the pressure applied (Figure 3.2d). The linear region was fitted and, after multiple measurements, the yield stress of RP was calculated using the equation [11]:

$$\ln\left(\frac{1}{(1-\rho)}\right) = \frac{P}{3\sigma_{yield}} \tag{3.8}$$

Which resulted in an average yield stress (σ_{yield}) of 500 $\pm$ 130 MPa. Compared to amorphous Si, this value is significantly lower ($\approx$ 1/20th). This value is important when the failure of a material is considered at the particle level. The yield or plastic deformation of the particle results in an irreversible change which is preferable to fracture when electrical contact between particles and coulombic efficiency are considered.

Moreover, unloading curves from samples that have a range of masses (1, 1.5 and 3

g, see Section 2.2.9) were analyzed, as shown in Figure 3.2c. These curves allowed for the measurement of the bulk modulus at the density achieved by the material during the compression test. In order to calculate the bulk modulus of the fully dense RP, the bulk modulus measured at different porosities of the RP sample tested were plotted (Figure 3.2e) and, by solving Equation (2.16), the bulk modulus of the fully dense material was calculated as $B_0 = 1.9 \pm 0.1$ GPa.[12] Compared to previously reported values for this property, this one is slightly lower.[2, 3] However, this was the first time that this parameter has been measured using a mechanical test rather than x-ray diffraction or digital imaging.

The elastic properties of RP were measured via ex-situ nanoindentation using constant stiffness measurements (Figure 3.3). Details are shown in Section 2.2.10. Nanoindentation experiments can provide the hardness (H), which is related to the yield stress as:

$$H \approx 3\sigma_{yield} \tag{3.9}$$

and the reduced elastic modulus, E_r, which is a combination between the mechanical properties of the sample (E and ν) and the indenter (E_i and ν_i), Equation (2.19). Using the known properties of the nanoindenter and the reduced elastic modulus obtained by the experiment, the properties of RP can be calculated, by rearrangement of Equation (2.19) and Equation (3.10):

$$B = \frac{E}{3(1-2\nu)} \tag{3.10}$$

$$\frac{1}{E_r} = \frac{1-\nu_i^2}{E_i} + \frac{1-\nu^2}{B(3(1-2\nu))} \tag{3.11}$$

from which ν can be calculated and then E can be obtained using the previous equations. Using the mechanical properties measured, other properties such as shear modulus can be calculated:

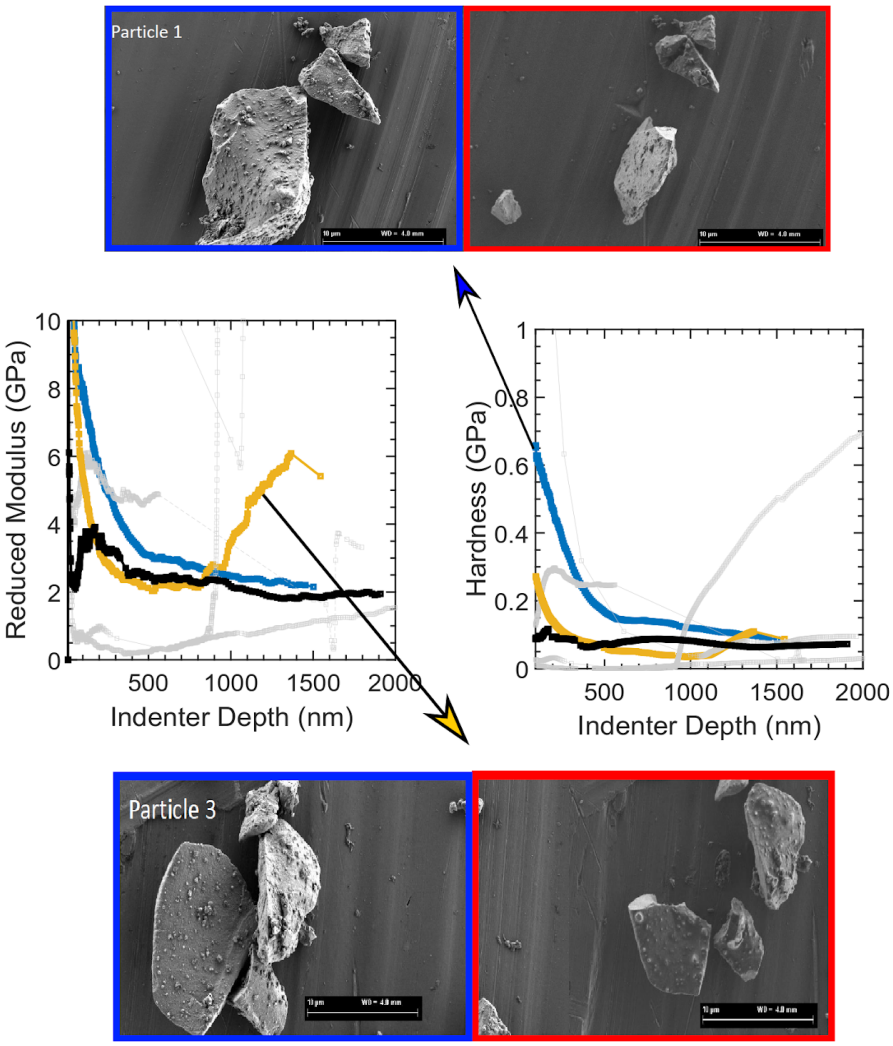


Figure 3.3: Single particle nanoindentation grey results discounted. Blue test particle shown before (SEM image with blue border and after (SEM image with red border) above and yellow particle below. The average of yellow, blue and black over the range 400-800nm depth gives values of: $E_r = 2.5 \pm 0.4$ GPa and H= 100 ± 50 MPa. Nanoindentation experiments were performed with our collaborator Dr. Ed Darnbrough (University of Oxford).

$$\mu = \frac{3B(1-2\nu)}{2(1+\nu)} \tag{3.12}$$

The fracture toughness of RP was measured by in-situ SEM nanoindentation of single RP particles. This allowed for direct observation of the formation of cracks on the particles and the analysis of the fracture surface area, S, measured from the images. The measure

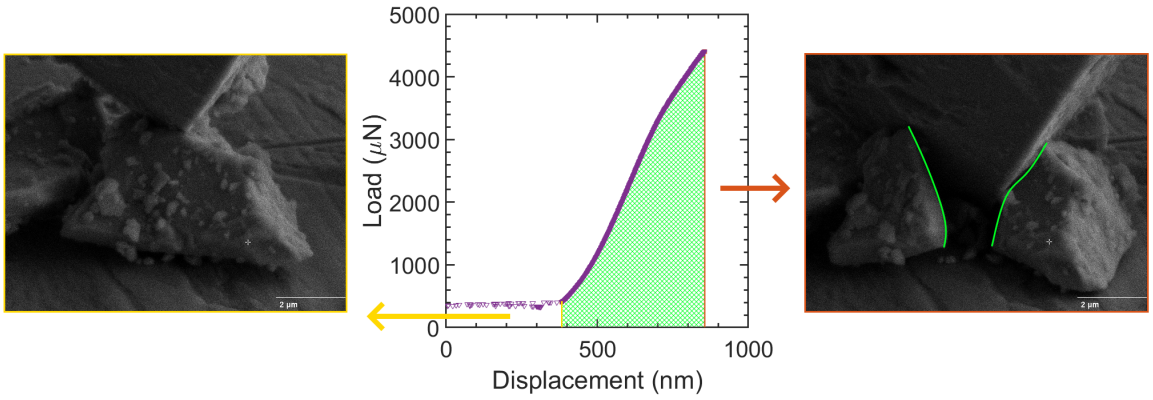


Figure 3.4: Start-to-fracture energy and SEM images from in-situ test showing the surface before the fracture (left) and after the fracture (right). In/situ nanoindentation experiments were performed with our collaborator Dr. Ed Darnbrough (University of Oxford).

of the energy required to cause the fracture (corresponding to the area under the curve in Figure 3.4c), F, and the fracture surface area, allows for the calculation of the fracture toughness [13]:

$$K_{1C} = \sqrt{E\frac{dF}{dS}} \tag{3.13}$$

All the mechanical properties that have been measured and calculated are shown in Table 3.1 and compared to the properties of amorphous Si that have been reported in literature.

Elastic Property	B	Er	E	ν
Method	powder compression	ex-situ indent	calculated	calculated
RP	1.9±0.1 GPa	2.5±0.4 GPa	2.3±0.4 GPa	0.296±0.079
Amorphous Si	n.a.	n.a.	136±9 GPa	0.27±0.02
Plastic Property	σ_{yield}	H	$3H \approx \sigma_{yield}$	K_{1C}
Method	powder compression	ex-situ indent	calculated	in-situ indent
RP	500±130 MPa	100±50 MPa	290±50 MPa	0.3±0.1 MPa $m^{0.5}$
Amorphous Si	9.2±0.2GPa	10.9±0.9 GPa	33±3 GPa	4.7 MPa $m^{0.5}$± 8%

Table 3.1: Elastic and Plastic properties of RP as measured and calculated by this work and values for amorphous Si from references for comparison.[14–17]

Overall, the plastic properties of RP allow for its classification as ceramic, like Si (chart 7 in [18]).

When elastic properties are also considered, however, it is clear that RP can withstand higher strains without failure compared to Si. This is mainly related to RP having a smaller elastic modulus ($\approx$ 1/60th of Si). The presence of flaws on or within the particle can also cause the particle to fracture rather than yield. This possibility is related to the size of these flaws. The critical flaw size (minimum size of the flaw that could cause the fracture of the particle) was also calculated, and resulted to be $160\pm^{332}_{28}$ nm for RP and 6$\pm$1 nm for amorphous Si. This means that the presence of a flaw that is $160\pm^{332}_{28}$ nm would cause the fracture of a RP particle, while a 6$\pm$1 nm flaw is needed in the Si case. However, As shown by McDowell et al. with their in-situ TEM experiment, the lithiation of spherical amorphous Si did not provoke the fracture of particles as big as 860 nm, even though a flaw as low as 6 nm was needed to initiate the fracture process.[19] Flaws that are 160 nm in size are rarely present on RP particles, makes their fracture even more unlikely, compared to Si. These can also be related to a possible particle size that is likely to fracture using the model developed. The result is that both Si and RP are likely to retain the connection throughout the particle, even in the case of yielding, which is preferable when cycling. The stresses needed to cause the yield of the RP will be calculated using the model.

3.3.3 Electrochemo-mechanical model

Knowing the mechanical and electrochemical properties of RP, the model was developed. This allowed the stresses generated in the RP particle to be simulated during the alloying reaction.

Several assumptions have been made in order to develop this model, as described previously. With those assumptions, analytical solutions can be obtained. It should be noted that the stress levels for the alkali ions (K in particular) may be underestimated, especially if the changes in the diffusion coefficient are taken into account (as shown in Figure 3.1). In fact, the alloying reaction with K may result in a phase separation, leading to a high stress concentration at the interphases.

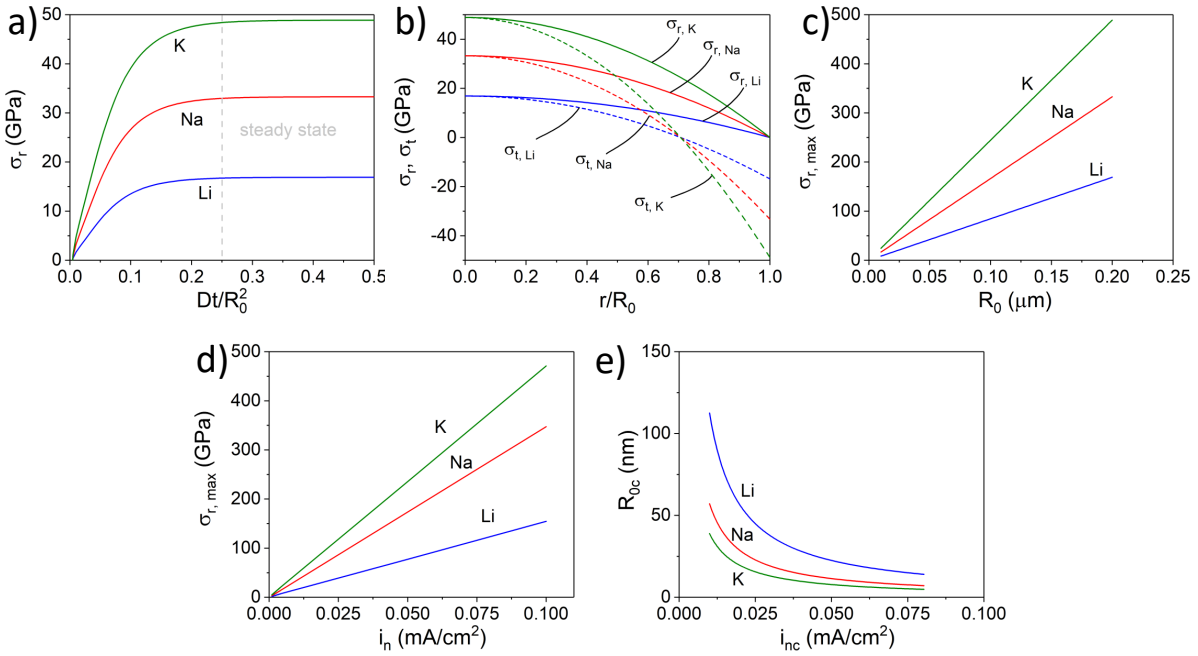


Figure 3.5: a) Evolution of radial stress with time normalised by Dt/R_0, where D is the diffusion rate and R_0 is the particle size. b) Distribution of radial and tangential stress (solid and dashed line, respectively) within a sphere at steady state. Maximal radial stress with changing particle size (c) and pore-wall current density (d). e) Critical particle radius of RP when alloying with Li, Na and K when different pore-wall currents are applied. This model was deveoloped in collaboration with Dr. Ying Zhao (Tongji University, Shanghai, China)

In the simulation a spherical RP particle was considered (with radius of 100 nm) and a Young's modulus of 2.3 GPa. The current density that was applied on the surface of the particle is given by the pore-wall current density, i_n, which can be approximated from[20]:

$$i_n = \frac{iR_0}{3\varepsilon\delta_{electrode}} \tag{3.14}$$

which is related to an electrode consisting of identical spherical particles with the same radius R_0. ε is the volume fraction of RP in the electrode, while $\delta_{electrode}$ is the thickness of the electrode. Considering an electrode with thickness 15 μm and a volume fraction of RP of 0.4, a current density of 10 mA cm^{-2} is equal to a pore-wall current density of 0.05 mA cm^{-2}, calculated from Equation (3.14). More parameters used in this simulation are shown in Appendix C.

In Figure 3.5a, the radial stress increases at the centre of the particle while the ions

insert. Then it reaches a steady state. Among all the ions, K induces the highest stresses, while Li induces the lowest. The steady state is reached when $Dt/R_0^2 > 0.25$. Radial and tangential stresses (shown in Figure 3.5b) change differently during the alloying reaction. Again, the largest change in amount of stress is given by potassiation, while the stress distribution induced by lithiation is more homogeneous

It is important to note that radial stresses are always in tension in the particle until they reach zero at the surface of the particle. On the other hand, the tangential (hoop) stresses vary from being tensile stress (at the centre of the particle) to compressive (at the surface). In the latter case, compressive stress can lead to plastic failure (if they are higher than σ_{yield}) and the tensile stress can cause cracks or plastic failure, depending on which failure stress (σ_{1c} vs σ_{yield}) is lower. As mentioned earlier, the effect of phase transformation were not taken into account and diffusivity and mechanical properties are kept constant. In particular the same average value of diffusivity was used for all three ions. However, as shown earlier (Figure 3.1), Li and Na show a similar trend but K is more variable, ranging from 10^{-17} to $10^{-15}\,cm^2\,s^{-1}$ (when $0.25 < x < 0.6$ in K_xP). For this metal, we expect that the concentration gradient in the particle could lead to higher stresses that were not taken into account in this model.

In Figure 3.5c it is shown how the particle size and the current density affect the maximal radial stresses. As expected from Equation (3.6), the relation between these properties and the stresses is linear, with the gradient changing based on the ions that is reacting with RP. It is interesting to note that the stresses caused by K are the same caused by Li with a current density ≈ 3 times higher. This means that RP can withstand the alloying with Li better than Na or K, without resulting in the failure of the particle ($\sigma > \sigma_{yield}$).

In Figure 3.5e, the relation between the particle radius and the pore-wall current that led to the critical stress is shown. The plot shows that the increase of one of the two parameters requires the decrease of the other one, in order to avoid that stresses reach the limit line for failure, causing the particle to yield or fracture. Again, Li shows that

lower stresses are developed with this metal an that the critical failure stress is caused with bigger particles, compared to Na or K, with the same pore-wall current. The trend remains unchanged with increasing currents.

The validity of this model has been tested with in-situ TEM experiments where particles were charged using extreme currents. Spherical and ball milled commercial RP particles were produced using the procedures described in Section 2.1.1 and Section 2.1.2 and tested.

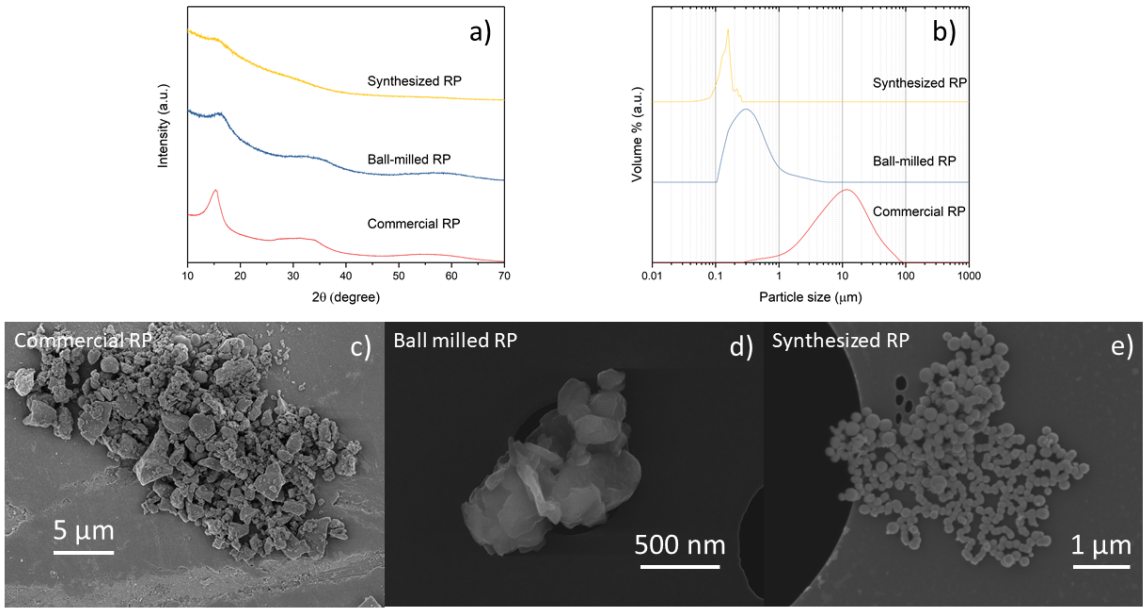


Figure 3.6: a) XRD data of the three RP samples used: commercial RP (red), ball milled commercial RP (blue) and synthesized RP (yellow), showing the characteristic amorphous profile with no visible crystalline impurities. b) Particle size distribution of commercial RP, ball milled commercial RP and synthesized RP. SEM images of the commercial RP (c), ball milled commercial RP (d) and synthesized RP (e).

Synthesized and ball milled commercial RP do not show the presence of any crystalline peak on the XRD, due to the amorphous nature of the material (a). As shown in b, the synthesized spherical RP particles have a sharp particle-size distribution centered at about 150 nm, while the ball milled commercial RP has a distribution centered at about 300 nm. The morphology of ball milled commercial RP is rough and irregular, similar to the pristine commercial RP. On the other hand, synthesized spherical RP particles have

a near-perfect spherical shape (c-e).

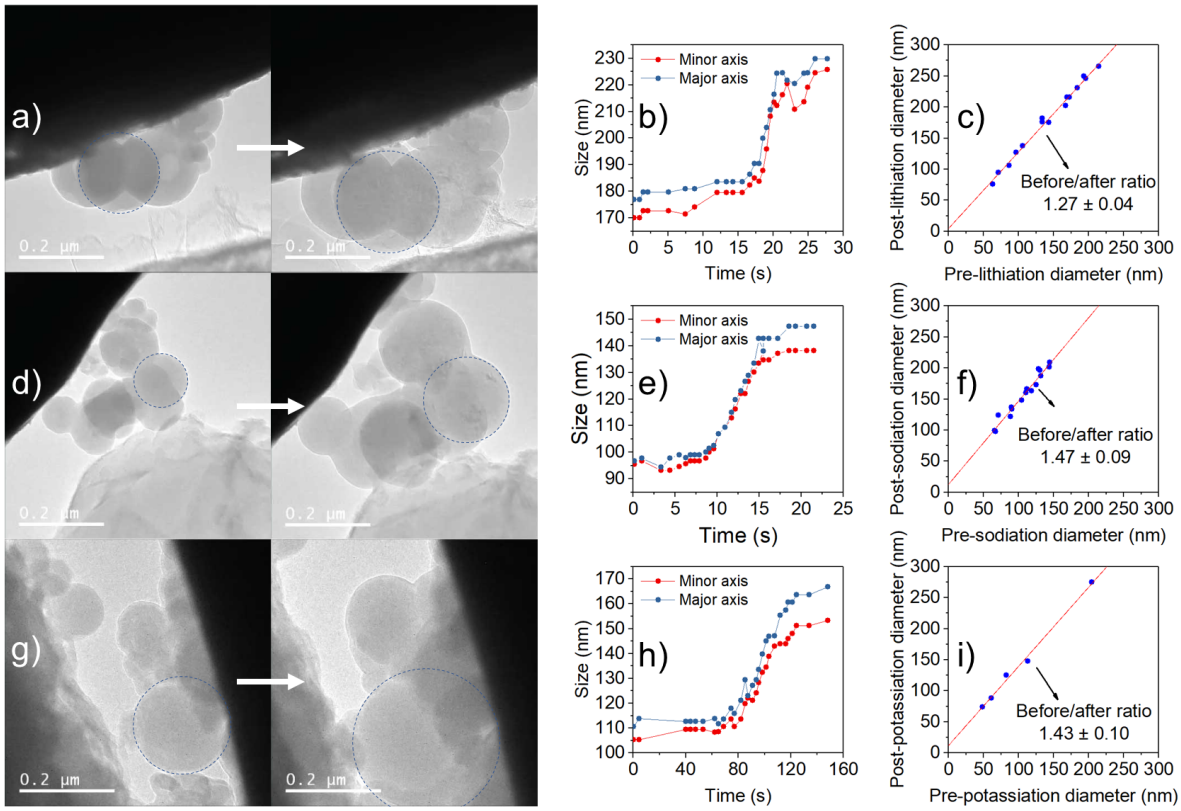


Figure 3.7: a) In-situ TEM experiments performed on spherical RP particles showing the particles before (left) and after (right) lithiation. b) size change of the particle with time during lithiation with red being the minor axis (perpendicular to the contact point) and red the major axis (parallel to the contact point). c) average size change of the diameter of the particles after the lithiation. (d-f) and (g-i) show the data collected from the same experiment using sodium and potassium, respectively. These experiments were performed with our collaborator Prof. Hyun-Wook Lee (Ulsan National Institute of Science and Technology, Ulsan, South Korea).

3.3.4 In-situ TEM: spherical RP particles

To validate the model, RP particles were charged using an open cell in-situ TEM setup. The procedure is explained in detailed in Section 2.2.6. This way, the volume expansion of the RP particles under extreme conditions can be observed. The experiment was firstly performed on RP spherical particles (Figure 3.7).

The volume expansion expected from the alloying reaction of RP with Li, Na and K were calculated considering the phases that are expected to form. For each ion, the

expected volume expansion is 168%, 331% and 162%, for Li, Na and K, respectively (see Appendix D).

In Figure 3.7(a,d,g), the volume expansion of the RP spherical particles when they alloy with Li, Na and K is shown. When alloying with the alkali metals, a similar elongation of both axis (parallel to the contact point of the metal tip and perpendicular to the contact point) was observed, showing that the expansion is isotropic and no cracks were observed.

This behaviour suggests that the shape of the particle (spherical in this case) and the starting size can suppress the formation of cracks, despite the high charging rate and the non-homogeneous flow of ions. The size of the particles measured before and after the alloying shows that lithiation provoked an increase of the size by a factor of 1.27 ± 0.04 (Figure 3.7c), resulting in an average volume expansion of 105 ± 20%. The value is lower than expected, suggesting that some of the RP has not reacted , possibly because of the presence of a thin oxide layer that is not clearly visible in this configuration or due to incomplete lithiation. Sodiation resulted in an average increase in the diameter of the particles of 1.47 ± 0.09 times (Figure 3.7f), resulting in a volume expansion of 217 ± 60%. This value is also lower than expected (331%). The possible causes may be similar to the Li case. Potassiation on average increased the diameter of the particle by 1.43 ± 0.10 times, resulting in a volume expansion of 192 ± 60%. However, the poor contrast of the image made the analysis more challenging. Nevertheless, the expected value (162%) lies in the range observed.

3.3.5 In-situ TEM: ball milled RP particles

To analyze the impact of the shape of the RP particles, ball milled commercial RP was also tested. The results are shown in (Figure 3.8). The shape of the particles can be described as oblate, generally larger than the spherical particles and with a rough surface. The volume expansion of these particles after charging was also calculated and resulted to be 72%, 179% and 217% for Li, Na and K respectively. These values are different from

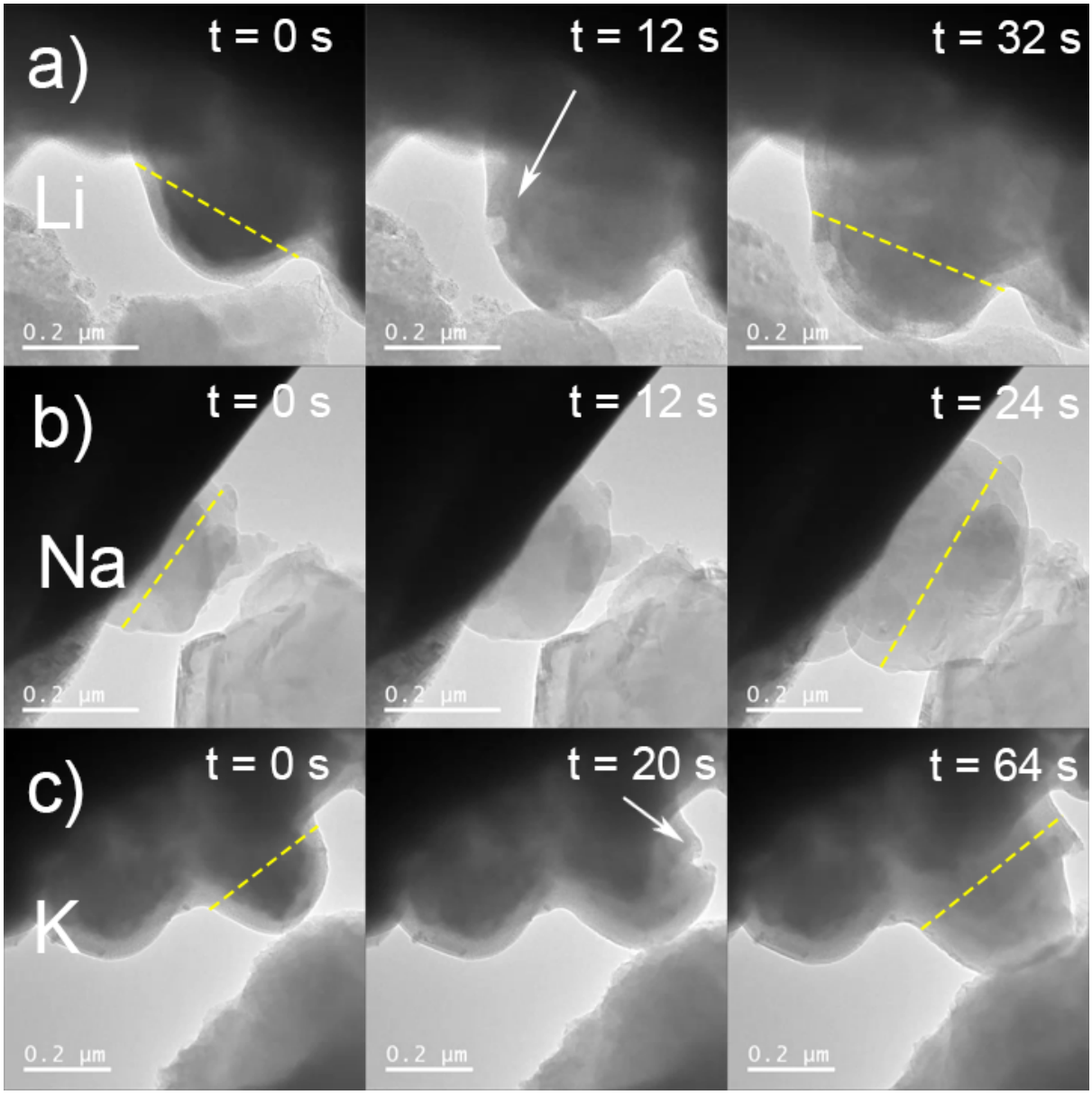


Figure 3.8: In-situ TEM experiments performed on ball milled commercial RP. Frames taken from videos collected during the experiments showing lithiation, sodiation and potassiation of the particles, respectively. The sequence from left to right shows the beginning of the experiment and the end of the reaction, respectively. The alkali metals that are used are lithium (a), sodium (b) and potassium (c). The white arrows point to the newly formed surface cracks on the particles. The yellow dashed lines show the axis that were measured to calculate the volume expansion. These experiments were performed with our collaborator Prof. Hyun-Wook Lee (Ulsan National Institute of Science and Technology, Ulsan, South Korea).

the spherical particles, but this can be related to error in the assumed particle dimension that is perpendicular to the imaging plane (depth), or the presence of an oxide layer.

Indeed, this layer is visible around the particles as a brighter layer, with a sharp change in contrast to the darker particle core. The brighter layer can be the result of less electron scattering, related to the different composition of the oxide compared to the bulk. Its thickness also remained unchanged after the reaction, supporting the conclusion of it being an oxide, which is electrochemically inactive.

Compared to the spherical particles, however, we observed that cracks form on the surface of the particles during lithiation and potassiation, as shown in Figure 3.8a and indicated with an arrow. These cracks are located at about 50 degrees from the contact point of the metal tip. The cracks grow to a length of about 50 nm before stopping.

Sodiation should also provoke the formation of cracks, as the stresses should be higher than lithiation. However, the lack of cracking in the particle could be an effect of the geometry of the particle and the direction of the flow of the ions, since the contact point of the Na tip with the RP particle lies on the long side instead of the short side, as in lithiation and potassiation. This could lead to a lower stress that prevents the formation of cracks.

Both in lithiation and potassiation, the cracks did not cause the catastrophic failure of the particle. Three reasons can be identified for this behaviour. First, the stress concentration at the tip of the crack leads to the blunting and plastic yielding of the crack tip. Second, the compressive stresses that are generated at the surface (shown in Figure 3.5) perturb mode I cracking. Third, The location and the scale of the cracks could offer a hint to another cause of the crack. These are mainly located on the oxide layer of the particle and not on the RP. The oxide layer on RP particles has been shown in past works to be as thick as $\approx$ 15-50 nm [21, 22]. A layer this thick can be present on ball milled commercial RP particles, as they are produced from commercial RP, which also presents an oxide layer. Although the preparation has been made in inert atmosphere that prevents further oxidation of RP, a, oxide layer can still be present. Spherical particles did not show an oxide layer with a visible thickness because they are chemically synthesized and proper care was taken to avoid exposure to air. However, catastrophic

failure of the particle has not been observed either in the spherical particles nor in the ball milled particles, even in conditions of extreme charging, in agreement with its mechanical properties.

3.3.6 In-situ TEM experiment modelling

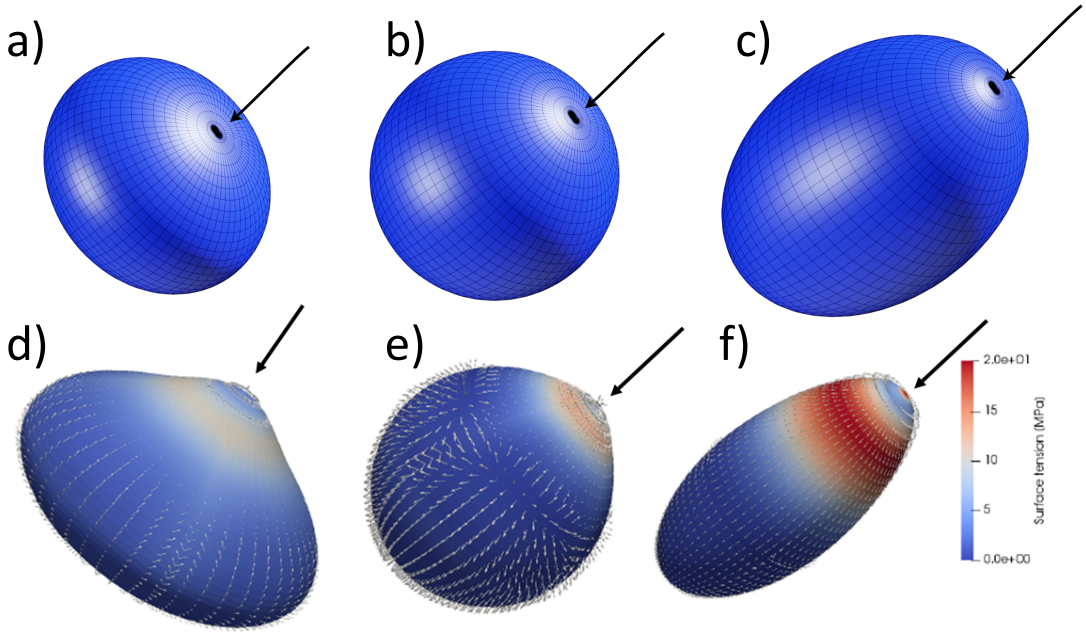


Figure 3.9: Modelling of RP alloying in in-situ TEM conditions (anisotropic flow of ions) and different particle geometry. a-c) Geometries considered in the model: oblate (a), spherical (b) and prolate (c). The black arrows show the point from where the ions will flow in the particles. In particular, for the oblate particle, the top of the short axis has been considered as contact point while the top of the long axis has been considered in the prolate particle. In d-c, the surface stresses of the corresponding cases are shown: oblate (d), spherical (e) and prolate (f). The grey arrows on the surface of the particles show the directions of surface stresses, and the coloured contour shows magnitudes of tensile stress along longitude direction. This model was developed in collaboration with Dr. Ying Zhao (Tongji University, Shanghai, China).

Using the model previously developed, the effect of the geometry of the particle and the flux of the ion were considered to simulate the two general cases observed with oblate spheroid particles, shown in Figure 3.9. This way the effect of ions entering the particle from one specific point, as in the case of in-situ TEM, can be studied. The diffusion of the ions in the particle can lead to a concentration gradient that also results in an

expansion gradient (the regions with high concentration expand before the other regions). This heterogeneous expansion can lead to tensile stresses as shown in Figure 3.9. The stresses in the model are located at about 50-60 degrees from the contact point. The stresses are also higher when the contact point is located on the long edge. This can also contribute to the normal stresses and lead to fracture. However, this behaviour is similar to the experimental conditions of in-situ TEM where we have extreme conditions given by directional loading and the tensile stress generated by the heterogeneous expansion decreases over time, as the particle is charged. These conditions do not occur in battery applications. This finding, however, offers an explanation of the results provided by the in-situ TEM testing of ball milled commercial RP particles, where cracks did not propagate through the particle.

3.4 Conclusions

In this chapter, a model that can calculate the stresses generated by a RP particle that alloys with Li, Na and K is shown. In order to develop and use this model, a number of mechanical and electrochemical properties of RP was needed. These properties were measured for the first time in this work. The model shows that the increase of the current applied to the system will increase the stresses related to the expansion of the particle, as expected. However, it is now possible to calculate the maximum stress level and if they could lead to plastic deformation or fracture. A simple model of a spherical particle with uniform flow of ions from the surface was used to simulate the stress. In this case, the maximal stresses are internal, meaning that a flaw of ∼160nm or bigger within a particle is needed to cause the failure by fracture of the particle (Figure 3.5e). Considering a commercial RP particle 10 µm in size that alloys with Li with a pore-wall ion current density of $\sim 1.5\,\mu A\,cm^{-2}$ (or a current density $15\,\mu A\,cm^{-2}$) we can predict that the plastic failure will occur, keeping electrical and ionic connection through the particle. The fracture of the particle will only occur if a pre-existing crack or flaw that

is 160 nm is already present on the RP particle. However, the presence of these flaws is not likely due to the modern production routes, suggesting that most of RP particles will not fracture during cycling. If a higher current density is considered ($10\,\mathrm{mA\,cm^{-2}}$ that equates to an ideal pore-wall current density of $\sim 25\,\mu\mathrm{A\,cm^{-2}}$, the critical radius would be $\sim$ 40 nm (larger yields plastically), meaning that the pre-existing flaw needed to cause the fracture would need to be bigger than the particle. This further supports the idea that RP fails plastically at moderate or high currents during cycling and that fracture does not occur. This means that fracture for RP particles is not an issue that influences its cycling and that research on the optimisation of this material should be focussed on other variables such as surface area-to-volume ratio (to optimize the coulombic efficiency on the first cycle), electronic conductivity, phosphorus-to-carbon ratio in the composite and microstructure of the electrode.

3.5 References

1. Zhao, Y. *et al.* A review on modeling of electro-chemo-mechanics in lithium-ion batteries. *Journal of Power Sources* **413,** 259–283 (2019).
2. Rissi, E. N. *et al.* Pressure-induced crystallization of amorphous red phosphorus. *Solid State Communications* **152,** 390–394 (2012).
3. Zaug, J. M. *et al.* Pressure-dependent structures of amorphous red phosphorus and the origin of the first sharp diffraction peaks. *Nature Materials* **7,** 890–899 (2008).
4. Zhu, Y. *et al.* Galvanostatic intermittent titration technique for phase-transformation electrodes. *Journal of Physical Chemistry C* **114,** 2830–2841 (2010).
5. Mayo, M. *et al.* Ab Initio Study of Phosphorus Anodes for Lithium- and Sodium-Ion Batteries. *Chemistry of Materials* **28,** 2011–2021 (2016).

6. Marbella, L. E. *et al.* Sodiation and Desodiation via Helical Phosphorus Intermediates in High-Capacity Anodes for Sodium-Ion Batteries. *Journal of the American Chemical Society* **140,** 7994–8004 (2018).

7. Sottmann, J. *et al.* Chemical Structures of Specific Sodium Ion Battery Components Determined by Operando Pair Distribution Function and X-ray Diffraction Computed Tomography. *Angewandte Chemie - International Edition* **56,** 11385–11389 (2017).

8. Yang, W. *et al.* First-Principles Study of Black Phosphorus as Anode Material for Rechargeable Potassium-Ion Batteries. *Electronic Materials Letters* **16,** 89–98 (2020).

9. Sultana, I. *et al.* High capacity potassium-ion battery anodes based on black phosphorus. *Journal of Materials Chemistry A* **5,** 23506–23512 (2017).

10. Chang, W. C. *et al.* Red Phosphorus Potassium-Ion Battery Anodes. *Advanced Science* **6** (2019).

11. Heckel, R. W. Density-Pressure Relationships in Powder Compaction (1961).

12. Rice, R. W. *Porosity of Ceramics* (CRC Press, 2017).

13. Zehnder, A. T. in, 185–219 (2012).

14. Hopcroft, M. A. *et al.* What is the Young's modulus of silicon? *Journal of Microelectromechanical Systems* **19,** 229–238 (2010).

15. Domnich, V. *et al.* Temperature dependence of silicon hardness: Experimental evidence of phase transformations. *Reviews on Advanced Materials Science* **17,** 33–41 (2008).

16. Petersen, K. Silicon as a mechanical material. *Proceedings of the IEEE* **70,** 420–457 (1982).

17. Chen C. P. Leipold, M. H. Fracture toughness of silicon. *American Ceramic Society Bulletin* **59,** 469–472 (1980).

18. Weaver, P. M. *Materials Selection in Mechanical Design. by Michael F Ashby* United Kingdom, 1999.

19. McDowell, M. T. *et al.* In Situ TEM of Two-Phase Lithiation of Amorphous Silicon Nanospheres. *Nano Letters* **13,** 758–764 (2013).

20. Doyle, M. *et al.* Modeling of Galvanostatic Charge and Discharge of the Lithium / Polymer / Insertion Cell. en. *Journal of The Electrochemical Society* **140,** 1526–1533 (1993).

21. Marino, C. *et al.* Interface and Safety Properties of Phosphorus-Based Negative Electrodes in Li-Ion Batteries. *Chemistry of Materials* **29,** 7151–7158 (2017).

22. Capone, I. *et al.* Effect of the Particle-Size Distribution on the Electrochemical Performance of a Red Phosphorus-Carbon Composite Anode for Sodium-Ion Batteries. *Energy and Fuels* **33** (2019).

Chapter 4

Effect of RP particle-size distribution

4.1 Introduction

This chapter is focused on the effect of the particle-size distribution of RP on the electrochemical performance of a RP-graphite composite.

As discussed previously, the volume expansion of RP can cause the failure of the electrode and ultimately poor cycle life. As shown in Chapter 3, however, the fracture of RP particles is not one of the causes that could lead to the failure of the electrode, as for example with Si. Therefore, attention needs to be focused on other properties on a composite level, such as the surface area-to-volume ratio (that depends on the particles-size distribution of the components), the P-to-C ratio and the preparation method of the composite.

Differently from the previous chapter, where the focus was on a particle level, now the attention will move to the entire composite. The particle-size distribution of RP was reduced and controlled in order to produce composites having RP particles with different sizes. Also, the milling time of RP with graphite was studied, monitoring the changes

occurring to the morphology of the composite and their electrochemical performance.

4.2 Results and discussion

4.2.1 Control of the RP particle size

In order to study both the effect of the particle-size distribution of RP and the effect of milling time of RP with graphite, on the electrochemical performance of the material, a two-step preparation procedure was developed to distinguish between the two factors. A schematic of the reaction is shown in Figure 4.1. Details about the synthesis of the composite are explained in Section 2.1.1. The first step of the synthesis of the RP-graphite composite is the reduction and control of the particle size of commercial RP by wet milling. The milling of the RP alone prior to the production of the composite allows for an accurate measure of its particle size distribution.

The milling was operated under argon in a zirconium oxide jar with the addition of EG, using 180 zirconia balls (5 mm ⌀). The presence of this solvent was important for four main reasons. Firstly, EG, being a reducing agent, can prevent the oxidation of RP during the milling. Secondly, the viscosity of EG can slow down the balls during the milling, resulting in lower energy being delivered at the moment of the impact. Indeed, high energies can induce a phase change from RP to BP, as shown by Ramireddy et al. and Sun et al.[1, 2] Moreover, the high boiling point of EG (197.3 °C) reduces the risk of overpressure during the milling due to the evaporation of the solvent. Also, the presence of a liquid in the jar prevents the reaggregation of secondary particles, increasing the milling efficiency. The evolution of the particle size distribution during milling was measured by DLS (see Section 2.2.1). This technique can provide a clearer picture of the size of all the particles that are present in the sample. The evolution of the particle-size distribution during milling is shown in Figure 4.2. The Dv90 value reported in the figure is a measure of how much the milling is affecting the particle size. It is in fact the size at which 90% of the particles (by volume) have a diameter smaller than that value. The

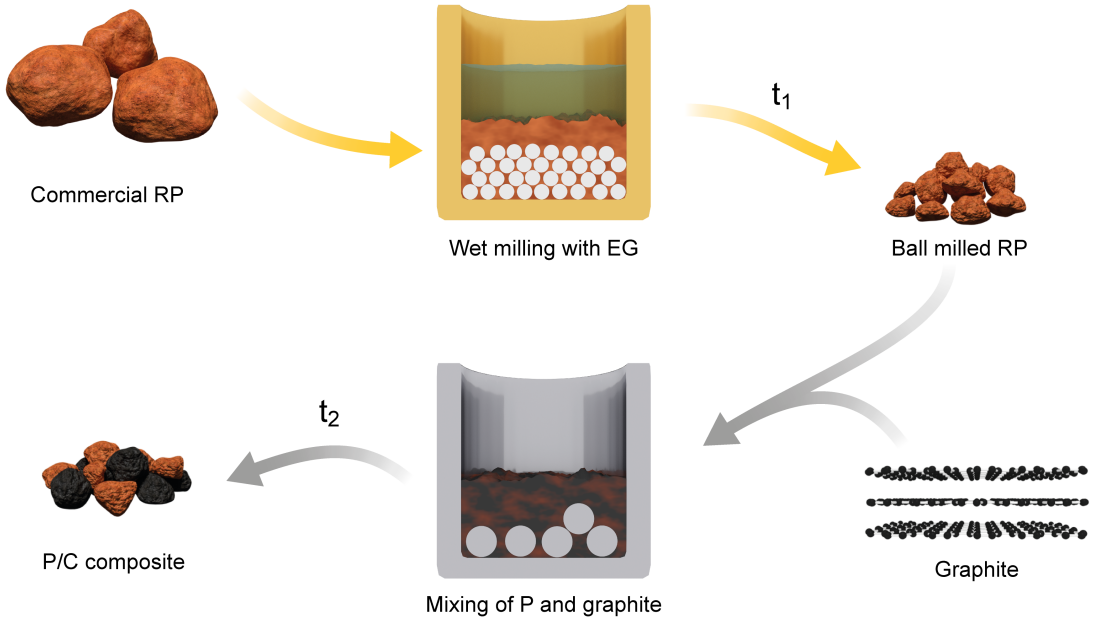


Figure 4.1: Schematic of the two-step milling procedure developed to prepare the RP-graphite composite. In the first step (gold arrows), commercial RP is wet ball milled in EG for time t_1 to reduce and control the particle size. Milling the RP alone allows for the accurate measurement of its particle-size distribution before formation of the composite. In the second step (silver arrows), the RP from step one is combined with graphite in a 7:3 ratio and dry ball milled for time t_2 to form an electronically conductive RP-carbon composite suitable for use as an anode.

commercial RP shows a very high Dv90 of about 12.49 µm. From Figure 4.2a it is clear that the majority of the particles have a size that is larger than 1 µm. After only 6 hours of ball milling, the Dv90 value decreases rapidly to 2.75 µm.

This is the largest drop in particle size that occurs during the milling. The rate at which the Dv90 values decreases reduced over time and achieved 0.79 µm after 60 h. The milling efficiency is greatly influenced by whether a media is used during the milling. Dry milling of commercial RP was performed in order to confirm this. After 24 h of dry milling (milling without the addition of any solvent), the particle-size distribution is only slightly affected by the milling, retaining a similar shape to the commercial RP, Figure 4.3. The Dv90 slightly decreased to 10.53 µm, as a result of the production of particles in the range 0.1 - 1 µm. Water was also tested as a solvent for its ease of use, safety and cost.

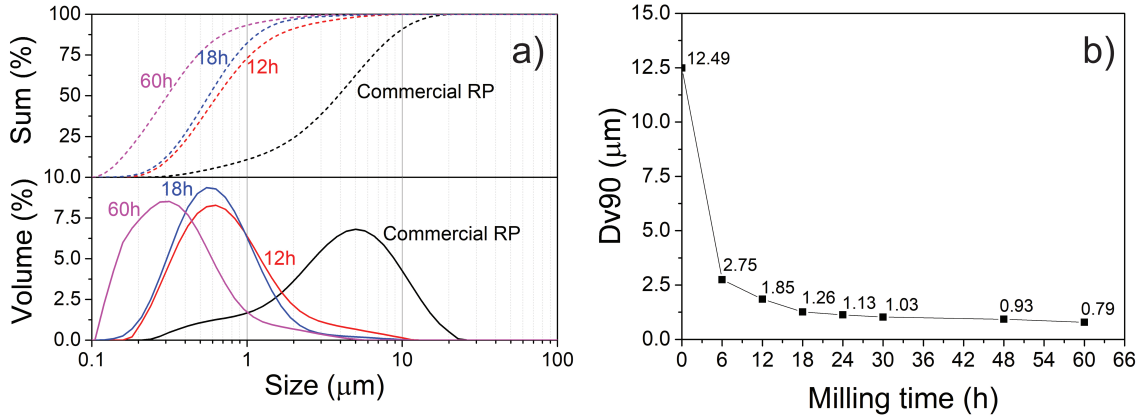


Figure 4.2: a) Particle-size distributions of commercial RP and ball milled RP. The distribution moves to the left to smaller size as the milling progresses. After 12 h the mode moves to about 0.6 µm. After 18 h the mode is almost unchanged 0.55 µm, but most of the particles in the range 2-10 µm have been milled. After 60 h, the particle-size distribution further moves to the left, with a mode of about 0.30 µm. b) Changes occurring to the Dv90 value (determined by DLS) as a function of milling time in EG.

The improved milling process observed with these experiments showed that the use of solvents was necessary in order to efficiently reduce the particle size of RP. In fact, after ball milling commercial RP for 24 h with water, a Dv90 of 3.88 µm was achieved (Figure 4.3a,b). The particle-size distribution shows that the addition of water can efficiently lead to the milling of particles bigger than 5 µm. However, issues related to the chemistry of water arise. The low viscosity and high dielectric constant of water, plus its reactivity with RP led to the production of impurities such as phosphates or oxides as shown in the XRD, Figure 4.3c (see Section 2.2.3 for details). Moreover, compared to water milling and dry milling, the addition of EG resulted in the most efficient procedure. After 24 h, a Dv90 of 1.13 µm was achieved, and no impurities are visible after the milling. SEM analysis on the commercial RP that was ball milled for 60 h shows that, compared to commercial RP where particles larger than 1 µm are clearly visible, the majority of the particles are smaller than 1 µm, although they tend to aggregate into secondary particles. In order to test the electrochemical performance of the ball milled RP, the production of a RP-graphite composite was necessary, in order to increase the electronic conductivity of the material. Therefore another milling step is required. In this case, measures need

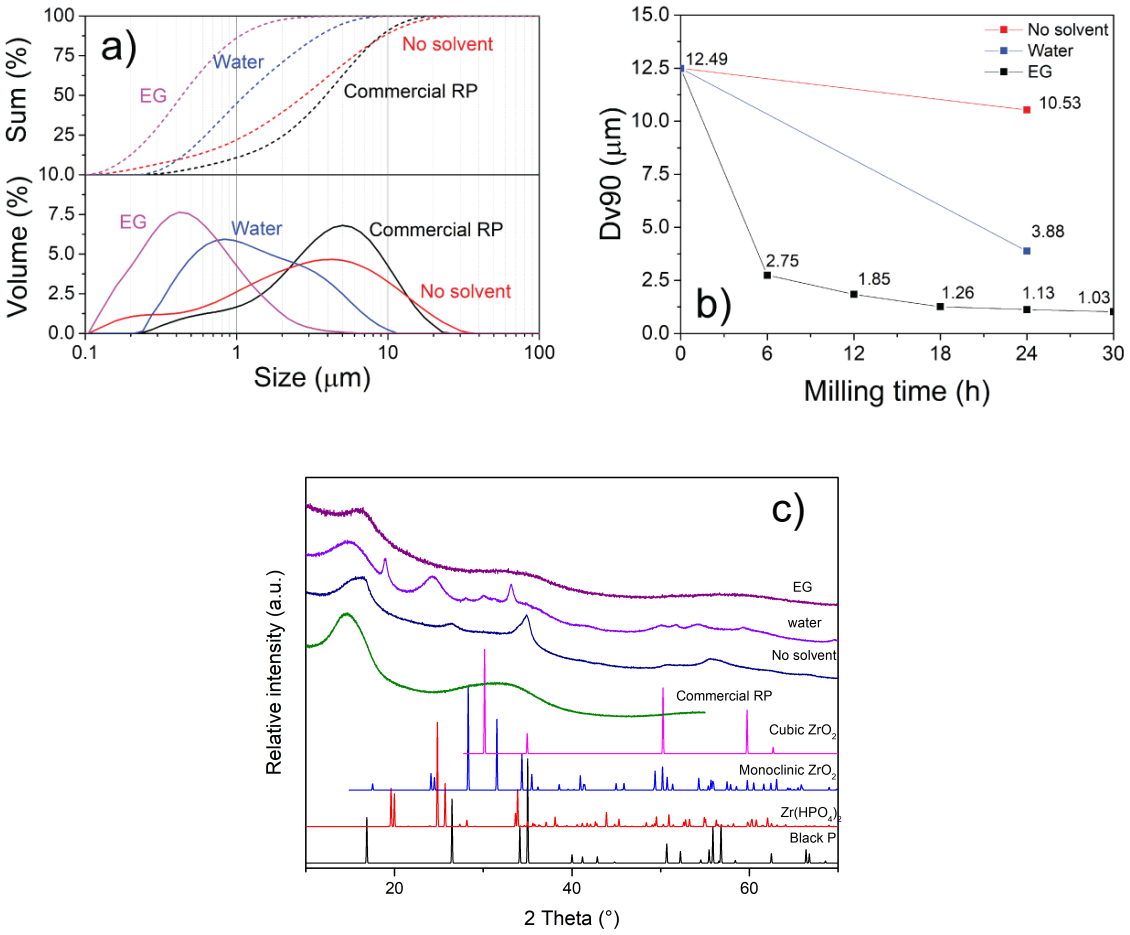


Figure 4.3: a) Particle-size distribution of commercial RP, dry milled RP, wet milled RP with water and EG, for a total milling time of 24 h. b) Dv90 changes of RP milled in different media. c) XRD of RP milled in different media, compared to common impurities and black phosphorus.[3–6]

to be taken to prevent further reduction of the RP particle size. As shown by Kabezya et al., in a sample, the size of the particles that are affected by the milling depends on the size of the balls used during the process.[7] In particular, they showed that the size of the balls affect a size-range of particles that are specific to each material, and that as the particle-size distribution is reduced, smaller balls are needed to further decrease it. For this reason, to reduce the risk of further milling of RP during the preparation of the composite in this step, we operated with dry milling using a smaller number (5) of larger balls (1 cm ⌀).

Electrochemical tests were performed to understand how the RP particle-size distribution affects the electrochemical performance of the material. However, as mentioned earlier, RP has a very low electronic conductivity, and its combination with a carbon additive is needed in order to increase it. However, the addition of a carbon additive can influence the performance of the composite.[8] To ensure that the results of the electrochemical measures were related to the RP and not from the carbon additive, we decided to use graphite as the carbon additive and perform the tests with Na for several reasons. First, sodium does not intercalate in graphite, so its contribution can be discarded.[9] Moreover, graphite has a high electrical conductivity and lubricating properties that can be effective in mitigating further milling of RP particles during the preparation of the composite. Also, graphite can exfoliate and form graphene layers when ball milled, allowing for the formation of a carbon coating on the particles and enhancing the electronic conductivity of the material.[2] The P/C ratio used in this step (7/3) is widely reported in literature as the optimal ratio to achieve the best performance with the highest addition of RP.[1, 10, 11]

4.2.2 Electrochemical performance: RP particle size

To test the effect of the RP particle-size distribution on the electrochemical performance of the composite, galvanostatic cycling (GC) experiments were performed using three composites prepared with RP samples having different particle-size distribution. In particular, RP samples ball milled for 12, 18 and 60 h were used. These milling times were chosen due to the evenly spaced Dv90 values of 1.85, 1.26 and 0.79 µm respectively. The composites were prepared by mixing these samples with graphite for 24 h (Section 2.1.1). The electrodes containing the three composites were prepared following the procedure explained in Section 2.1.3. GC tests were performed using 2032 coin cells with Na as both the counter and reference electrode. 1M $NaPF_6$ in EC:DEC 1:1 with the addition of FEC (10%) was used as electrolyte. Further details about the electrochemical experiments are provided in Section 2.3.1. The galvanostatic profiles of the three composites

tested at C/15 are shown in Figure 4.4.

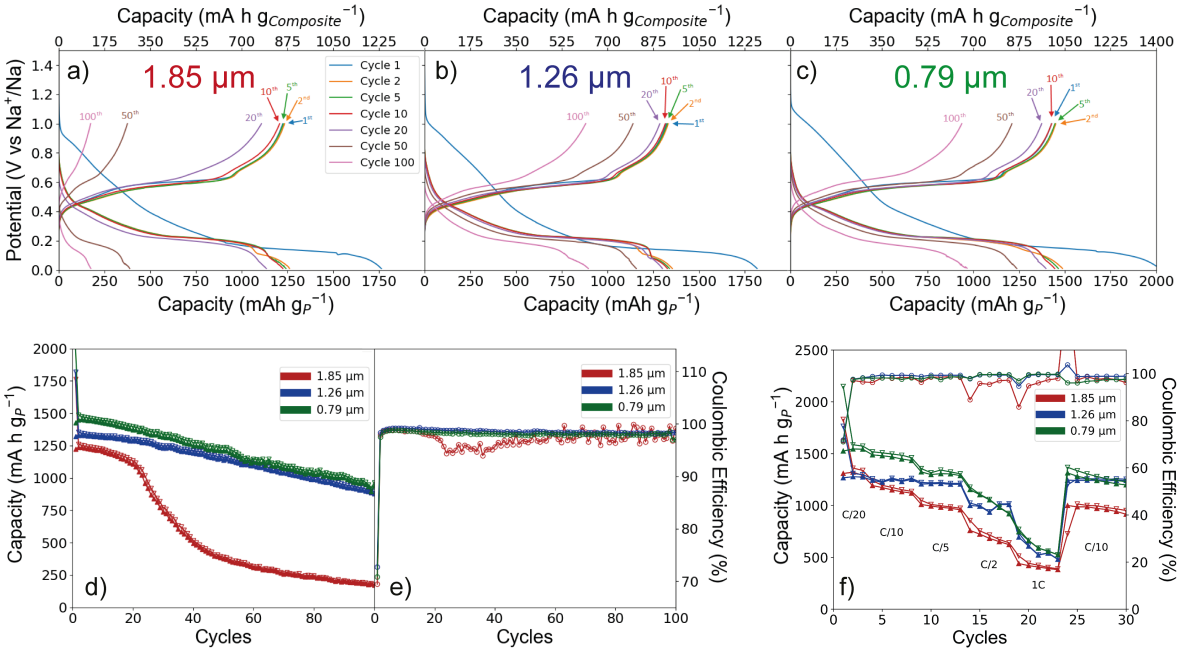


Figure 4.4: Electrochemical performance of RP-graphite composites prepared with different RP particle-size distributions (t_1 = 12 h, 18 h and 60 h, Dv90 shown on the plots), prepared by ball milling RP and graphite for 24 h. a-c) Galvanostatic profiles of the composites cycled at C/15. d) Discharge (open markers) and charge (closed markers) capacity of the three composites at each cycle. e) Coulombic efficiencies of the galvanostatic cycles shown in (d). f) Capacity delivered by the composites at different C rates and their coulombic efficiencies.

The profiles all show on the first discharge a slope in the range 1.2 - 0.2 V vs Na^+/Na. This is only present on the first cycle and is related to the electrolyte degradation at such potentials and consequent formation of the Solid electrolyte interphase (SEI) on the electrode. Also, a plateau at about 0.2 V vs Na^+/Na is clearly visible. This is related to the reduction of RP and the formation of the Na_3P phase, that ultimately leads to the volume expansion of the RP particles.[12] When charged, the profiles show a plateau at about 0.6 V vs Na^+/Na, related to the reduction to amorphous phosphorus. The capacity retention of the three composites, as well as their coulombic efficiencies, are shown in Figure 4.4d,e. The behaviour of the composite prepared using the RP sample with Dv90 of 1.85 µm shows a high capacity of about 1224 mAh g_P^{-1} on the first charge and is able to retain most of the capacity for about 20 cycles. Then the capacity quickly

decreases and the material is able to deliver only about 376 mAh g_P^{-1} after 50 cycles. As discussed earlier, this behaviour is well documented and attributed to the volume expansion of RP, and failure of the electrode. Composites with smaller particles did not show this behaviour. This supports the statement that smaller particles mitigate the effect of the volume expansion on the stability of the electrode and therefore its failure. Indeed, the material prepared using RP with a Dv90 of 1.26 µm shows a superior cycle life. Although the particle-size distribution of both the RP samples used to prepare the composites have a mode at about 0.55 µm, shown in Figure 4.2b, the sample that was ball milled for 18 h has a reduced number of particles with a size larger than 2 µm. The removal of these particles resulted in a material with a longer cycle life and able to retain 67% of the capacity after 100 cycles. Further reduction of the particle size to achieve a Dv90 of 0.79 µm only resulted in the production of a composite with an increased capacity, but the cycle life of the material remained similar to when the sample with Dv90 of 1.26 µm. This finding shows that the milling of particles bigger than 2 µm is essential to increase the cycle life of the composite.

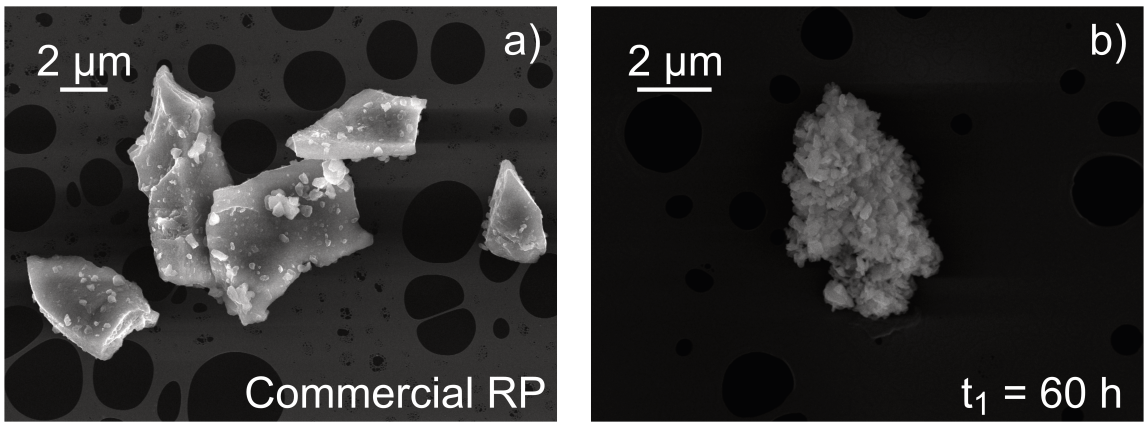


Figure 4.5: SEM images of commercial RP (a) and ball milled RP for 60 h (b)

On the first cycle, all three composites showed a low coulombic efficiency of about 70%. As discussed earlier, the electrolyte is irreversibly reduced on the first discharge, resulting in the formation of the SEI. In general, the SEI is directly related to the surface area of the material, so a larger surface area and a lower coulombic efficiency is expected

for the composite with the smallest RP particle-size distribution. However, in this case the primary particles in the composites form aggregated secondary particles with roughly equivalent surface Figure 4.5.

The rate capability of these composites was also studied, and the results are shown in Figure 4.4f. The electrodes were cycled at increasing currents, up to 1C. The capacity of all the composites slightly decreases as the current rate increases from C/20 to C/5. At C/2 and 1C, the capacity for all the samples is constantly decreasing, with the exception of the composite with intermediate RP particle-size distribution, which shows good capacity retention at C/2. The capacity is fully recovered when slower rates such as C/10 are applied to the materials, meaning that the low rate capability at high rates is mainly related to the electronic conductivity of the electrodes.

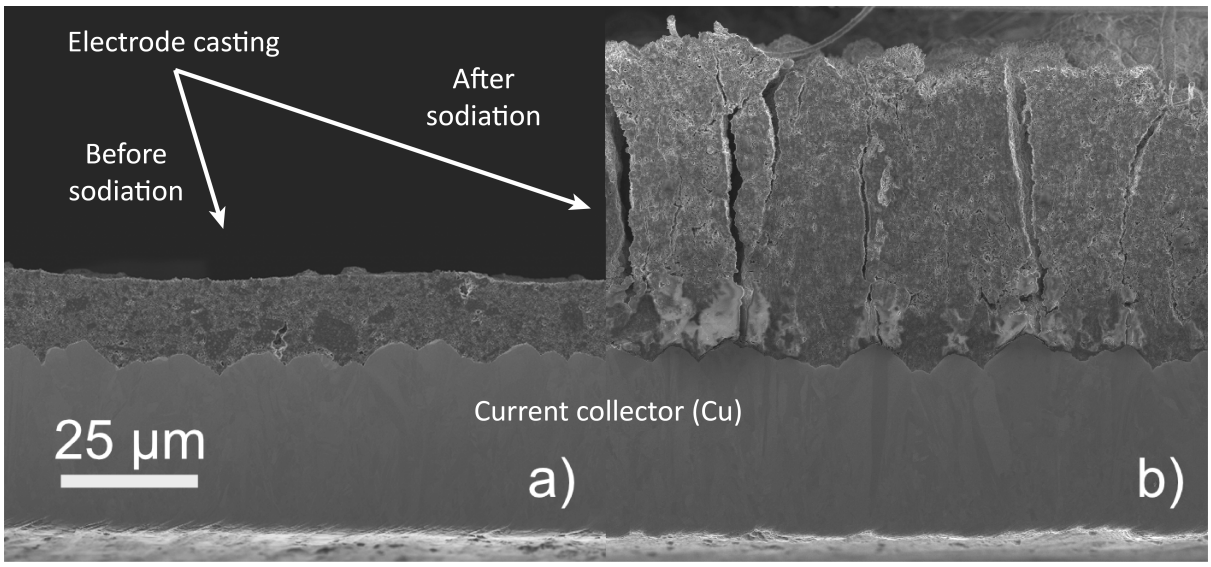


Figure 4.6: Crossection of the RP-graphite electrode before cycling (a) and after 100 cycles at C/15 (b). The electrode in (b) is shown in the sodiated (discharged) state.

It is important to note that, although the reduction of the particle size can improve the stability of the electrode, this does not prevent the RP particles from expanding. A visual comparison of the electrode (t_1 60 h, $t_2 = 24$ h) before and after sodiation is shown in Figure 4.6. The thickness of the casting increases from 15 µm to about 50 µm when sodiated. The expansion is related to the volume expansion of the RP. Cracks on the electrode casting are also visible. These can be the result of the expansion/contraction

cycles, but can also be a product of decrimping procedure that damaged the electrode.

4.2.3 Electrochemical performance: RP-graphite mixing

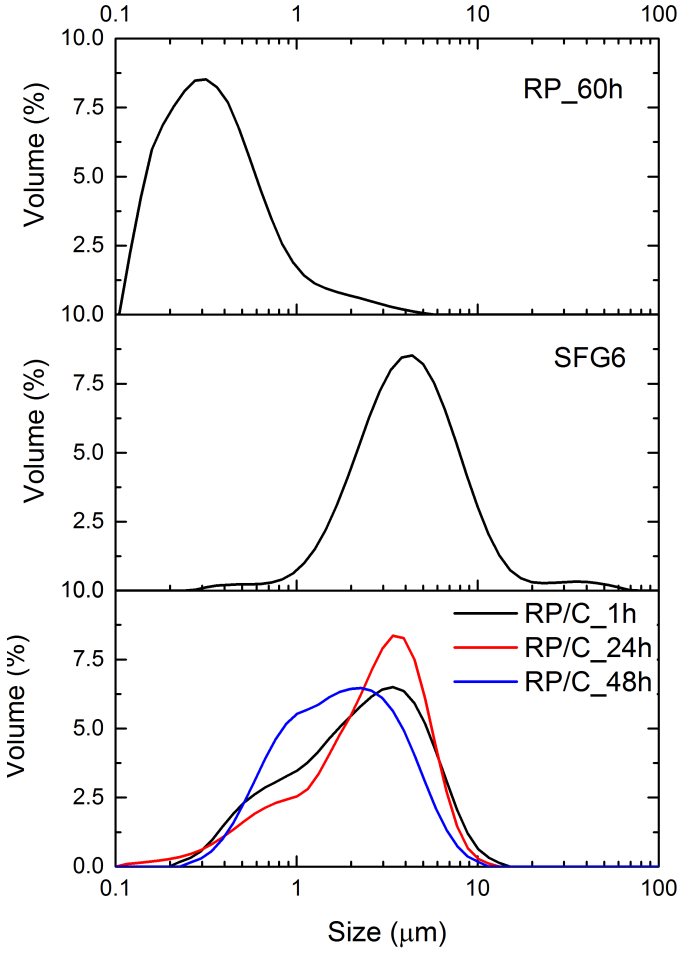


Figure 4.7: Particle-size distribution of commercial RP (top), pristine graphite (middle) and RP-graphite composites prepared by ball milling for 1 h, 24 h and 48 h (bottom).

The effect of the mixing time of the RP with graphite was also studied. For this study, the RP sample with the smallest particle-size distribution (0.79 µm) was selected because it exhibited the highest capacity when compared to the other ones. The sample was mixed with graphite for 1, 24 and 48 h. Longer mixing times were not investigated as they may be not applicable to large scale production. As discussed earlier, avoiding further milling of the RP particles during this step is of paramount importance. However,

measuring the RP particle size in the composite via DLS can be extremely challenging due to the presence of the graphite particles. In Figure 4.7, the particle size distribution of the three RP-graphite composites is shown. All three particle-size distributions show two peaks, related to single RP and graphite particles and aggregates of these two materials. However, no particles smaller than the initial RP particle-size distribution were observed in each case. This suggests that no further milling of RP occurred in the second milling step. The composites were tested at C/15 and their galvanostatic profiles are shown in figure Figure 4.8a-c.

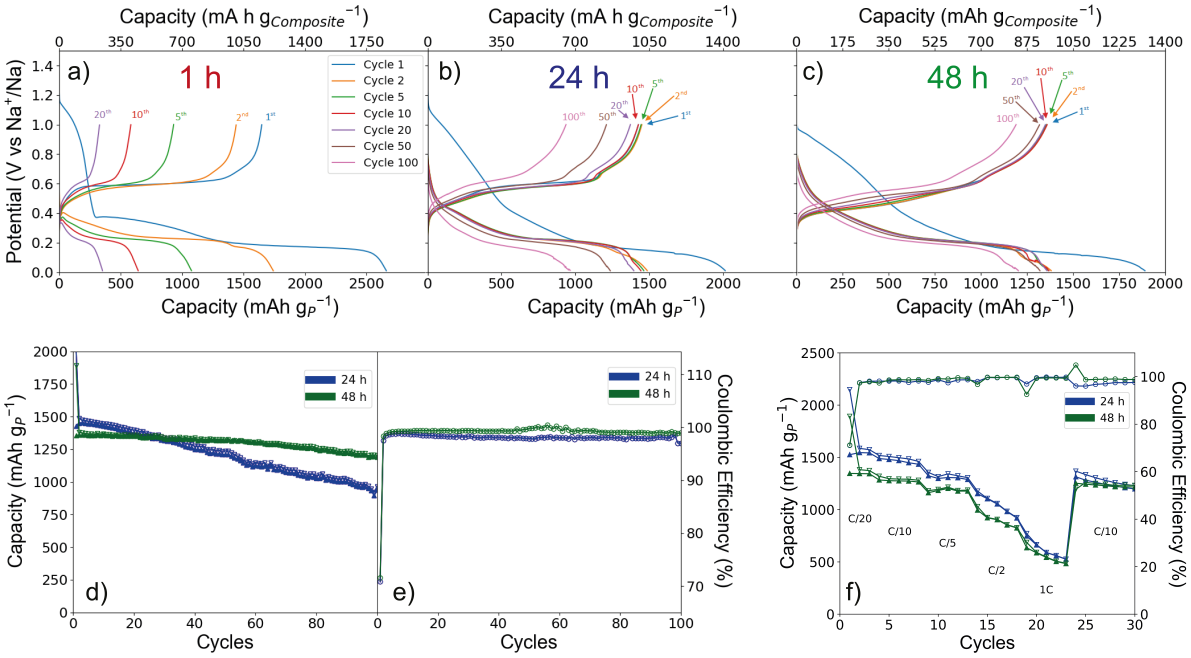


Figure 4.8: Electrochemical performance of RP-graphite composites prepared with different mixing times of RP with graphite (t_2 = 1 h, 24 h and 48 h), prepared using RP with the smallest Dv90 (0.79 µm, t_2 = 60 h). a-c) Galvanostatic profiles of the composites cycled at C/15. d) Discharge (open markers) and charge (closed markers) capacity of the three composites at each cycle. e) Coulombic efficiencies of the galvanostatic cycles shown in (d). f) Capacity delivered by the composites at different C rates and their coulombic efficiencies.

The composite prepared by mixing RP with graphite for only 1 h showed poor performances and delivered about 20.9% of the initial capacity after 20 cycles. However, the best performance were achieved by the composite ball milled for 48 h, which showed a high capacity on the first cycle of about 1354 mAh g^{-1} and was able to retain 88% of

the capacity after 100 cycles, with a coulombic efficiency above 99% Figure 4.8d,e. The rate capability was also tested as shown in Figure 4.8f. All the composites were able to deliver most of the initial capacity at C/5, but as before, a slow capacity decay occurs when higher currents are applied. Again, the materials are able to recover full capacity when a C/10 rate is applied again to the material, meaning that the decay is related to the electronic conductivity of the composites.

The morphology of the RP-graphite composite prepared using the RP sample with Dv90 of 0.79 µm and ball milled with graphite for 48 h was investigated in order to understand the reasons of its superior cycle life. SEM-EDX analysis of the cross section of the electrodes was conducted to study the distribution of the elements in the material. As shown in Figure 4.9, the EDX analysis demonstrates that the milling time of RP with graphite improves the mixing of the two components. After only 1 h, P-rich areas and C-rich areas are clearly distinguishable in the electrode, and this poor mixing can be the reason of its poor electrochemical performance.

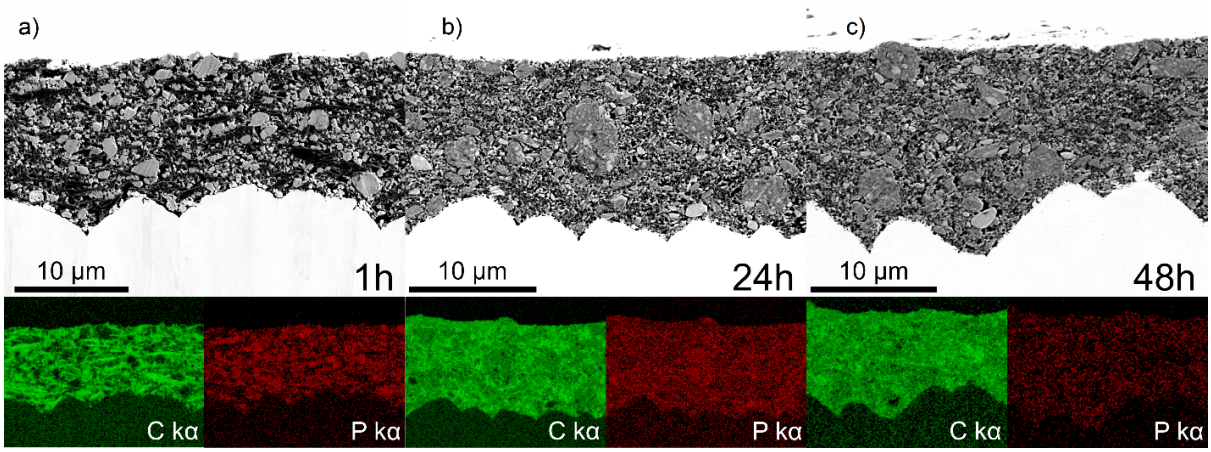


Figure 4.9: Cross sections of the electrodes. The three images are of the composites ball milled for a) 1, b) 24, and c) 48h. SEM and EDX data show that the spatial distribution of the elements increases with milling time.

After 24 h, the mixture becomes more uniform and gets even more homogeneous after 48 h. Moreover, after 48 h milling, XRD analysis still shows the presence of graphite peaks, although they are lower in intensity and broader compared to pristine graphite, Figure 4.10a. This can be indicative of an amorphisation of the graphite consequent of

the ball milling step. XRD also shows the presence of a weak peak from BP, which is the product of the partial conversion of RP to BP due to the ball milling step.

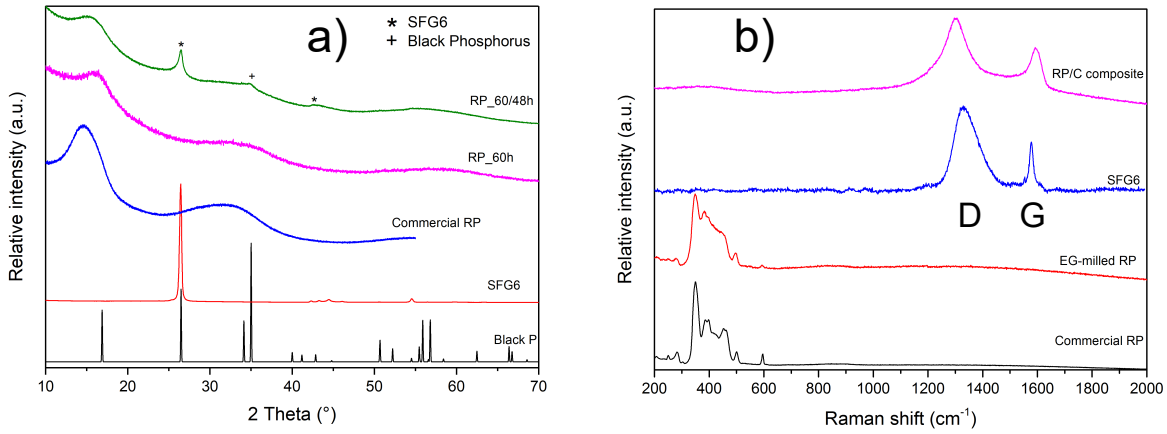


Figure 4.10: a) XRD of commercial RP, ball milled RP (t_1 = 60 h) and RP-graphite composite (t_1 = 60 h, t_2 = 48 h). b) Raman profiles of the above-mentioned samples.

The composite analyzed by Raman spectroscopy shows two distinct peaks from carbon (D peak and G peak) but no peaks related to RP, which are expected in the region 300 - 600 cm^{-1} (Figure 4.10b). This further suggest the presence of a coating that covers the RP particles. Moreover, the G peak in the composite, compared to the pristine graphite, is shifted to higher frequency from 1578 to 1597 cm^{-1}. This behaviour has been reported when few-layers graphite are present.[13] TEM analysis was performed to further investigate the morphology of the composite, Figure 4.11.

TEM shows the presence of crystal layers separated by 0.34 nm on the surface of the composite particles. The spacing is equal to the interlayer space between graphite's (002) crystal planes.[14] This finding confirms that the exfoliation of graphite occurred during the milling and that exfoliated graphene layers are present on the surface of the particles. TEM-EDX performed on the sample show the homogeneous distribution of the two elements in the composites, but the resolution is not high enough to confirm the presence of a carbon coating on the phosphorus particles.

Energy-tuned PES was performed on the composite to acquire more information about

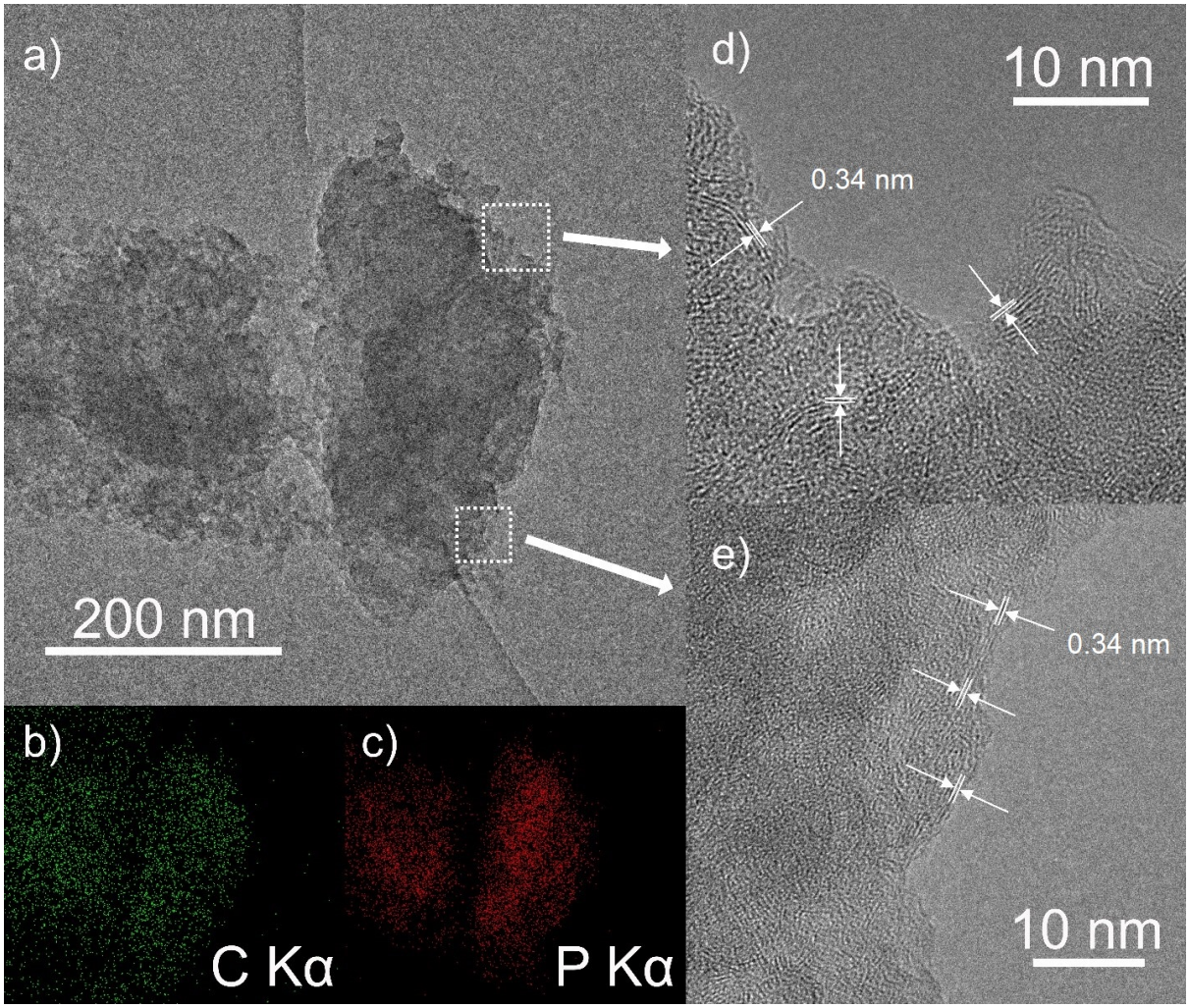


Figure 4.11: a) TEM image of the RP-graphite composite (t_1 = 60 h, t_2 = 48 h) and (b,c) EDX spectra of carbon and phosphorus. d,e) close up of figure (a) showing the presence of graphene layers around the particles. The spacing found between the layers is about 0.34 nm. The TEM analysis on the composite was performed by a DPhil student in the group: Albert W. Xiao (University of Oxford).

the elemental distribution in the particles. Three different photon energies were used (as explained in Section 2.2.4) to obtain information at increasing probe depths. The spectra from the P2p region and C1s region were fitted and the areas of the peaks were integrated. In the P2p region, Figure 4.12, the most intense peak is related to the P-P bonds. Moreover, when low photon energies are uesd, two main peaks at 133 eV and 130.1 eV related to the P-O and P-C bonds respectively can be observed, Figure 4.12b-d. P-O bonds can be related to the natural oxidation of the surface of phosphorus particles while the P-C bonds can be related to the presence of a carbon coating. A small peak

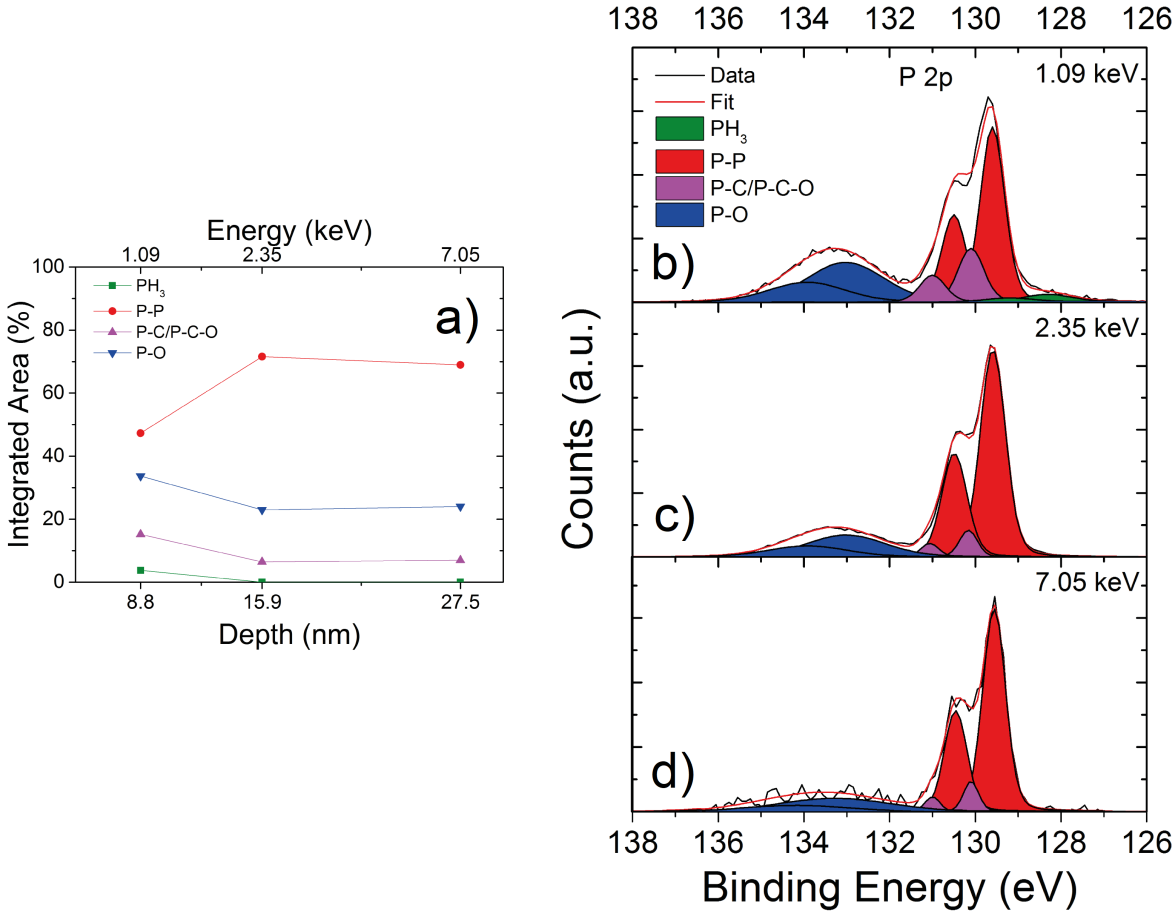


Figure 4.12: a) Ratio between the integrated areas of the peaks fitted in the P 2p region of the photoelectron spectra collected from the composite at increasing probing depth (b-d). The PES analysis on the electrode material was performed by our collaborator Dr. Andrew J. Naylor (Uppsala University, Uppsala, Sweden) at Diamond Light Source.

that can be assigned to the presence of PH_3 bonding is also visible. This can be related to the partial reduction of RP due to the exposure to humidity. The use of higher photon energies provided more information about the bulk of the material. While the peak related to PH_3 bonds is no more visible in the spectra, the peaks related to P-O and P-C bonds reduce drastically in intensity. In particular, the intensity of the peak related to the P-C bonds reduces by about half the intensity when the probe depth is about 15.9 nm and stays constant when higher photon energies are used (Figure 4.12a). Similarly, the intensity of the peak related to the P-O bonds reduces of about 30% at a probing depth of 15.9 nm and stays constant. The peak related to the P-P bond, on the other hand,

increases in intensity of about 50% at a higher probing depth, meaning that the bulk of the P particles was being sampled. The C1s region, among several peaks related to C-C bonds (sp^2 and sp^3) and C-O bonds related to the oxidation of the carbon material, also shows a peak at 283.2 eV related to the presence of P-C bonds (Figure 4.13). Similarly to the P region, increasing probe depths result in a decrease in intensity of the peaks related to P-C and C-O bonds and an increase in the C-C bonds, arising from the bulk of the material.

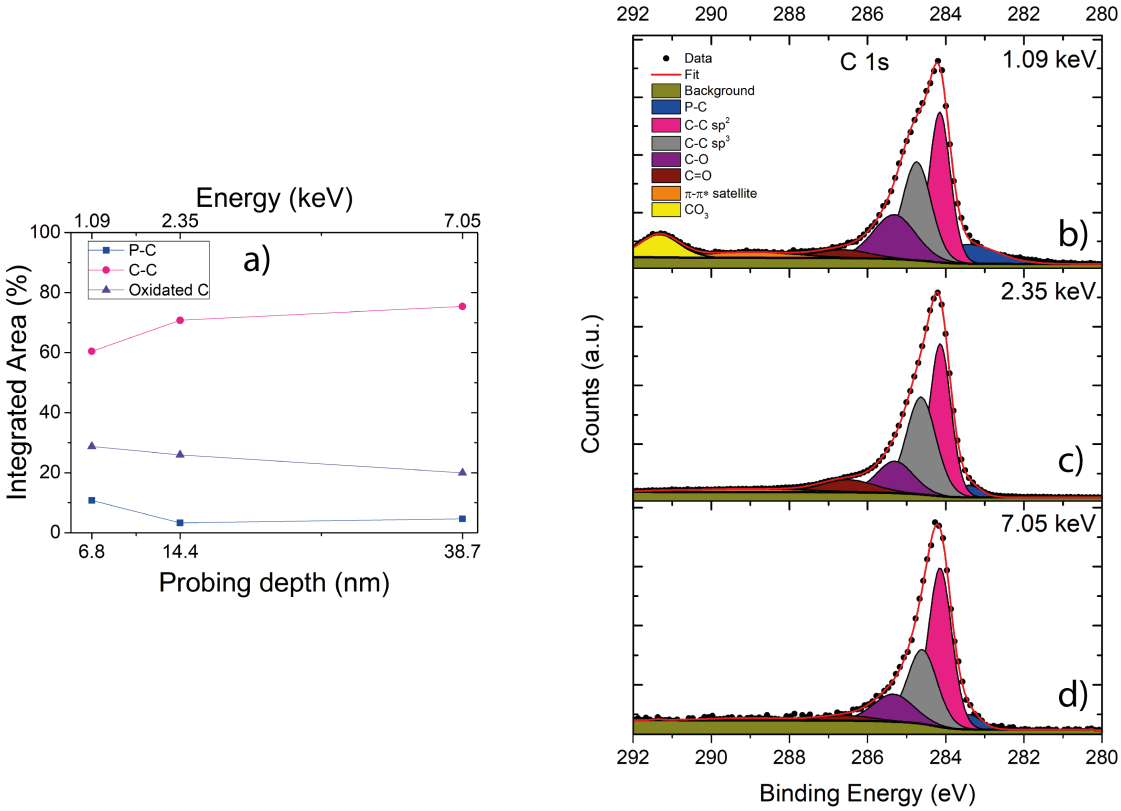


Figure 4.13: a) Ratio between the integrated areas of the peaks fitted in the C 1s region of the photoelectron spectra collected from the composite at increasing probing depth (b-d). The PES analysis on the electrode material was performed by our collaborator Dr. Andrew J. Naylor (Uppsala University, Uppsala, Sweden) at Diamond Light Source.

4.3 Conclusions

This work allowed for an in-depth study of how the particle-size distribution of RP affects the electrochemical performance of the composite for NIBs. This study was made possible by separating the ball milling procedure in two steps. The first step allowed for the reduction, measure and control of the particle size of RP via a wet milling technique that used EG to improve the milling efficiency as well as the safety of the procedure. The second step concerned the production of the composites using RP samples with a known particle-size distribution, with proper care to avoid further reduction of the size of the RP particles.

Our findings show that, when RP with a Dv90 of 1.86 µm is used to prepare a composite, a material with short cycle life and fast capacity fade after 20 cycles is produced. The breaking of particles larger than 2 µm achieved after 18 h of ball milling, resulting in a material with Dv90 of 1.26 µm with prolonged cycle life and able to retain 67% of the capacity after 100 cycled. Further milling of RP does not significantly improve the cycle life of the composite, but increases its capacity. This study indicates that breaking the particles that are larger than 2 µm is the critical step to achieve in order to mitigate the effect of the volume expansion of RP particles on the electrode, that could lead to damages on the electrode and loss of electric contact between the particles, resulting in capacity loss. By reducing the particle size of RP, materials with long cycle life and better performance can be produced.

The study on the effect of the mixing time of RP with graphite also showed that a carbon coating is formed on the particles when graphite is ball milled. This is mainly related to the exfoliation of graphene layers during the ball milling step. This contributes to the increased performance of the electrode material, mainly because of a homogeneous distribution of the two elements, ensuring the electrical contact between the particles. After 48 h milling, a composite able to retain 88% of the initial capacity after 100 cycles is produced. It is expected that the performance will increase with longer mixing time.

However, the milling process may result too long and to expensive for practical use in large scale production. Proper optimization of the mixing time is therefore required to achieve the high performance with the shortest mixing time.

These results give important insights into the effect of the size of RP particles that are used to prepare the composites, and the maximum particle size that can be employed to achieve high performance phosphorus anodes for NIBs.

4.4 References

1. Ramireddy, T. *et al.* Phosphorus–carbon nanocomposite anodes for lithium-ion and sodium-ion batteries. *Journal of Materials Chemistry A* **3,** 5572–5584 (2015).
2. Sun, J. *et al.* Formation of Stable Phosphorus–Carbon Bond for Enhanced Performance in Black Phosphorus Nanoparticle–Graphite Composite Battery Anodes. *Nano Letters* **14,** 4573–4580 (2014).
3. Cartz, L. *et al.* Effect of pressure on bonding in black phosphorus. *The Journal of Chemical Physics* **71,** 1718–1721 (1979).
4. Martin, U. *et al.* Neutron powder investigation of tetragonal and cubic stabilized zirconia, TZP and CSZ, at temperatures up to 1400 K. *Acta Crystallographica Section B Structural Science* **49,** 403–413 (1993).
5. Kudoh, Y. *et al.* In Situ Determination of Crystal Structure for High Pressure Phase of ZrO2 Using a Diamond Anvil and Single Crystal X-ray Diffraction Method. *Phys. Chem. Miner* **13,** 233–237.
6. Alberti, G. *et al.* Characterization, and Structure of α-Zirconium Hydrogen Phosphate Hemihydrate. *J. Solid State Chem* **113,** 289–295.
7. Kabezya, K. *et al.* The Effect of Ball Size Diameter on Milling Performance. *Journal of Material Science & Engineering* **04** (2014).

8. Nitta, N. *et al.* Influence of Binders, Carbons, and Solvents on the Stability of Phosphorus Anodes for Li-ion Batteries. *ACS Applied Materials & Interfaces* **8,** 25991–26001 (2016).

9. Moriwake, H. *et al.* Why is sodium-intercalated graphite unstable? *RSC Advances* **7,** 36550–36554 (2017).

10. Kim, Y. *et al.* An amorphous red phosphorus/carbon composite as a promising anode material for sodium ion batteries. *Advanced Materials* **25,** 3045–3049 (2013).

11. Li, W.-J. *et al.* Simply Mixed Commercial Red Phosphorus and Carbon Nanotube Composite with Exceptionally Reversible Sodium-Ion Storage. *Nano Letters* **13,** 5480–5484 (2013).

12. Mayo, M. *et al.* Ab Initio Study of Phosphorus Anodes for Lithium- and Sodium-Ion Batteries. *Chemistry of Materials* **28,** 2011–2021 (2016).

13. Ferrari, A. C. Raman Spectroscopy of Graphene and Graphite: Disorder, Electron–phonon Coupling, Doping and Nonadiabatic Effects. *Solid State Commun* **143,** 47–57.

14. Steurer, W. in *Reference Module in Materials Science and Materials Engineering* (Elsevier, 2017).

Chapter 5

RP-graphite as anode material for KIBs

5.1 Introduction

The optimisation of the RP-graphite composite shown in Chapter 4 resulted in a material with high stability and superior cycle life. The best performing composite was the one prepared by ball milling RP in EG for 60 h, thus achieving a particle-size distribution with a Dv90 of 0.79 µm, and mixed with graphite for 48 h. This resulted in a composite having a homogeneous distribution of the two elements in the material and the formation of a carbon coating on the surface of the particles. This way, we were able to synthesize an anode for NIBs. As mentioned in Chapter 1, KIBs are also a promising alternative to LIBs because of the similar low reduction potential of K compared to Li (-2.93 V and -3.01 V vs SHE, respectively) and the large abundance of K. Moreover, differently from the Na case, graphite, the most used anode in LIBs, is also able to intercalate K^+ ions. However, the theoretical capacity delivered is lower ($279\,mAh\,g^{-1}$).[1, 2] Therefore an anode with a higher capacity (such as RP) would be ideal to push the development of high energy density KIBs. As demonstrated in Chapter 4, the reduction of the particle size prior

to the preparation of the composite allowed for the development of a composite with superior cycle life with Na.[3] Using the knowledge we gained from that work, we tested the material with K to confirm the synthetic procedure that we developed in Chapter 4 is also valid for K. The RP-graphite composite showed superior performance with K, delivering a very high first charge capacity ($723\,\mathrm{mA\,h\,g_P^{-1}}$ compared to the theoretical $865\,\mathrm{mA\,h\,g_P^{-1}}$) and a good rate capability, retaining 75.8% of the capacity when C-rates as high as 5C were used.

5.2 Results and discussion

5.2.1 Electrochemical performance

The electrochemical performance of the RP-graphite composite prepared using the procedure optimized in Chapter 4 was tested with K via galvanostatic cycling with C-rates ranging from C/20 to 5C. The results are shown in Figure 5.1. The galvanostatic profile of the first cycle shown in Figure 5.1a shows two plateaus. The plateau at about 1.2 V vs K^+/K is related to the degradation of the electrolyte at such potentials and the formation of the SEI. This plateau is not present in the subsequent cycles. The second plateau is centered at about 0.3 V vs K^+/K and, as discussed in Chapter 3, related to the formation of the KP alloy.[4]

The first discharge capacity of the material delivered about $939\,\mathrm{mAh\,g_P^{-1}}$, of which $723\,\mathrm{mAh\,g_P^{-1}}$ was recovered on the first charge, with a total coulombic efficiency on the first cycle of about 77%. The low coulombic efficiency and the higher discharge capacity than the theoretical capacity, suggest the formation of an SEI. When higher currents were applied to the material, it was able to maintain most of the initial capacity (5.1b): using currents as high as 1C, with an overall coulombic efficiency 99.5%. Moreover, it was also able to deliver 86.3% and 75.8% of the initial capacity with currents of 2C and 5C, respectively.

In 5.1c, the differential capacity plots at different C-rates show at what potential the

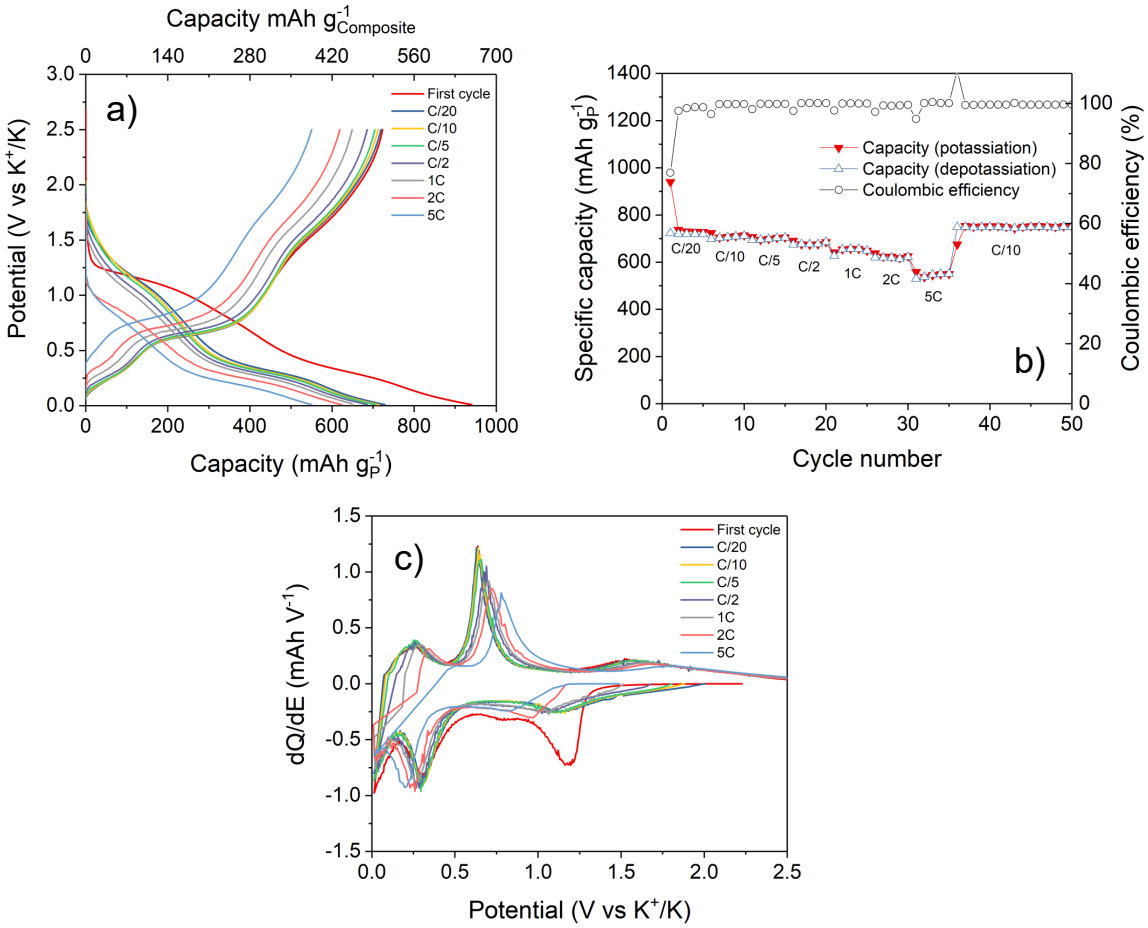


Figure 5.1: Electrochemical performance of RP-C composite. In (a), the galvanostatic profiles of the active material at increasing rates is shown. (b) Shows the rate capability of the material with currents ranging from C/20 to 5C. The differential plots of the cycles shown in (a) are illustrated in (c).

interphases and the alloy are formed. As discussed earlier, a peak at 1.2 V vs K^+/K, associated to the formation of the SEI is visible only on the first cycle. On discharge, a peak at 0.3 V vs K^+/K is visible, related to the formation of the alloy, and on charge a peak at 0.7 V vs K^+/K appears, corresponding to the dealloying of the material. The hysteresis between these two peaks is almost constant when higher currents are applied. However, it suddenly increases when currents as high as 2C are applied. The effect is even more prominent when 5C is applied. This is a consequence of the slow diffusion of the ions in the material, which limits the kinetics of the reaction.[5]

Interestingly, when a current of C/10 is applied again to the cell after 5C, the material

is able to deliver a capacity that is about 3% higher than the initial charge capacity (5.1b).

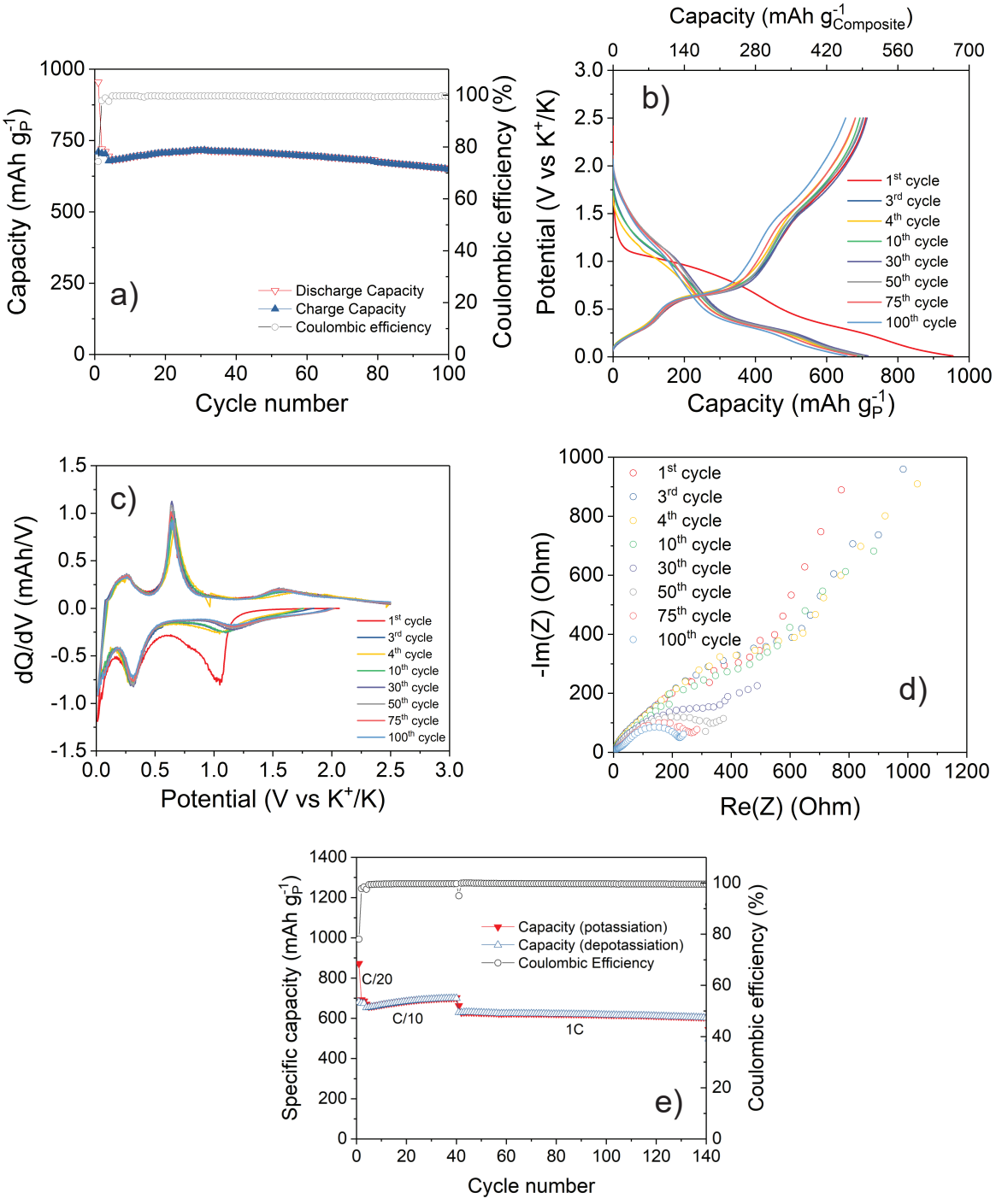


Figure 5.2: a) Composite cycled for the first three cycles at C/20 and the remaining cycles at C/10. b) Galvanostatic profiles and differential plot of the material at different cycles (b and c, respectively). d) Impedance profiles taken after the cycles shown in (b) and (c). e) Cycling stability of the RP-graphite composite at 1C. C/20 rates are applied for the first three cycles, then C/10 rates are applied up until the 30th cycle. a rate of 1C is applied until the 100th cycle.

To accurately study this phenomenon, we cycled the material at C/20 for the first three cycles (to allow the formation of a stable SEI) and at C/10 for 100 cycles to observe changes in the performance. We also measured the impedance of the cell after each cycle, allowing 1 h rest before each measure. The galvanostatic profiles and the cycling data are shown in Figure 5.2. We observed that after the 3rd cycle, the capacity slowly increases and reaches a peak after 30 cycles, where the capacity is 5% higher (715 mAh g_P^{-1}, 30th cycle capacity compared 678 mAh g_P^{-1}, 4th cycle capacity). While the galvanostatic profiles and the position of the plateaus do not show any visible change during cycling (Figure 5.2b,c), the impedance analysis shows that the charge transfer resistance decreases with increasing cycles (Figure 5.2d). This behaviour suggests that the surface area where the electrode material is in contact with the electrolyte is increasing, and so the diffusivity of the ions into the material is increased, improving the performance and increasing the capacity. This could be associated to the formation of cracks on the electrode material caused by the expansion/contraction of RP particles during subsequent cycles.[6] The material is still able to deliver 95% of the capacity after 100 cycles.

We also tested the cycle life of this material at higher rates. The electrode was cycled in similar conditions as before for 40 cycles (first three cycles at C/20 and the following cycles at C/10), then we applied a current of 1C for 100 cycles, shown in Figure 5.2e. Again, an increase in capacity was observed when a current of C/10 was applied. The capacity increased for about 30 cycles, until it stabilized. When a current of 1C was applied, the material delivered a capacity of 629 mah g^{-1} and after 100 cycles it was able to retain 96.3% of the capacity, with a coulombic efficiency of about 99.4% for each cycle (Figure 5.1). No increase of capacity was observed when higher currents were applied.

The long cycle life and the high rate capability of the material are likely related to the initial reduction of the particle/size distribution of the RP that is operated during the first production step. The homogeneous mixing with graphite also contributes to the stability of the material, as shown in Chapter 4.

5.2.2 Material Characterisation

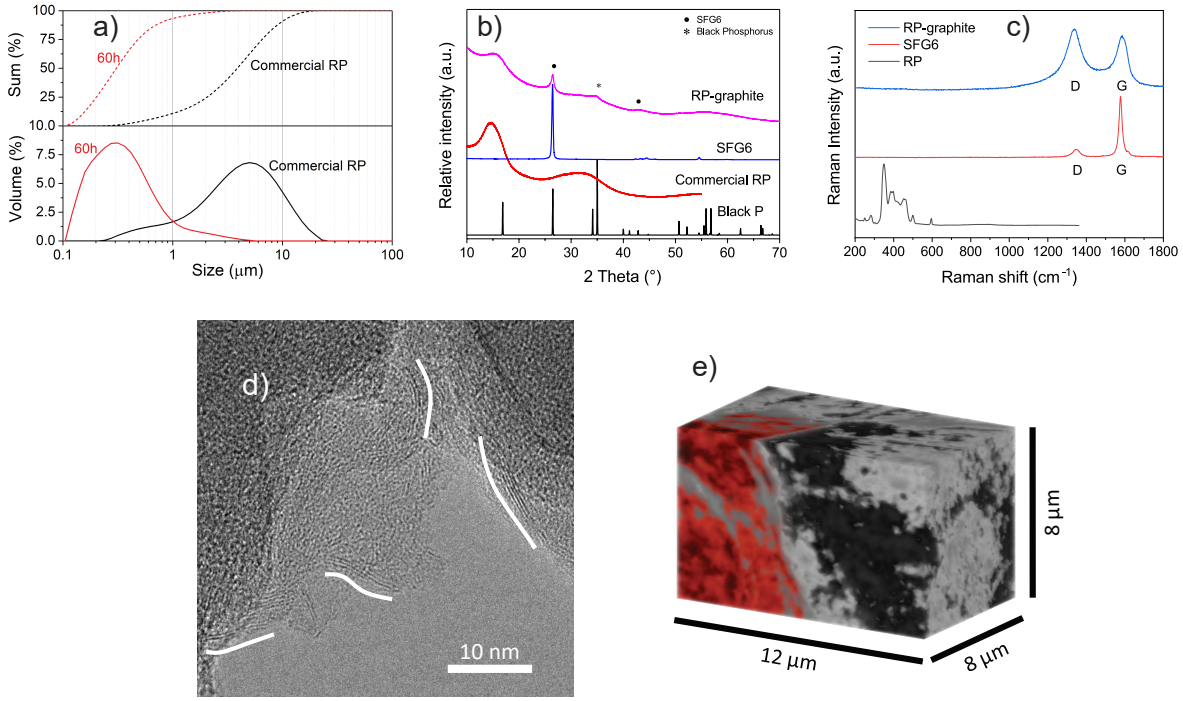


Figure 5.3: a) XRD analysis and (b) Raman spectra of RP, SFG6 and RP-graphite composite. c) Particle size distribution of commercial RP and RP ball milled for 60h. d) TEM of RP/graphite composite. The white lines indicate where the graphite layers are located on the surface of the composite particles. The TEM analysis on the composite was performed by a DPhil student in the group: Albert W. Xiao (University of Oxford). e) Reconstructed section of the PXCT scan of electrode material. The PXCT analysis on the electrode material was performed by a postdoc in the group, Dr. Hyeon Jeong Lee (University of Oxford), at Diamond Light source.

The morphology of this material was thoroughly characterized during the optimisation process that was explained in Chapter 4. DLS, XRD, Raman, TEM and SEM-EDX were used in this work. As shown previously, after ball milling RP in EG for 60h, the particle-size distribution reduces from a Dv90 value of 12.49 µm to 0.79 µm, 5.3a. As explained earlier, EG is used due to its high viscosity and high boiling point that to improve the safety of the process and decrease the energy released from the impact of the balls, which could cause a phase change from RP to BP.[7] This was confirmed by XRD and Raman

analysis, which do not show peaks related to BP after the first step.(Figure 5.3b)

The second step is the dry milling of RP with graphite for 48h to prepare the composite. As discussed in Chapter 4, this second step was conducted with proper care to avoid further reduction of the RP particle-size. After this step, broader and larger graphite XRD peaks can be observed, suggesting that amorphisation of graphite occurred during the milling, as well as a low intensity peak from BP, suggesting that a small fraction of RP converted to BP during this step (Figure 5.3b). The Raman spectrum of the composite shows the characteristic D and G peaks from graphite at about 1337 cm^{-1} and 1586 cm^{-1} respectively.5.3c These peaks are broader than the peaks that can be observed in the pristine graphite, supporting that amorphisation of graphite occurred during the milling. Indeed, this behaviour is well reported in literature.[8] However, no peaks related to RP are visible in the range 300-500 cm^{-1}.[9, 10]. This can be related to the presence of a carbon coating that is covering the RP particles or alternatively to a higher intensity of the graphite peaks compared to RP. The presence of the carbon coating was confirmed by TEM analysis, which showed the presence of graphite layers coating the surface of the particles (Figure 5.3d). As shown in Chapter 4, this layer was found to be about 16 µm by using energy-tuned PES analysis on the composite, Figure 4.12.[3] The morphology of this composite was further investigated using PXCT (details explained in Section 2.2.7) and SEM analysis. An image of the reconstructed section of the RP electrode is shown in Figure 5.3e, where RP is depicted in red, graphite is black and Super P is grey. The brightness of the color is indicative of the electron density (dark color = high density). PXCT shows that P-rich areas are visible in the electrode, as well as C-rich areas. The resolution however is too low to distinguish between the particles and a clear definition of the boundaries of the particles cannot be obtained.

SEM-EDX, on the other hand, allows a better definition of the elemental distribution of P and C in the composite. Figure 5.4 shows that both C and P are homogeneously distributed in the electrode, with some areas where a slightly higher concentration of each elements can be seen.

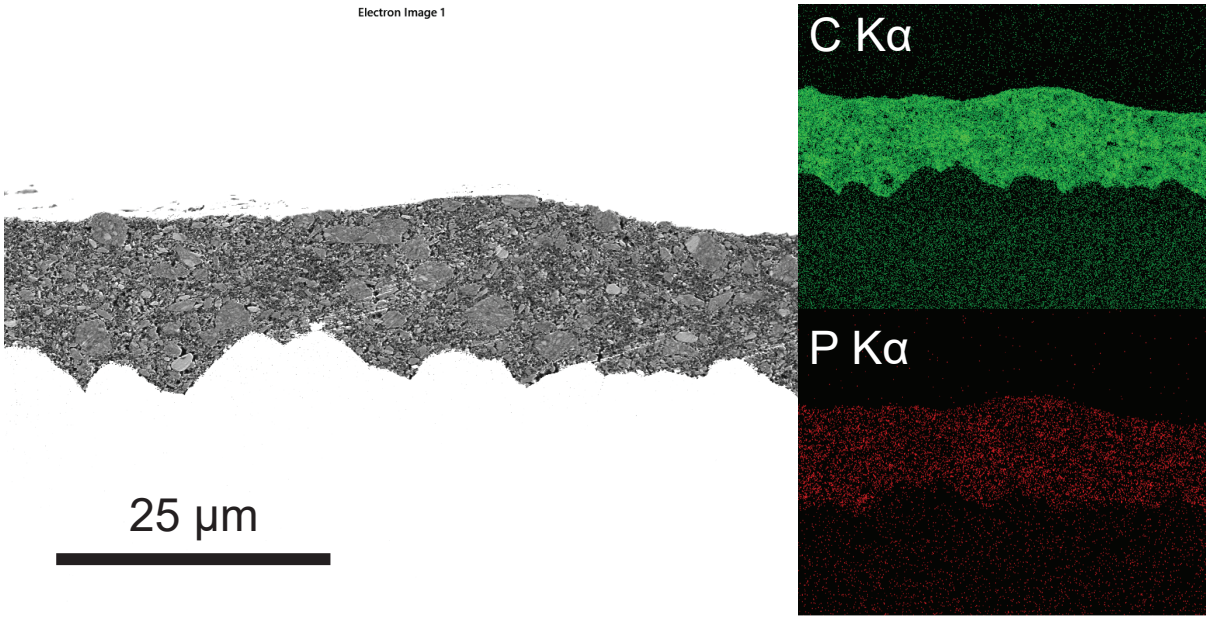


Figure 5.4: Cross section SEM and EDX analysis on RP-graphite electrode with signal map for C and P.

5.2.3 Raman operando

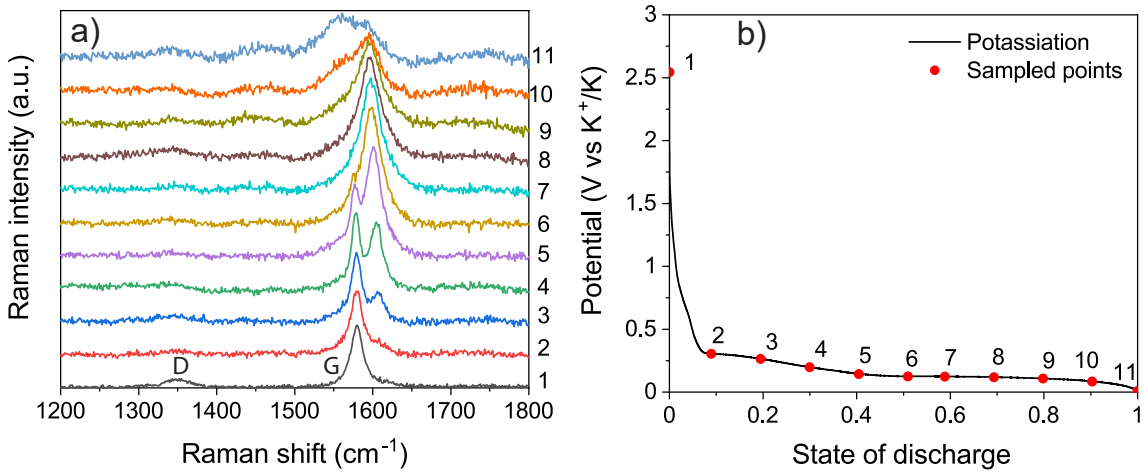


Figure 5.5: a) Raman operando made on a graphite electrode. b) Points in the galvanostatic profile show where the Raman spectrum was taken.

A Raman operando technique was used to observe the structural changes in the composite while alloying and dealloying with K. A 2032 coin cell was modified to allow the sampling of the electrode using Raman spectroscopy. A hole was drilled on the positive

side of the coin cell and a sapphire window was glued using epoxy to ensure a tight seal. Full details about this process are explained in Section 2.2.2. A schematic of the cell is shown in Figure 2.1. As only the graphite peaks are visible in the composite, we focused our attention of the changes that could occur to these peaks while cycling. As a standard, we also performed operando Raman analysis on pristine SFG6. The electrodes of both the composite and the pristine graphite were prepared following the procedure explained in Section 2.1.3. The potassiation of graphite induces structural changes to the material, mostly related to the intercalation of the ion between the graphite layers, which is reported to occur in stages.[11] The G peak undergoes different changes throughout the reaction. When K starts intercalating (about 0.25 V vs K^+/K) a shoulder of the G peak ($1616\,cm^{-1}$), which is visible at higher Raman shift, becomes more intense while the G peak gradually decreases in intensity (Figure 5.5). This behaviour is mainly related to the different stages of intercalation, as reported by Chacon-Torres et al.[12] Interestingly, when the potassiation is complete, both peaks disappear and instead a broad asymmetric band appears at about $1550cm^{-1}$. As suggested by Share et al. this could be related to the interaction between the metallic nature of the KC_8 phase and phonons in the material.[13]

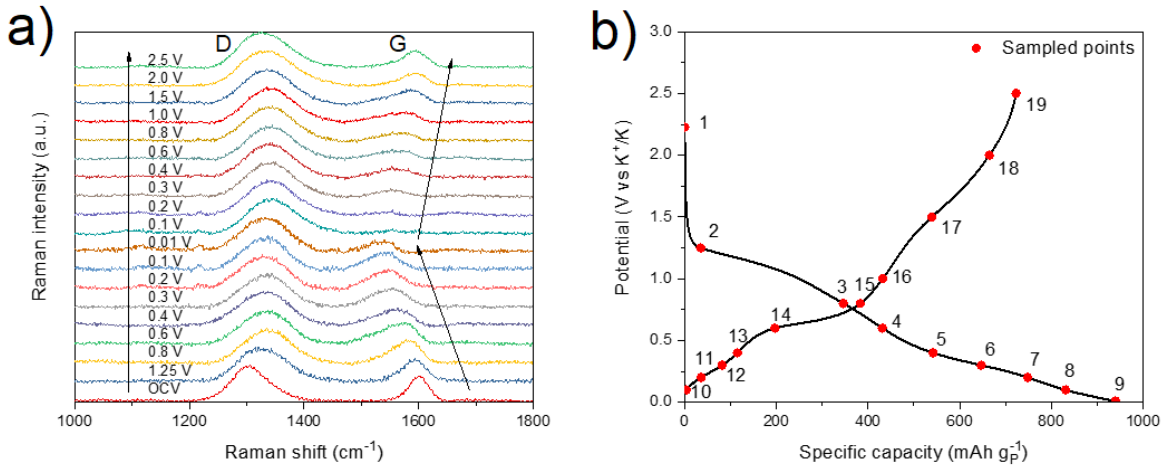


Figure 5.6: a) Raman spectra acquired on the RP-graphite composite at different states of charge. b) Points on the galvanostatic profile of RP-graphite show where the Raman spectra were acquired.

The graphite in the composite, however, shows a completely different behaviour. During potassiation of the composite, the G peak starts shifting to lower Raman shift, until it eventually stops when potassiation is complete. The process is reversible and the peak moves to the initial position when depotassiation is complete (Figure 5.6). The shift of the G peak observed in the composite occurring in the range of potential 0.01 - 2.5 V vs K^+/K suggests that the changes observed could not be entirely related to the chemical reaction between graphite and potassium which, as discussed earlier, occurs below 0.25 V vs K^+/K. Instead, this could be related to structural changes occurring on the graphite during cycling. As suggested by Ni et al., The shift of the G peak can occur when a high strain is applied to graphite layers.[14] They showed that the stretching of graphene layers induces the shift of the G peak to lower Raman shift. In this case, we speculate that the changes that we observe could be caused by a similar event. In the composite, the volume expansion of RP particles could cause the stretching of the graphite layers present on the surface of the particles, causing the shift of the G peak in the whole range of potentials and not only when K is supposed to intercalate in graphite. The dealloying and contraction of RP particles reverses the strain, causing the peak to move back to its original position.

5.2.4 Comparison with literature

The composite material developed shows outstanding performance even when high currents such as 5C are applied. Compared to other anode materials reported for KIBs, it is one of the best performing, both in terms of high capacity and rate capability. In Figure 5.7 a comparison between this material and other common anode materials is presented. To achieve a fair comparison, the electrochemical data have been recalculated based on the total electrode material (mass of P-C composite or active material, carbon additive and binder). The RP-graphite composite is able to deliver $403\,\mathrm{mAh\,g^{-1}_{electrode}}$ when a slow current of $24\,\mathrm{mA\,g^{-1}_{electrode}}$ is applied, and retains 75.8% of the capacity when currents 100 times higher are used. Compared to other P-C composites, it is the

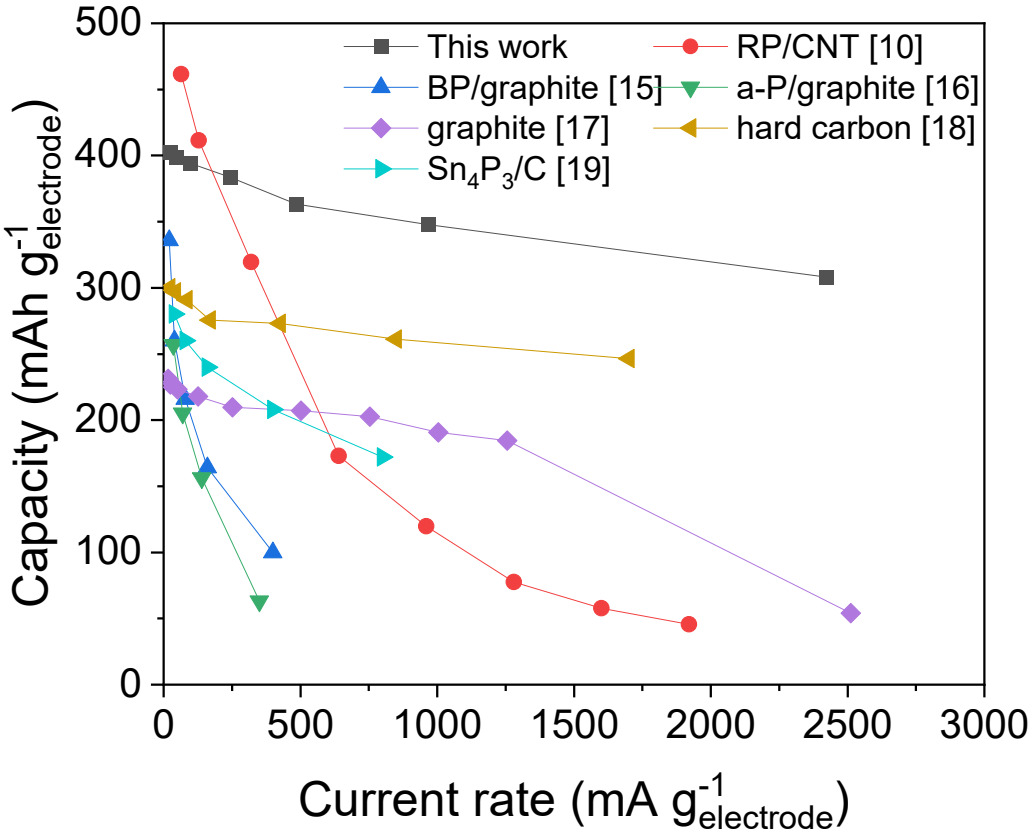


Figure 5.7: Comparison between the performance of the material presented in this work with other anode materials previously reported in literature.[10, 15–19]

only one with such rate capability, showing that the nanosizing of RP particles before the production of the composite is an effective way to obtain high performing electrodes using a simple, easy, scalable and cheap way such as ball milling.

5.3 Conclusions

In this chapter, the performance of the RP-graphite composite developed and optimized in Chapter 4 is presented with K. The material showed one of the best performances previously reported in terms of capacity delivered, cycle life and rate capability. The material delivered 723 mAh g_P^{-1} at C/20 and was able to retain 75.8% of the capacity at 5C. When a current of 1C was used, the material was able to retain 96.3% of the capacity

after 100 cycles with an average coulombic efficiency higher than 99.4%, showing a high cycling stability and long cycle life. Operando Raman analysis performed during cycling showed that the G peak of the graphite reversibly shifts to lower Raman shift during the alloying reaction and moves back to its original position during the dealloying reaction. The expansion/contraction of the RP particles during the potassiation/depotassiation could cause strain on the graphite layers that are present on the RP particles - confirmed by TEM analysis - causing the shift of the G peak. This material achieved one of the best performances reported so far compared to other anode materials previously reported.

5.4 References

1. Komaba, S. *et al.* Potassium intercalation into graphite to realize high-voltage/high-power potassium-ion batteries and potassium-ion capacitors. *Electrochemistry Communications* **60,** 172–175 (2015).

2. Carboni, M. *et al.* Unlocking high capacities of graphite anodes for potassium-ion batteries. *RSC Advances* **9,** 21070–21074 (2019).

3. Capone, I. *et al.* Effect of the Particle-Size Distribution on the Electrochemical Performance of a Red Phosphorus–Carbon Composite Anode for Sodium-Ion Batteries. *Energy & Fuels* **33,** 4651–4658 (2019).

4. Yang, X. X. *et al.* Raman spectroscopic determination of the length, strength, compressibility, Debye temperature, elasticity, and force constant of the C–C bond in graphene. *Nanoscale* **4,** 502–510 (2012).

5. Ovejas, V. J. *et al.* Effects of cycling on lithium-ion battery hysteresis and overvoltage. *Scientific Reports* **9,** 14875 (2019).

6. Ruess, R. *et al.* Influence of NCM Particle Cracking on Kinetics of Lithium-Ion Batteries with Liquid or Solid Electrolyte. *Journal of The Electrochemical Society* **167,** 100532 (2020).

7. Ramireddy, T. *et al.* Phosphorus–carbon nanocomposite anodes for lithium-ion and sodium-ion batteries. *Journal of Materials Chemistry A* **3,** 5572–5584 (2015).

8. Niwase, K. *et al.* Raman Spectra of Graphite and Diamond Mechanically Milled with Agate or Stainless Steel Ball-Mill. *Materials Transactions, JIM* **36,** 282–288 (1995).

9. Durig, J. R. *et al.* On the vibrational spectra and structure of red phosphorus. *Journal of Molecular Structure* **5,** 351–358 (1970).

10. Chang, W. *et al.* Red Phosphorus Potassium-Ion Battery Anodes. *Advanced Science* **6,** 1801354 (2019).

11. Liu, J. *et al.* Unraveling the Potassium Storage Mechanism in Graphite Foam. *Advanced Energy Materials* **9,** 1–11 (2019).

12. Chacón-Torres, J. C. *et al.* Raman spectroscopy of graphite intercalation compounds: Charge transfer, strain, and electron-phonon coupling in graphene layers. *Physica Status Solidi (B) Basic Research* **251,** 2337–2355 (2014).

13. Share, K. *et al.* Mechanism of potassium ion intercalation staging in few layered graphene from in situ Raman spectroscopy. *Nanoscale* **8,** 16435–16439 (2016).

14. Ni, Z. H. *et al.* Uniaxial Strain on Graphene: Raman Spectroscopy Study and Band-Gap Opening. *ACS Nano* **2,** 2301–2305 (2008).

15. Sultana, I. *et al.* High capacity potassium-ion battery anodes based on black phosphorus. *Journal of Materials Chemistry A* **5,** 23506–23512 (2017).

16. Wu, X. *et al.* Enhanced capacity of chemically bonded phosphorus/carbon composite as an anode material for potassium-ion batteries. *Journal of Power Sources* **378,** 460–467 (2018).

17. Hosaka, T. *et al.* Highly concentrated electrolyte solutions for 4 v class potassium-ion batteries. *Chemical Communications* **54,** 8387–8390 (2018).

18. Yamamoto, H. *et al.* Synthesizing higher-capacity hard-carbons from cellulose for Na- and K-ion batteries. *Journal of Materials Chemistry A* **6,** 16844–16848 (2018).

19. Zhang, W. *et al.* Phosphorus-Based Alloy Materials for Advanced Potassium-Ion Battery Anode. *Journal of the American Chemical Society* **139,** 3316–3319 (2017).

Chapter 6

Electrolyte optimization

6.1 Introduction

Previous chapters have been devoted to the study of the mechanical properties of RP-based electrodes at a particle level (Chapter 3) and at the composite level (Chapter 4 and 5). However, as mentioned in Chapter 1, the electrolyte can also play an important role in terms of cyclability of RP/C composites. The electrolyte in a cell is an alkali-ion containing salt that is dissolved in an organic solvent or ionic liquid. Organic solvents are most commonly used, in particular fluorinated solvents, as they allow for a large electrochemical stability window (i.e. they have a better oxidative stability) compared to water (up to 4.5 V compared to 1.23 V).[1–3] Salts, such as hexafluorophosphates (APF_6) or bis(fluorosulfonyl)imides, where A is an alkali metal ion, are used to maintain the charge neutrality in the materials. The electrolyte can influence the performance of the cell in many ways. One of the most important features that are affected by the choice of salts and solvents present in the electrolyte is the SEI that results from to the decomposition products of the electrolyte. This is a passivating layer that forms on the surface of the negative electrode in alkali batteries at low potentials. The formation of this layer between the electrode and the electrolyte can heavily affect the battery performance as it hinders further reactions. For example, its morphology and composition

influences the movement of the ions through the layer, which affects the rate capability of the material.[1] The mechanical and chemical stability of the SEI is another important parameter that heavily impacts the battery performance. A weak SEI can easily break after subsequent cycles, in particular with alloying materials where the volume expansion is severe. This results to new exposed surface of the electrode that can react with the electrolyte to form a new SEI, thus reducing the coulombic efficiency of the cycle. The ideal SEI should be porous, ionically conductive, and mechanically and chemically stable. Additives, such as FEC and vinylene carbonate (VC) are often added to the solvent to tune the composition and the morphology of this layer and increase the performance of the battery.[4]

In this chapter, an overview of the performance of the RP-graphite composite optimized in Chapter 4 with different electrolytes for Li, Na and K is offered. In particular, the electrolytes shown in Table 2.2 have been tested. EC and DEC organic solvents were investigated due to their wide application in LIBs, NIBs and KIBs. [1–3] The effect of FEC additive was studied due to the well reported performance improvements that this additive has shown with phosphorus-based anodes in NIBs.[5] Finally, the effect of hexafluorophosphates salts on phosphorus-graphite composite has been investigated as their use is widely reported in literature. FSI salts were also investigated due to the high solubility of KFSI salt in organic solvents compared to KPF_6, which is only able to reach 0.8 M concentration.

As expected, the performance of the material was affected by the choice of the electrolyte for each alkali ion. These changes are mainly related to the different electrochemical reactions that occur between the electrode surface and the electrolyte. The work presented here opens up the possibility for future studies on the interaction between these electrolytes and RP, in particular the investigation of the SEI that is formed and the optimisation of the electrolyte to further improve the performance of the RP-graphite composite.

6.2 Results and discussion

6.2.1 Electrolytes for LIBs

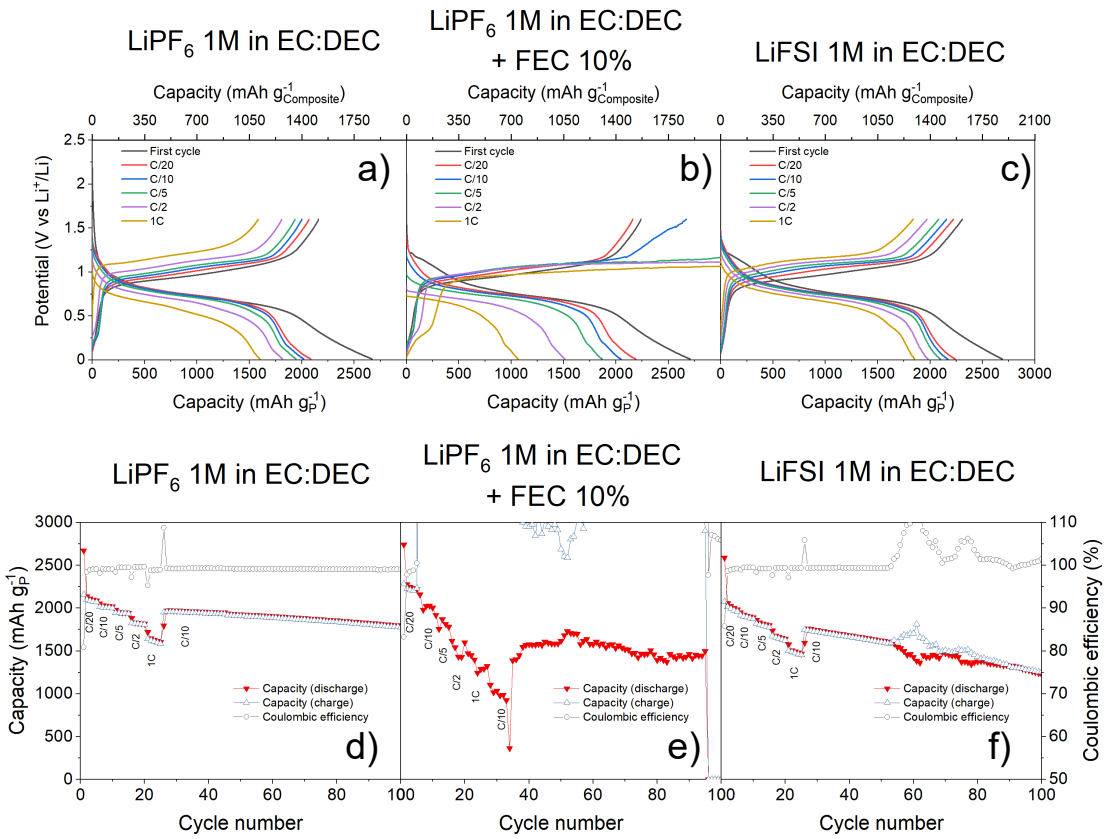


Figure 6.1: a-c) Galvanostatic profiles of the RP-graphite composite cycled at different C-rates with 1M $LiPF_6$ in EC:DEC, 1M $LiPF_6$ in EC:DEC + FEC 10% and 1M LiFSI in EC:DEC, respectively. d-e) Discharge and charge capacity and coulombic efficiency of the RP-graphite composite cycled at different C-rates with 1M $LiPF_6$ in EC:DEC, 1M $LiPF_6$ in EC:DEC + FEC 10% and 1M LiFSI in EC:DEC, respectively.

The electrochemical performance of the RP-graphite composite, optimized in Chapter 4, was evaluated using three different electrolytes. The results are shown in Figure 6.1. The galvanostatic profiles of the composite show a plateau centered at about 0.9 V vs Li^+/Li (Figure 6.1a-c), related to the formation of the Li_3P phase, as previously mentioned in Chapter 3. The composite tested with 1M $LiPF_6$ in EC:DEC shows the best performance (Figure 6.1d). The material delivers a capacity of 2159 $mAh\,g_P^{-1}$ at C/20 with a first cycle coulombic efficiency of about 80.8%, and it is able to still deliver most

of the capacity at C/5. When higher rates of C/2 are used, the material delivers 87% of the capacity, while it delivers 1647 mAh g_P^{-1} with 1C rates. The capacity, however, gradually decreases over each cycle, likely due to the low conductivity of the material. Nevertheless, the material is able to deliver full capacity when a slower rate of C/10 is applied again, and is able to retain 91% of the capacity at the 100th cycle. The capacity retention was calculated by comparing the charge capacity of the 100th cycle with the charge capacity of the first cycle at C/10, after the application of high rates of 1C. The addition of FEC to the electrolyte provokes totally different results, Figure 6.1e. Despite the high capacity on the first cycle (2280 mAh g_P^{-1}) with a slightly better coulombic efficiency of 83.2%, after only three cycles, the charge capacity of the material (dealloying reaction) results to be higher than the discharge capacity (efficiency > 100%). This phenomenon is in disagreement with previous reports where it was claimed that the addition of FEC in the electrolyte improved the performance of the electrochemical performance of Si.[6] It is possible that by-products of the degradation of the electrolyte are oxidised during charge.[4] However, to confirm if this is the case, more study of the SEI and the degradation of the electrolyte is needed. The use of 1M LiFSI as the salt leads to interesting results. The capacity delivered on the first charge is higher than the other two cases (2307 mAh g_P^{-1}), as well as the coulombic efficiency (85%), as shown in Figure 6.1f. However, the capacity fading is more severe, and only the 81% of the capacity is retained after 100 cycles. Moreover, at cycle 50, an effect similar to the one observed with the electrolyte containing FEC is produced. As previously explained, however, more study is needed to understand the reasons behind this behaviour.

6.2.2 Electrolytes for NIBs

The RP-graphite composite with Na-containing electrolytes shows a distinct plateau located at about 0.4 V vs Na/Na, related to the formation of the fully sodiated phase Na_3P, Figure 6.2a-c. On the first cycle, all profiles show a slope at about 1 V vs Na/Na related to the reduction of the electrolyte and the formation of the SEI. The electrolyte $NaPF_6$

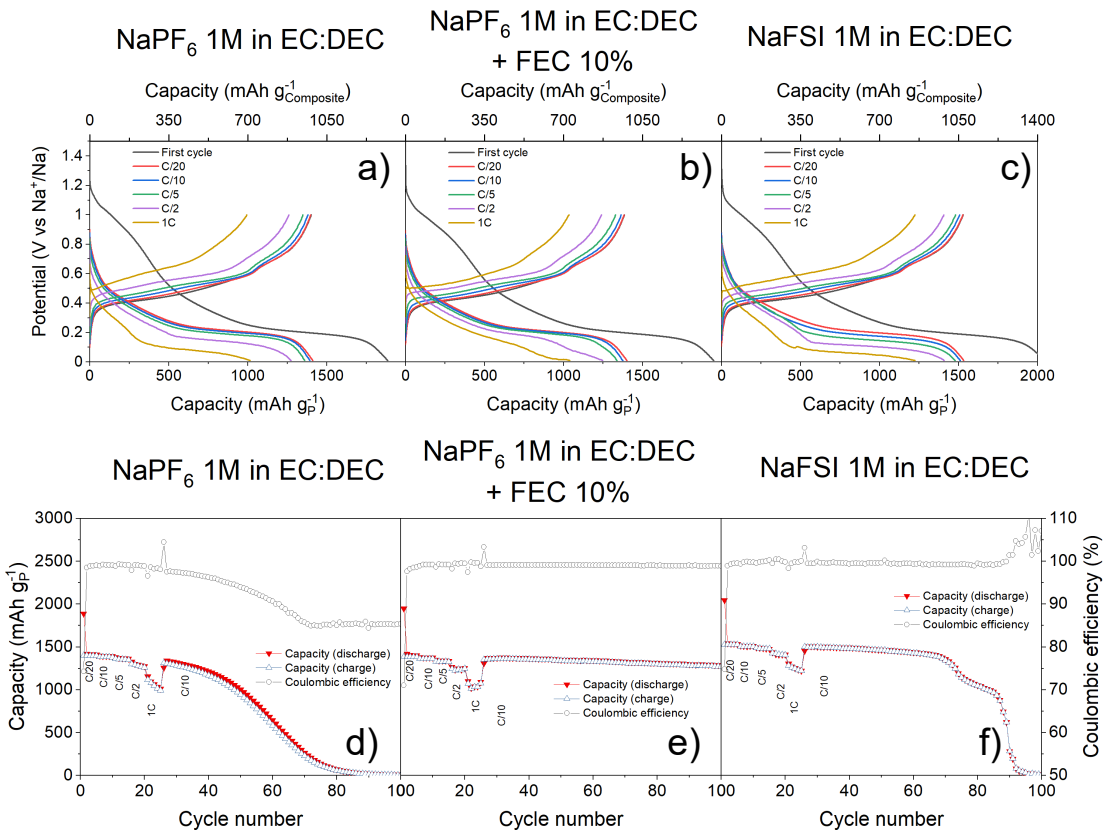


Figure 6.2: a-c) Galvanostatic profiles of the RP-graphite composite cycled at different C-rates with 1M $NaPF_6$ in EC:DEC, 1M $NaPF_6$ in EC:DEC + FEC 10% and 1M NaFSI in EC:DEC, respectively. d-e) Discharge and charge capacity and coulombic efficiency of the RP-graphite composite cycled at different C-rates with 1M $NaPF_6$ in EC:DEC, 1M $NaPF_6$ in EC:DEC + FEC 10% and 1M NaFSI in EC:DEC, respectively.

1M in EC:DEC results in the material delivering a first charge capacity of 1401 mAh g_P^{-1}, with a coulombic efficiency of about 74%. The lower capacity of the composite with Na compared to Li could be related to the contribution of Li intercalation in graphite, which does not occur with Na.[7] Moreover, the lower coulombic efficiency could be related to the larger volume expansion of RP with Na (168% and 332% with Li and Na, respectively, see Appendix D) that results in a larger surface area of RP that has to be covered by the SEI. Despite a good rate capability at C/2 (89.9% of the initial capacity), at 1C the capacity gradually decreases possibly related to the conductivity of the material. When a C/10 rate is applied again, the material delivers full capacity, but it rapidly fades and eventually reaches near zero on the 80th cycle. This is likely related to the low mechanical

stability of the SEI, which needs to be reconstructed at every cycle. This is supported by the low coulombic efficiency for each cycle that gradually decreases until it gets to as low as 85%. The addition of FEC greatly improves the performance. The capacity on the first cycle is about 1385 $\mathrm{mAh\,g_P^{-1}}$, with a coulombic efficiency of 71%. When currents as high as 2C are used, 90% of the capacity is retained, while only 77% of the capacity is delivered with 1C rates. When C/10 rates are applied again, full capacity is delivered and 94% is retained at the 100th cycle, with an average coulombic efficiency of 99.8%. As explained by Dahbi et al., the reason behind the improved performance of the composite is related to the addition of FEC to the electrolyte, which leads to the formation of a more stable, F-rich SEI, compared to the more F-poor SEI that is formed without the FEC.[5]

The composite exhibits interesting performance when 1M NaFSI is used instead of $NaPF_6$, Figure 6.2f. First cycle capacity delivered is about 1529 $\mathrm{mAh\,g_P^{-1}}$, with a coulombic efficiency of about 75%, both higher than the values obtained from using the previous electrolytes. The rate capability of the material is also greatly improved, with 91% of the capacity delivered when C/2 rates are used and 80% of the capacity with 1C is applied. Moreover, the material is able to recover full capacity when C/10 rates are applied again after 1C, and 95% of the capacity is retained for 30 cycles with an average coulombic efficiency of 99.5%. Nevertheless, the capacity decreases rapidly after 60 cycles and reaches zero after 90 cycles. The causes behind this behaviour could be related to the formation of a poorly conductive SEI on the electrode, that leads to its insulation and to a low cycle life. Again, more in-depth studies are needed to study the causes of this behaviour.

6.2.3 Electrolytes for KIBs

KPF_6 salt can only dissolve in EC:DEC up to 0.8 M concentrations.[8] In this work a concentration of 0.7 M was used to avoid the possibility of recrystallisation of the salt in the electrolyte that could occur with changes in solubility related to slight temperature fluctuations during the electrochemical test. Using of this electrolyte allows the RP-

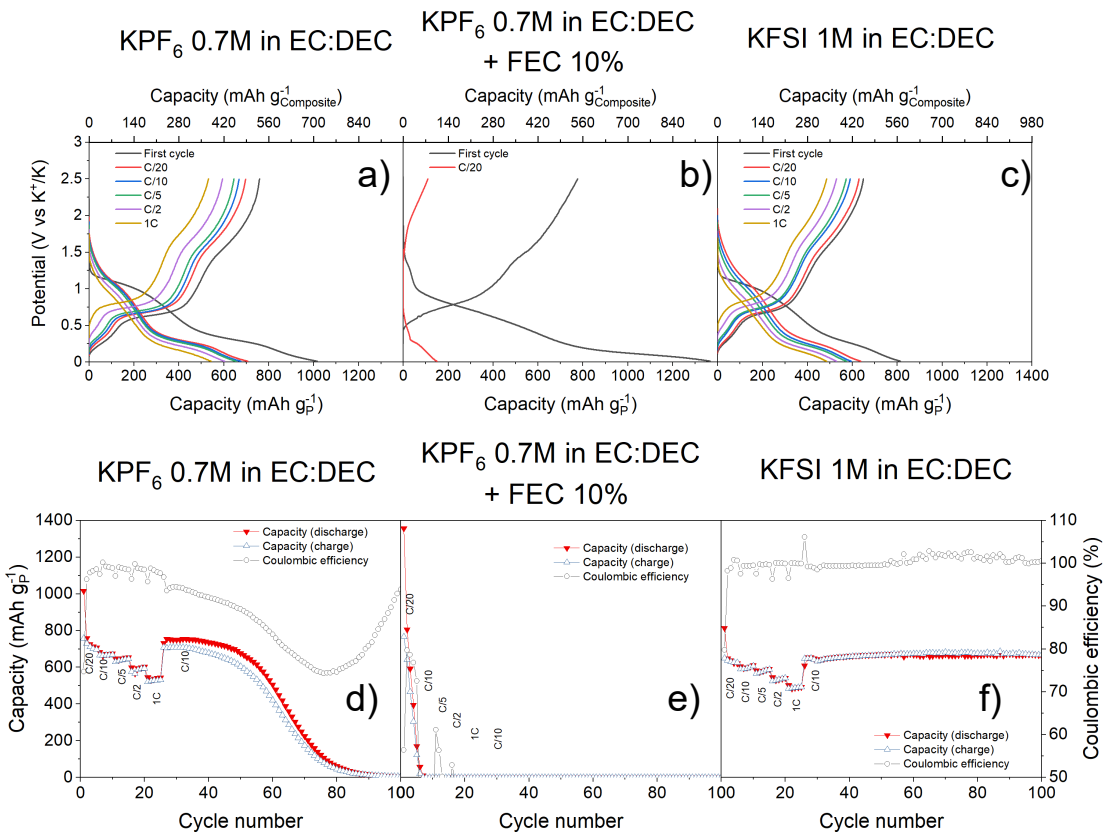


Figure 6.3: a-c) Galvanostatic profiles of the RP-graphite composite cycled at different C-rates with 0.7 M KPF_6 in EC:DEC, 0.7 M KPF_6 in EC:DEC + FEC 10% and 1M KFSI in EC:DEC, respectively. d-e) Discharge and charge capacity and coulombic efficiency of the RP-graphite composite cycled at different C-rates with 0.7 M KPF_6 in EC:DEC, 0.7 M KPF_6 in EC:DEC + FEC 10% and 1M KFSI in EC:DEC, respectively.

graphite composite to deliver about 759 mAh g_P^{-1} on the first charge at C/20 with a first cycle coulombic efficiency of 74.6%. The composite is still able to deliver about 75% of the capacity when high rates of 1C are applied, with an average coulombic efficiency of about 98%. However, the coulombic efficiency greatly decreases with cycling, reaching values as low as 74%. The capacity also gradually decreases over time, reaching almost zero after 80 cycles. This behaviour is likely related to a poorly stable SEI formed on the material, as suggested by the low coulombic efficiency at each cycle.

The lowest cycle life, however, is obtained when FEC is added to the electrolyte. Opposite to what occurs with Na, the addition of FEC results in poor performance of the material, resulting in an extremely low cycle life. This phenomenon has been observed not

only with RP, but also with graphite or MoS_2.[8, 9] As suggested by Xie et al., the addition of FEC can increase the desolvation energy of K^+ ions in the electrolyte, hindering the diffusion of the ions.[9] Moreover, the addition of FEC also results in the formation of a thick and heterogeneous SEI that could reduce the cyclability of the material.

The composite shows the best performance in terms of cycle life when 1M KFSI is used as the salt. The capacity delivered on the first cycle is about $649\,\mathrm{mAh\,g_P^{-1}}$, with a coulombic efficiency on the first cycle of about 80%. The material also shows good rate capability, being able to deliver 75% of the capacity with 1C rates, with an average coulombic efficiency of 99.4%. Moreover, after more than 70 cycles at C/10, the material retained about 99.7% of the capacity, showing an outstanding capacity retention. This behaviour, compared to the previous electrolytes, is likely related to the stability of the SEI that is formed on the material during the first cycle. As shown by Deng et al, the superior performance obtained with the use of KFSI as the salt could be related to the formation of a KF-rich SEI compared to KPF_6, which mainly consists of the decomposition products of the organic solvents.[8, 9]. Also, the repeated expansion/contraction of RP can induce the formation of cracks on the SEI layer that could not be effectively repaired by the decomposition of KPF_6. However, more study is necessary to confirm the composition of the SEI that forms on the composite.

6.3 Conclusions

The appropriate choice of electrolyte can result in improved performance and increased cycle life of the electrode material, mostly due to the nature of the SEI layer that is formed on the surface of the active material. In this chapter, several electrolytes have been tested to study their effect on the cyclability of the RP-graphite composite optimized in Chapter 4. With Li, the material showed the best performance with the electrolyte 1M $LiPF_6$ in EC:DEC. With this electrolyte, the material not only demonstrated good rate capability, but also improved cycle life, retaining 91% of the capacity after 70 cycles

at C/10. On the other hand, the addition of FEC to the electrolyte resulted in poor performance, with unusual high capacity during charge. This behaviour is surprising, as Markevich et al. not only showed that this phenomenon occurs when FEC is not present in the electrolyte, but it can be solved by the addition of FEC.[6] The reason why this occurs is not clear, however the results suggest that degradation products from the reduction of the electrolyte might be oxidized during charge. This can be elucidated with further study of the SEI (with XPS) or the investigation of the presence of soluble degradation compounds in the electrolyte, via gas chromatography coupled with mass spectrometry. Ultimately, the electrolyte containing LiFSI 1M in EC:DEC also showed poor performance, with similar behaviour. A similar investigation is therefore required. The electrolyte containing $NaPF_6$ 1M in EC:DEC with the addition of FEC resulted in the best performance delivered by the composite with Na. This result was expected, as Dahbi et al. showed that the lack of FEC results in the poor stability of the SEI on the electrode material, leading to poor coulombic efficiency and cycle life.[5] Although the use of NaFSI instead of $NaPF_6$ leads to higher capacity and first cycle coulombic efficiency compared to the other two electrolytes, the cycle life is rather poor, with the capacity dropping after only 60 cycles. KFSI 1M in EC:DEC allows for the best performance of the composite with K. The material delivered high capacity, good rate capability and high first cycle coulombic efficiency, together with a very long cycle life. The use of KPF_6 resulted in very poor performance, mostly related to the weak nature of the SEI that is formed on the electrode, implied by the low coulombic efficiency of each cycle. This results however needs to be confirmed by further analysis. On the other hand, the addition of FEC, that solves this issue with Na, worsens the performance of the composite, with a very low cycle life. As suggested by Xie et al., this is related to the high solvation energy of the FEC and the electrolyte with the alkali ion.[9] This work shows that the components of the electrolyte need to be optimized for each alkali ion. In particular, more in-depth study (for example with the employment of surface techniques such as XPS) is still needed to understand the morphology and the properties of the SEI

that is formed on the electrode and how this influences the electrochemical properties of the material. This research can be the ideal focus for future work on the optimisation of this anode material.

6.4 References

1. Li, Q. *et al.* Progress in electrolytes for rechargeable Li-based batteries and beyond. *Green Energy & Environment* **1,** 18–42 (2016).
2. Ponrouch, A. *et al.* Non-aqueous electrolytes for sodium-ion batteries. *Journal of Materials Chemistry A* **3,** 22–42 (2015).
3. Hosaka, T. *et al.* Highly concentrated electrolyte solutions for 4 V class potassium-ion batteries. *Chemical Communications* **54,** 8387–8390 (2018).
4. Haregewoin, A. M. *et al.* Electrolyte additives for lithium ion battery electrodes: progress and perspectives. *Energy Environ. Sci.* **9,** 1955–1988 (2016).
5. Dahbi, M. *et al.* Black Phosphorus as a High-Capacity, High-Capability Negative Electrode for Sodium-Ion Batteries: Investigation of the Electrode/Electrolyte Interface. *Chemistry of Materials* **28,** 1625–1635 (2016).
6. Markevich, E. *et al.* Fluoroethylene Carbonate as an Important Component for the Formation of an Effective Solid Electrolyte Interphase on Anodes and Cathodes for Advanced Li-Ion Batteries. *ACS Energy Letters* **2,** 1337–1345 (2017).
7. Moriwake, H. *et al.* Why is sodium-intercalated graphite unstable? *RSC Advances* **7,** 36550–36554 (2017).
8. Deng, L. *et al.* Influence of KPF_6 and KFSI on the Performance of Anode Materials for Potassium-Ion Batteries: A Case Study of MoS_2. *ACS Applied Materials & Interfaces* **11,** 22449–22456 (2019).

9. Xie, J. *et al.* Recent progress of electrode materials cooperated with potassium bis(fluorosulfonyl)imide–containing electrolyte for K-ion batteries. *Materials Today Advances* **6,** 100035 (2020).

Conclusions and Future work

Key Findings and implications for the field

This DPhil work has been devoted to the study of the mechanical and electrochemical properties of RP and their effect on the cyclability of the material as an anode for Li, Na and K-ion batteries.

In Chapter 3, a model that simulated the volume expansion of RP particles during the alloying reaction has been presented. The development and use of this model required the measurement for the first time of the mechanical properties (elastic and plastic) of RP and the diffusivity of the alkali ions in the material. The mechanical properties were measured by using compression tests and in-situ nanoindentation. Properties such as bulk modulus, elastic modulus, Poisson's ratio and fracture toughness were successfully measured and used to calculate other mechanical properties, in order to provide, for the first time, a collection of data related to RP. This allowed us to classify RP as a ceramic, similar to Si, but capable of withstanding higher strains without catastrophic failure. The diffusivity of the ions was measured by GITT analysis, which showed that, while Li and Na follow a similar trend, possibly related to a similar reaction path, K diffusivity shows sharper changes, most likely related to the formation of intermediate phases. The application of these values in the model showed that, among the three alkali ions, K is the one that causes the larger stresses on the RP particle during the alloying reaction. Moreover, the size of the particle that could cause the plastic failure of the material decreases when increasing currents are used. This plastic failure, though, does not cause

the fracture of the particle, as a pre-existing crack or flaw in the material of about 160 nm is required to cause it. This finding removes the fracture of the particle as one of the causes that could lead to the low cyclability of the material (as occurs with Si), and allows to focus on other matters such as the optimisation of the surface area-to-volume ratio, electronic conductivity of the material, RP/C composite ratios and microstructure of the electrode.

For this reason, in Chapter 4, the effect of the particle-size distribution on the electrochemical performance of a RP-graphite composite is evaluated. The particle-size distribution of RP was reduced and controlled using wet milling with EG. The use of EG greatly improves the efficiency of the milling. Three particle-size distributions with an evenly spaced Dv90 value of 1.85, 1.26 and 0.79 µm were used to produce a RP-graphite composite that was prepared by ball milling the two components for 24h. The composite was tested with Na, as it produces the largest volume expansion on the RP. Also, Na does not intercalate in graphite allowing its use as carbon additive in the composite, allowing the investigation of the effect of the RP particle-size distribution alone, without the contribution of the carbon to the electrochemical performance of the composite. The composite prepared with the largest particles resulted in a material with a low cycle life, losing most of its capacity after only 20 cycles. This is mainly due to the repeated volume expansion/contraction of RP when cycling, which could cause the failure of the electrode material and loss of electrical contact with the current collector. The use of RP with a smaller particle-size distribution produced composites with improved cycle life. In particular, the composite prepared with the smallest particle-size distribution resulted in a material with long cycle life and the highest capacity among the three. The RP with this particle-size distribution was also used to test the effect of the milling time of RP with graphite on the performance of the electrode material. The results showed that after 1 h milling time the elements are still heterogeneously mixed in the electrode and the result is an electrode with poor cycle life. After 24 h, the distribution of the elements in the electrode is more homogeneous and the elements get more evenly distributed after 48h.

This last material, in particular, showed superior performance with a capacity retention after 100 cycles of 88%.

In Chapter 5, the composite optimized as explained in Chapter 4 was tested with potassium to study its electrochemical performance with another alkali metal. The material showed high performance, being able to deliver 723 $\mathrm{mAh\,g_P^{-1}}$ and retaining 75.8% of the capacity even when currents rates as high as 5C were used. This material, compared to previously reported anodes (carbon-based and phosphorus-based) is one of the best performing, both in terms of capacity and rate capability.

In Chapter 6, different electrolytes for Li, Na and K were tested to study their effect on the electrochemical performance of the RP-graphite composite optimized in Chapter 4. For Li, the electrolyte 1M $LiPF_6$ in EC:DEC showed the best performance, while the addition of FEC or the replacement of $LiPF_6$ with LiFSI showed poor performance. For Na, the best performing electrolyte was 1M $NaPF_6$ in EC:DEC with 10% FEC, while the other two electrolytes showed poor performance. This is most likely related to the composition and the mechanical properties of the SEI that results from the degradation of that electrolyte compared to the other two. 1M KFSI in EC:DEC is the best performing electrolyte for K, while the use of 0.7M KPF_6 in EC:DEC (with or without FEC) results in poor performance, related to the composition of the SEI (KF-poor) or to the high solvation energy with K. The optimisation of the electrolyte, however, necessitates further study in order to characterize and understand what solvents, salts or additives effectively improve the performance and how the SEI influences the cyclability of the material.

Future work

One of the key questions that still remain to answer is the reaction path that RP follows during the alloying and dealloying reaction with Li, Na and K. Although the sodiation and the desodiation processes have been discussed by Sottmann et al. and Marbella et al., and the reaction path of Li, Na and K with K predicted by Mayo et. al and Yang

et al., clear evidence of the real reaction path with Li and K is still missing.[1–4] In particular, it would be interesting to understand if intermediates are formed during the reaction, if a phase change occurs and if the intermediates are crystalline or amorphous. A way to answer this question would be the employment of operando XRD experiments that follow the reaction during the alloying and de-alloying steps and that can confirm if the intermediates are crystalline or amorphous. NMR operando experiments can also help to understand the structural changes that occur to RP while the reaction progresses, providing more information about the reaction path. A more practical field of research could be the development and optimisation of cheap and scalable anode material that could promote the production of cells (LIBs, NIBs or KIBs) with an improved energy density at a lower cost. RP, as mentioned earlier, is the only alloying material that is able to electrochemically alloy with Li, Na and K developing a very high capacity. In Chapter 4, a RP-graphite composite was produced to study the effect of the particle-size distribution of RP with Na, where graphite was chosen due to its inability to intercalate Na. Further optimisation of the composite material, however, is still required. The P/C ratio for example needs to be accurately tuned in order to increase the amount of P in the composite (thus increasing the capacity of the composite) while ensuring the electronic conductivity throughout the material with the lowest amount of C. A preliminary study concerning this parameter was developed by Kim et al., but a deeper is necessary.[5]. Moreover, an investigation on the optimal carbon additive to be used in the RP/C composite is required. The ideal carbon not only ensures the electronic conductivity through the composite, but also contributes to the capacity. In Chapter 6, a brief study of the effect of different electrolytes on the electrochemical performance of the RP-graphite composite is given. However, more study is needed not only to understand the products that are formed with the degradation of the electrolytes and their effect on the anode material, but also further tests with different solvents (e.g. DMC or PC or ionic liquids) as well as additives (such as VC). XPS analysis of post-mortem or discharged electrodes, for example, could be employed systematically to understand the nature of

the SEI and how it affects the overall performance. This study could further improve the electrochemical performance of this material and push for its employment in commercial batteries. I hope the work I conducted in my DPhil and the results presented will be of relevance for future studies and applications on this promising and worth pursuing material.

Appendices

A Diffusivity values

In the following table the diffusivity values calculated from the GITT measurements using Equation (2.24) are shown.

LITHIUM		SODIUM		POTASSIUM	
S.O.C.	D (cm^2 s^{-1})	S.O.C.	D (cm^2 s^{-1})	S.O.C.	D (cm^2 s^{-1})
0.007	1.92E-16	0.01	5.41E-16	0.01	4.79E-16
0.027	3.94E-16	0.05	1.83E-15	0.04	7.39E-16
0.056	9.32E-16	0.11	2.81E-15	0.07	8.10E-16
0.084	1.17E-15	0.17	3.00E-15	0.10	6.90E-16
0.11	1.27E-15	0.22	2.60E-15	0.13	5.93E-16
0.14	1.29E-15	0.28	1.49E-15	0.15	5.88E-16
0.17	1.15E-15	0.34	1.03E-15	0.18	6.38E-16
0.20	7.78E-16	0.40	9.73E-16	0.21	6.76E-16
0.22	6.36E-16	0.45	8.68E-16	0.24	7.39E-16
0.25	5.19E-16	0.51	9.76E-16	0.26	9.40E-16
0.28	4.20E-16	0.57	7.30E-16	0.29	1.34E-15
0.31	3.50E-16	0.63	5.75E-16	0.32	1.79E-15
0.34	3.00E-16	0.68	4.70E-16	0.35	2.03E-15
0.36	2.70E-16	0.74	3.37E-16	0.38	2.01E-15

0.39	2.42E-16	0.80	2.32E-16	0.40	1.71E-15
0.42	2.36E-16	0.86	1.85E-16	0.43	1.01E-15
0.45	2.19E-16	0.91	1.65E-16	0.46	6.13E-16
0.48	2.23E-16	0.97	2.71E-16	0.49	3.83E-16
0.51	2.11E-16			0.52	2.63E-16
0.53	1.91E-16			0.54	1.52E-16
0.56	1.74E-16			0.57	1.09E-16
0.59	1.59E-16			0.60	6.52E-17
0.62	1.44E-16			0.63	6.39E-17
0.65	1.39E-16			0.66	4.53E-17
0.68	1.28E-16			0.68	4.04E-17
0.70	1.32E-16			0.71	4.92E-17
0.73	1.32E-16			0.74	6.83E-17
0.76	1.49E-16			0.77	1.03E-16
0.79	1.65E-16			0.79	2.08E-16
0.82	1.79E-16			0.82	3.73E-16
0.85	1.91E-16			0.85	5.58E-16
0.87	2.01E-16			0.88	7.03E-16
0.90	2.48E-16			0.91	6.70E-16
0.93	4.48E-16			0.93	6.22E-16
0.95	8.12E-16			0.96	7.00E-16
0.98	1.24E-15			0.99	1.03E-15

Table 1: Diffusivity values of different alloying states of RP with Li, Na and K.

B RP density

The density of RP was measured using a OHAUS Pioneer Density Kit. Ethanol was used as the solvent. The density of empty vials was measured prior to the addition of the sample. Then, the density of RP was calculated using the following equation:

$$\rho(\mathrm{RP}) = \frac{\mathrm{m(RP)_{air}}}{\mathrm{m(RP)_{air}} - \mathrm{m(RP)_{ethanol}}} \times [\rho(\mathrm{ethanol}) - \rho(\mathrm{air})] + \rho(\mathrm{air})$$

where $\mathrm{m(RP)_{air}}$ and $\mathrm{m(RP)_{ethanol}}$ are the mass of RP samples in air and in ethanol, respectively. In order to get these values, the mass of the vials containing the powder was measured before the addition of the sample to obtain their mass in air and in ethanol. The mass of RP in air and ethanol was simply calculated using the following equations:

$$\mathrm{m(RP)_{air}} = \mathrm{m(RP + vial)_{air}} - \mathrm{m(vial)_{air}}$$

$$\mathrm{m(RP)_{ethanol}} = \mathrm{m(RP + vial)_{ethanol}} - \mathrm{m(vial)_{ethanol}}$$

		m(VIAL)	m(VIAL + RP)	m(RP)	DENSITY
SAMPLE_01	AIR	6.643 g	7.045 g	0.402 g	2.60382 g cm^{-3}
	ETHANOL	4.379 g	4.659 g	0.280 g	
SAMPLE_02	AIR	6.569 g	7.126 g	0.557 g	2.16842 g cm^{-3}
	ETHANOL	4.328 g	4.682 g	0.354 g	
SAMPLE_03	AIR	6.659 g	7.108 g	0.449 g	2.16366 g cm^{-3}
	ETHANOL	4.387 g	4.672 g	0.285 g	
SAMPLE_04	AIR	6.609 g	6.851 g	0.242 g	2.39050 g cm^{-3}
	ETHANOL	4.346 g	4.508 g	0.162 g	

Table 2: Density measures on RP

$\rho(\mathrm{air}) = 0.0012$ g cm^{-3}

$\rho(\mathrm{ethanol}) = 0.79105$ g cm^{-3}

Average $\rho(\mathrm{RP}) = 2.33 \pm 0.21$ g cm^{-3}

C Parameters used in the model

Table 3: Parameters in the simulation.

Descriptions	Units	Li	Na	K
Max. concentration	$\mathrm{mol\,cm^{-3}}$	8.46×10^{-2}	5.26×10^{-2}	2.88×10^{-2}
Partial molar volume	$\mathrm{cm^3\,mol^{-1}}$	7.44	14.66	21.53
Li-ion diffusivity	$\mathrm{cm^2\,s^{-1}}$	5×10^{-16}		
Young's modulus	GPa	2.3		

D RP volume expansion

We calculated the expected volume expansion of RP alloying with lithium, sodium and potassium. Starting from the density of RP and using the density of the phases that are formed during the reaction, we fix the moles of P atoms (1) and then we calculate the volume that the new phases would have, compared to the RP. This way, we are able to establish a linear correlation between the volume expansion and the amount of alkali ions that reacted with RP. The density data for RP-metal alloys were taken from https://materialsproject.org/.

Li-RP alloying

Phase	Li/P ratio	Density (g cm^{-3})	Molar weight (g mol^{-1})	Mass for 1 mol of P (g)	Volume for 1 mol of P (cm^3)	Normalized volume	Relative volume expansion (%)
RP	0	2.33	30.97	30.97	13.24	1	0
LiP_7	0.143	2.16	223.76	31.96	14.80	1.12	11.82
Li_3P_7	0.428	1.98	237.64	33.95	17.15	1.30	29.55
LiP	1	2.00	37.91	37.91	18.96	1.43	43.22
Li_3P	3	1.46	51.8	51.8	35.48	2.68	168.07

Table 4: Relative volume expansion of Li-P alloys to RP

Na-RP alloying

Phase	Na/P ratio	Density (g cm^{-3})	Molar weight (g mol^{-1})	Mass for 1 mol of P (g)	Volume for 1 mol of P (cm^3)	Normalized volume	Relative volume expansion (%)
RP	0	2.33	30.97	30.97	13.24	1	0
Na_3P_{11}	0.273	2.046	409.68	37.24	18.20	1.38	37.54
NaP	1	2.052	53.96	53.96	26.30	1.99	98.69
Na_3P	3	1.752	99.94	99.94	57.04	4.31	331

Table 5: Relative volume expansion of Na-P alloys to RP

K-RP alloying

Phase	K/P ratio	Density (g cm^{-3})	Molar weight (g mol^{-1})	Mass for 1 mol of P (g)	Volume for 1 mol of P (cm^3)	Normalized volume	Relative volume expansion (%)
RP	0	2.33	30.97	30.97	13.24	1	0
K_3P_{11}	0.273	1.872	458.01	41.64	22.24	1.68	68.05
K_2P_3	0.666	1.915	171.12	57.04	29.79	2.25	125
KP	1	2.016	70.07	70.07	34.76	2.63	162.61

Table 6: Relative volume expansion of K-P alloys to RP

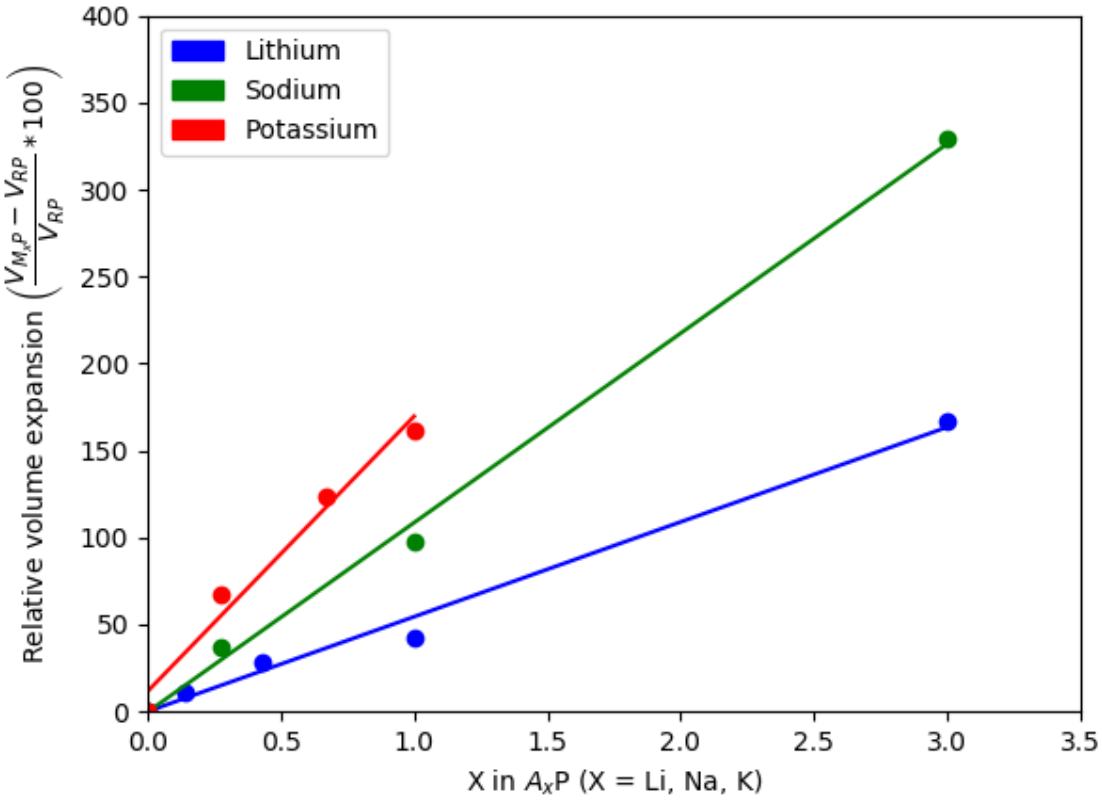


Figure 4: Relative volume expansion of metal-RP alloys to RP.